STARS

Electronic Theses and Dissertations, 2020-

2020

Heterogeneous Integrated Photonics for Nonlinear Frequency Conversion and Polarization Diversity

Tracy Sjaardema
University of Central Florida

Part of the Electromagnetics and Photonics Commons, and the Optics Commons

Find similar works at: https://stars.library.ucf.edu/etd2020

University of Central Florida Libraries http://library.ucf.edu

University of Central Florida

STARS
Showcase of Text, Archives, Research & Scholarship

HETEROGENEOUS INTEGRATED PHOTONICS FOR NONLINEAR FREQUENCY
CONVERSION AND POLARIZATION DIVERSITY

by

TRACY SJAARDEMA
B.S., New Mexico Institute of Mining and Technology, 2015
M.S., University of Central Florida, 2018

A dissertation submitted in partial fulfilment of the requirements
for the degree of Doctor of Philosophy
in the College of Optics and Photonics
at the University of Central Florida
Orlando, Florida

Summer Term
2020

Major Professor: Sasan Fathpour

ABSTRACT

Silicon has proven to be one of the materials of choice for many integrated photonic applications. However, silicon photonics is limited by certain material shortcomings. Two shortcomings addressed in this work are zero second-order optical nonlinearity, and the lack of methods available to achieve broadband polarization diversity. Heterogeneous integrated solutions for these shortcomings of silicon photonics are presented in this work.

First, nonlinear frequency conversion is demonstrated with thin-film lithium niobate on silicon substrates. The method for reaching the highest-achieved second-harmonic generation conversion efficiency, using active monitoring during periodic poling, is discussed. Additionally, a cascaded approach for generating higher-order harmonics is presented, along with a theoretical model to extract conversion efficiencies from measurements performed with pulsed sources. Initial work to integrate second-order and third-order nonlinearities together using thin-film lithium niobate and chalcogenide is also presented.

Second, a spatially-mapped anisotropic material platform that exhibits broadband polarization diversity is discussed. This platform currently demonstrates polarization beam splitters, and polarization-selective beam taps and microring resonators, whose results are presented. Also discussed is a method to include polarization rotators to demonstrate full polarization diversity, as well as designs and initial work to expand the platform to operate at longer wavelengths, specifically those in the telecom band.

This is dedicated to my family who encouraged me and believed in me throughout my PhD.

ACKNOWLEDGMENTS

TABLE OF CONTENTS

LIST OF FIGURES

xiii

LIST OF TABLES

CHAPTER 1: INTRODUCTION

Integrated photonics, originating just a few decades ago, has quickly progressed into a prominent field of optics research. Devices that previously filled an optical table top with bulky, individual, difficult-to-align components can now be realized in tiny, compact devices that can fit on a chip a few centimeters in size. Integrated photonics is essentially the optical equivalent to the integrated circuits of electronics. Soref predicted this with his "superchip" nearly 30 years ago, as shown in Fig. 1.1 [1]. For integrated photonics, the advantages are numerous and the applications are virtually endless.
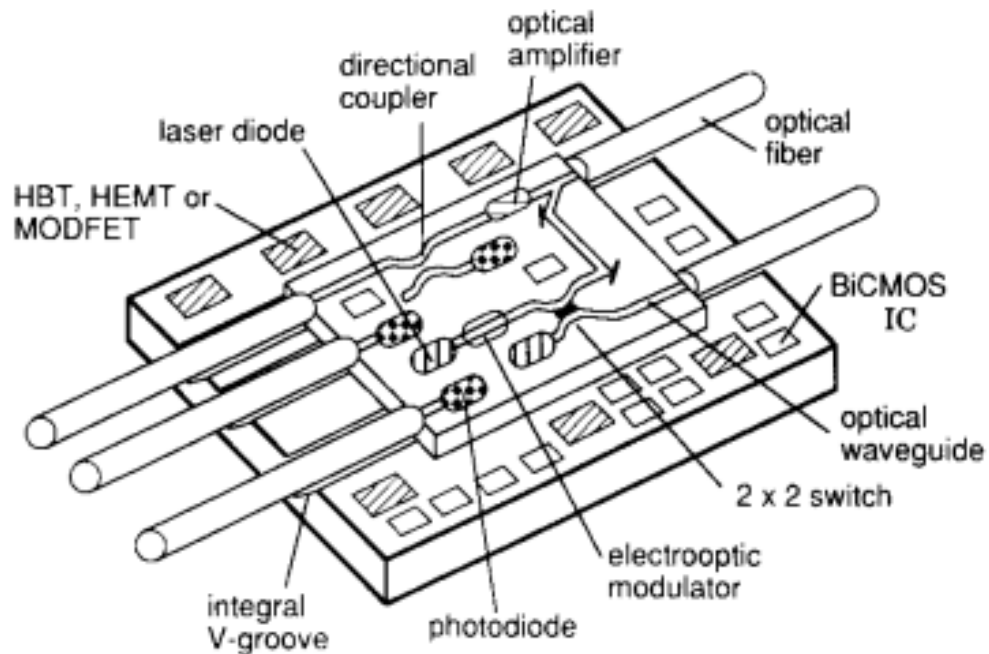
Figure 1.1: Soref's Silicon "Superchip" [1]

1.1   Integrated Photonics

Integrated photonics, initially called integrated optics, began as a concept of a "miniature transmission line" through which laser beams could be guided, with the intent of greatly reducing the size, temperature and vibration sensitivities, and alignment difficulties of free-space systems [2]. Such an implementation promised small sizes, lower optical powers, and even lower driving voltages for active devices. This initial concept has since grown rapidly into the field it is today. Some of the key applications of integrated photonic devices include on-chip passive waveguides and multiplexers, lasers, photodetectors, and modulators.

Some of the most common material choices for integrated photonics today are silicon (Si), III-V semiconductors, often based on gallium arsenide (GaAs) and indium phosphide (InP), and lithium niobate. There are two prominent wavelength ranges of interest – the first is in the near-infrared (near-IR) range of telecom bands (1260 nm to 1675 nm), with emphasis at 1550 nm in the C-band. The second is the mid-infrared (mid-IR), ranging from about 3 μm to 8 μm. Each of these material platforms have their advantages depending on the desired working wavelength range and required device functionality. However, with the advent of silicon on insulator (SOI) technology, silicon has since become the material of choice for many photonics applications.

1.2   Silicon Integrated Photoncis

The growth of silicon photonic devices in the recent decade has been driven by complementary metal oxide semiconductor (CMOS) foundries for photonics [3]. However, the integration of silicon photonics into CMOS technology also has many challenges [4]. SOI technology caused silicon to become one of the materials of choice for photonic devices, due to the much smaller device sizes enabled by the SOI platform. SOI waveguides are formed by a thin silicon waveguide core

layer on top of a lower cladding layer of silicon dioxide (SiO_2) on a silicon substrate, as depicted in 1.2 [5]. As such, SOI waveguides have extremely high index contrast between the core and cladding, allowing for tightly-confined modes, which in turn allows for small bending radii and small device sizes. Numerous applications have been demonstrated with the SOI optical platform [6], including modulators [7, 8, 9, 10], lasers using stimulated Raman scattering (SRS) [11, 12, 13], and wavelength conversion [14, 15, 16].
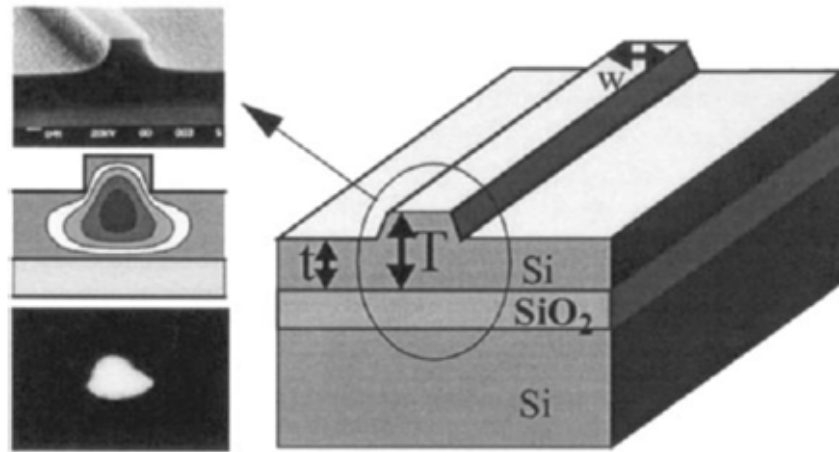
Figure 1.2: Example of SOI waveguide [5].

An ideal photonics platform would have a wide transparency range, second-order nonlinearity, be low loss, support lasing, be ferroelectric to allow for poling ability, be easy to fabricate, and allow for small device sizes. Although SOI photonics has numerous advantages, it, nor any other single platform, can achieve each of these aims alone. Also, no material platform is without its own challenges. One of the main challenges of silicon photonics it its inability to lase. Silicon has an indirect band structure, which prevents lasing due to phonon interactions [6, 17]. The hybrid integration of III-V direct bandgap semiconductors such as GaAs and InP on silicon substrates has been a promising solution [18, 19, 20, 21].

The SOI platform faces other challenges as well, but as above, photonics platforms formed by the heterogeneous integration of silicon with materials better suited to solving these challenges have the combined advantage of both silicon and the integrated materials. This dissertation focuses on two heterogeneous integrated photonic platforms for solving some of the challenges of the SOI platform. Figure 1.3 gives an outline of the dissertation, which will start by portraying two additional challenges of the SOI photonics platform. Heterogeneous platform implementations to solve these challenges will then be introduced, and finally research areas on each of these platforms will be presented in detail.
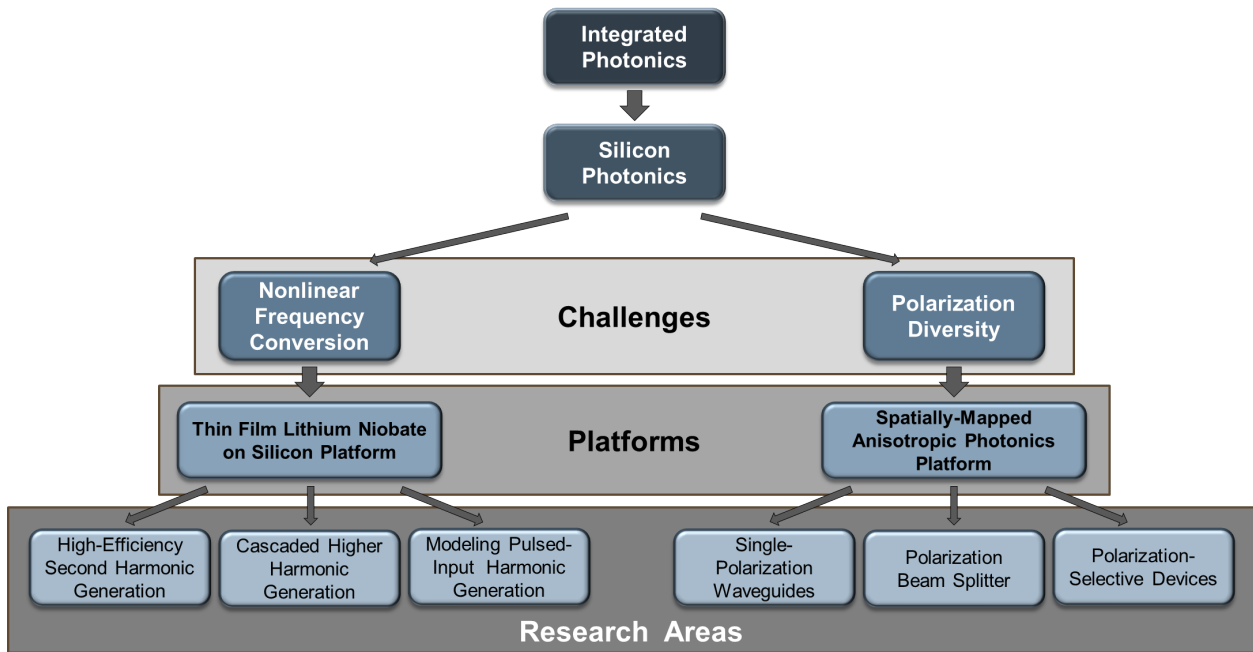
Figure 1.3: Outline of Dissertation

1.3   Challenges for Silicon Photonics

In this work, two additional shortcomings of SOI technology are addressed: the zero second-order nonlinearity of silicon, due to its centrosymmetric crystal structure, and the lack of methods available to achieve broadband polarization diversity. Heterogeneous integration of other materials with silicon photonics can be the answer to address these challenges, and implementations of two platforms and their associated research areas are discussed in this dissertation.

1.3.1   Lack of Second-Order Nonlinearity Addressed with the Thin-Film Lithium Niobate on Silicon Platform

The first shortcoming is a lack of second-order ($\chi^{(2)}$) nonlinearity due to the centrosymmetric crystal structure of silicon. Second-order nonlinear frequency conversion processes are used to generate wavelengths not easily obtained from commercial laser sources, among other applications. The theory, applications, and implementations of second-order nonlinear optics is discussed in greater detail in Chapter 2.

This shortcoming of SOI is addressed by introducing materials with strong second-order nonlinearity for the device layer, including lithium niobate [22, 23], a material with electro-optic properties, or aluminum nitride, a non-centrosymmetric material [24, 25], instead of silicon in a SOI-like structure.

The thin-film lithium niobate on silicon platform combines the strong second-order nonlinearity of lithium niobate and the tight-mode confinement of thin (~1 μm) layers of material with the well-established silicon photonics platform. This platform, with its development, benefits, and implementation is discussed in greater detail in Chapter 2. This platform has been used for many nonlinear optics and electrooptics applications [23].

5

1.3.2   Broadband Polarization Diversity Addressed with the Spatially-Mapped Anisotropic Photonics Platform

The second shortcoming of silicon is a lack of methods to achieve broadband polarization diversity. Broadband polarization diversity is important when processing bipolarized input signals. Due to modal birefringence in the circuits for processing these signals, orthogonal polarizations experience different refractive indices, causing them to each respond to waveguides and devices differently.

Platform designs on which polarizations experience no modal birefringence have been proposed and attempted, but have not yet been fully achieved. Thus, to achieve the same result orthogonal polarizations are instead split and processed separately. Polarization beam splitters or polarization-splitter-rotators are used for this process, however, current implementations suffer from narrow bandwidths and high loss. The applications for polarization-diverse photonic circuits and the current-best polarization-selective device implementations are discussed further in Section 6.1.

The spatially-mapped anisotropic photonics platform is a novel platform presented in Chapter 6. This platform uses common, easily-deposited, non-birefringent materials to form a birefringenet material that when placed as a waveguide core or side-cladding, can form polarization-selective waveguides that guide only transverse-electric (TE) or transverse-magnetic (TM) modes. Polarization beam splitters and other devices are easily implemented with this platform, and due to the nature of the platform, the devices are broadband.

The research topics presented in this dissertation are focused on these two heterogeneous integrated photonics platforms: the thin-film lithium niobate on silicon platform, and the spatially-mapped anisotropic photonics platform. The specific areas of research for each platform are introduced in the following section.

6

1.4 Areas of Research on Thin-Film Lithium Niobate on Silicon Platform

As described above, the thin-film lithium niobate on silicon platform allows devices for second-order nonlinearity to be more easily integrable with existing silicon photonics. In this work, the thin-film lithium niobate on silicon platform is used to fabricate devices for second-order nonlinear frequency conversion, specifically for generating the second-, third-, and fourth-order harmonics. The research presented on this platform in this dissertation includes the following three topics:

1.4.1 High-Efficiency Second Harmonic Generation

The high second-order nonlinearity of lithium niobate and the tightly-confined modes achievable in waveguides on the thin-film lithium niobate on silicon platform allows for highly-efficient second-order nonlinear frequency conversion processes. In Chapter 3, a device for second harmonic generation is presented. This device achieves a record-high second harmonic generation conversion efficiency of 4,600 $\%W^{-1}cm^{-2}$.

1.4.2 Cascaded Harmonic Generation

In Chapter 4, cascaded harmonic generation is demonstrated on the thin-film lithium niobate on silicon platform. Two second-order nonlinear processes, such as that presented in Chapter 3, are cascaded in a device, allowing for the generation of higher harmonics. Generation of the third- and fourth-order harmonics are presented here.

1.4.3   Modeling Pulsed-Input Harmonic Generation

Chapter 5 presents a numerical model for nonlinear harmonic generation for pulsed-source inputs, by solving the nonlinear Schrödinger equation for coupled modes with second-order nonlinearity. This model is applied to the devices from Chapter 4 to quantify the conversion efficiencies of the cascaded segments.

1.5   Areas of Research on Spatially-Mapped Anisotropic Photonic Platform

As described above, the spatially-mapped anisotropic photonics platform can define specific anisotropic regions spatially across an otherwise isotropic material platform. Careful mapping of this anisotropic material on a chip can form the single-polarization waveguides introduced previously, as well as other polarization-selective devices. Due to the nature of the material, these waveguides and devices remain polarization-selective over a broad bandwidth. The following devices are presented in this dissertation.

1.5.1   Single-Polarization Waveguides

The single-polarization waveguides made possible with the spatially-mapped anisotropic photonics platform are discussed further in Section 6.4. These waveguides are broadband and resistant to fabrication tolerances. The results of combining these two waveguides into a single hybrid waveguide are also presented, with interesting implications.

1.5.2   Polarization Beam Splitter

The same principles behind the operation of the single-polarization waveguides can be used to split input light of two orthogonal polarizations, with the TE and TM modes being split in space with a polarization beam splitter. This device has high extinction ratios over a record-breaking bandwidth, and is presented in Section 6.6.1.

1.5.3   Polarization-Selective Devices

Finally, similar to the polarization beam splitter, polarization-selective devices can be made with the spatially-mapped anisotropic photonics platform. These devices act on one polarization and are essentially invisible to the orthogonal polarization. These devices include the polarization-selective beam tap and the polarization-selective microring resonator. Theses devices are discussed in greater detail in Sections 6.6.2 and 6.6.3.

CHAPTER 2: NONLINEAR FREQUENCY CONVERSION

Nonlinear frequency conversion generates wavelengths of light that may not be conveniently available from conventional laser sources [26]. Integrating these sources can be particularly useful towards on-chip circuits and systems, as well as more efficient and smaller-footprint devices that operate at lower optical pump powers than bulk-crystal approaches. The small modal effective area of the integrated waveguides provides a high nonlinear overlap between the interacting modes and thus a higher conversion efficiency. Therefore, much attention has been given to integrated frequency conversion approaches, including harmonic generation [27, 28, 29, 30, 25, 31, 32, 33, 34, 35], frequency combs [36, 37, 38], and even quantum-frequency conversion [39, 40]. This chapter will provide important background theory on nonlinear optics, including defining nonlinear optics, reviewing second-order nonlinear processes, and discussing implementation methods.

First, an introduction to nonlinear optics is given. In linear optics, the polarization of a material system is given by (2.1), where $\tilde{E}(t)$ is the field strength of an applied optical field. Here, the polarization and the strength of the electric field have a linear dependence. ϵ_0 is the permittivity of free space, and $\chi^{(1)}$ is the linear susceptibility [26].

$$\tilde{P}(t) = \epsilon_0 \chi^{(1)} \tilde{E}(t) \tag{2.1}$$

However, for nonlinear optics, the polarization of a material system is described by (2.2), where

$\chi^{(2)}$, $\chi^{(3)}$, and beyond are the second-, third-, and higher-order nonlinear susceptibilities [26].

$$\begin{aligned} \tilde{P}(t) &= \epsilon_0 \left[\chi^{(1)} \tilde{E}(t) + \chi^{(2)} \tilde{E}^2(t) + \chi^{(3)} \tilde{E}^3(t) + \cdots \right] \\ &\equiv \tilde{P}^{(1)}(t) + \tilde{P}^{(2)}(t) + \tilde{P}^{(3)}(t) + \cdots \end{aligned}$$

(2.2)

Second-order nonlinear optics looks at nonlinear processes that happen due to this second-order nonlinear polarization $\tilde{P}^{(2)}(t)$ dependent on $\chi^{(2)}$, and is this focus of this section.

2.1   Second-Order Nonlinear Optics

Second-order ($\chi^{(2)}$) nonlinear processes can only occur in crystals that do not have inversion symmetry, called noncentrosymmetric crystals [26]. Examples of some $\chi^{(2)}$ processes include sum-frequency generation (SGF), difference-frequency generation (DFG), and second-harmonic generation (SHG). These are examples of three-wave mixing. Each of these processes involve two input waves with frequencies ω_1 and ω_2, and produce an output wave with frequency ω_3. SFG generates a frequency equal to the sum of the input frequencies and DFG generates a frequency equal to the difference of the input frequencies. SHG is a special case of SFG where the input frequencies are equal. These conversion processes are visualized in the energy-level diagrams of Fig. 2.1. The energy-level diagrams show the absorption (upwards arrows) and emission (downwards arrows) of photons of the different frequencies [26].

More background information and equations are given to describe three-wave mixing processes. For these processes, two input frequencies, ω_1 and ω_2, are required. The input field is given by

11
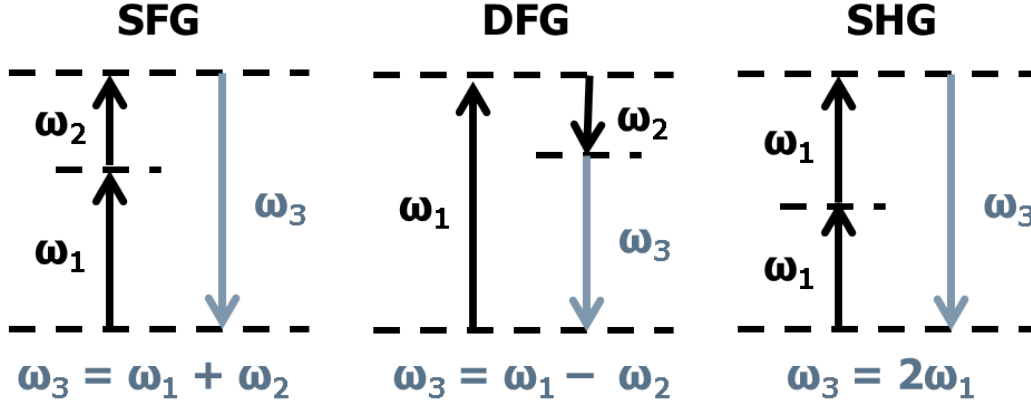
Figure 2.1: Energy-level diagrams for $\chi^{(2)}$ processes.

$\tilde{E}(t)$ in (2.3).

$$\tilde{E}(t) = E_1 e^{-i\omega_1 t} + E_2 e^{-i\omega_2 t} + c.c. \tag{2.3}$$

Substituting this field into (2.2) gives the following nonlinear polarization in (2.4), where the terms denoted by the underbrace are two terms for SHG, where the new frequency is twice the input frequency. The term denoted by the overbrace is the term for SFG, where the new frequency is the sum of the input frequencies. The other terms are for DFG and optical rectification.

$$\tilde{P}^{(2)}(t) = \epsilon_0 \chi^{(2)} \left[\underbrace{E_1^2 e^{-2i\omega_1 t}} + \underbrace{E_2^2 e^{-2i\omega_2 t}} + \overbrace{2E_1 E_2 e^{-i(\omega_1+\omega_2)t}} + 2E_1 E_2^* e^{-i(\omega_1-\omega_2)t} + c.c. \right] +$$
$$2\epsilon_0 \chi^{(2)} \left[E_1 E_1^* + E_2 E_2^* \right] \tag{2.4}$$

From this nonlinear polarization resulting from an input field with two frequency components, the

complex amplitude of the nonlinear polarizations can be defined as (2.5) for SHG processes and as (2.6 for SFG processes.

$$P(2\omega) = \epsilon_0 \chi^{(2)} E^2 \tag{2.5}$$

$$P(\omega_1 + \omega_2) = 2\epsilon_0 \chi^{(2)} E_1 E_2 \tag{2.6}$$

From here, it is beneficial to look at the coupled-mode equations for SHG for a periodic waveguide (2.7), derived using the local normal-mode expansion (LNME). This derivation is detailed in [41].

$$\frac{d}{dz}a_{2\omega}(z) = -i\left(a_\omega(z)\right)^2 e^{i\Delta\beta_0 z} f(z) - \frac{\alpha_{2\omega}}{2}a_\omega(z)$$
$$\frac{d}{dz}a_{2\omega}(z) = -ia_\omega(z)a_{2\omega}^*(z)e^{-i\Delta\beta_0 z} f^*(z) - \frac{\alpha_\omega}{2}a_\omega(z) \tag{2.7}$$

In the above coupled-mode equations, $a_\omega(z)$ and $a_{2\omega}(z)$ are the normalized field amplitudes of the fundamental and second-harmonic (SH) signals at frequencies ω and 2ω, α_ω and $\alpha_{2\omega}$ are the propagation losses in the waveguide at the two frequencies, and $\Delta\beta_0$ is a phase mismatch between the two waves. $f(z)$ is a nonlinear coupling term containing the effects of modulating the

13

waveguide, and is defined in (2.8)[22].

$$f(z) = \sqrt{2}\omega\left(\frac{\mu_0}{\varepsilon_0}\right)^{\frac{3}{4}} \frac{\exp\left[-i\int_0^z 2\beta_\omega(\zeta) - \beta_{2\omega}(\zeta) + \Delta\beta_0 d\zeta\right]}{n_{\text{eff}}^\omega(z)\sqrt{n_{\text{eff}}^{2\omega}(z)}}\Gamma(z),$$

(2.8)

$$\text{where } \Gamma(z) = \frac{\iint d(x,y,z)\left\{E^{2\omega}(x,y,z)\right\}^* \left\{E^\omega(x,y,z)\right\}^2 dxdy}{\left[\left\{\iint |E^{2\omega}(x,y,z)|^2 dxdy\right\}\left\{\iint |E^\omega(x,y,z)|^2 dxdy\right\}^2\right]^{\frac{1}{2}}}$$

In the above equation, E^ω and $E^{2\omega}$ are the transverse mode field profiles, n_{eff}^ω and $n_{\text{eff}}^{2\omega}$ are the effective refractive indices, and β_ω and $\beta_{2\omega}$ are the propagation constants, all of the fundamental and SH respectively. $d(x,y,z)$ is the second-order nonlinear d tensor, which is equal to half of the second-order nonlinear susceptibility tensor, $\chi^{(2)}$.

The phase mismatch, $\Delta\beta_0$, is due to dispersion in the waveguide causing a momentum mismatch between the interacting photons involved in the frequency generation process. If this phase mismatch is not compensated for, the frequency conversion process will be inefficient. Methods for this compensation are called phase matching.

2.2   Phase Matching

These phase-matching methods must apply a z-dependent variation to $f(z)$, above, to compensate for the phase mismatch. When this compensation is periodic, it is called quasi-phase matching (QPM). QPM essentially provides an extra phase term from this periodic variation to compensate for the phase mismatch from the dispersion of the waves. Two approaches of implementing QPM

14

are grating-assisted QPM and periodic poling. These approaches and their implementations are discussed in greater detail below.

2.2.1 Grating-Assisted QPM

In grating-assisted QPM, the z-dependent variation comes from modulating the transverse mode field profiles $E^{\omega}(x,y,z)$ and $E^{2\omega}(x,y,z)$ of the waves at the pump and the SH, noted by the terms contained in the overbrace in $f(z)$ from (2.8). This can be done by modulating the shape of the waveguide itself in a process called mode-shape modulation (MSM) [42]. The waveguide width is sinusoidally-varied between the two values shown in Fig. 2.2, providing the necessary QPM. The nonlinear effect is achieved from modulating the nonlinear mode overlap integral between the pump and SH waves. This approach to QPM is useful in non-ferroelectric materials that cannot be poled.
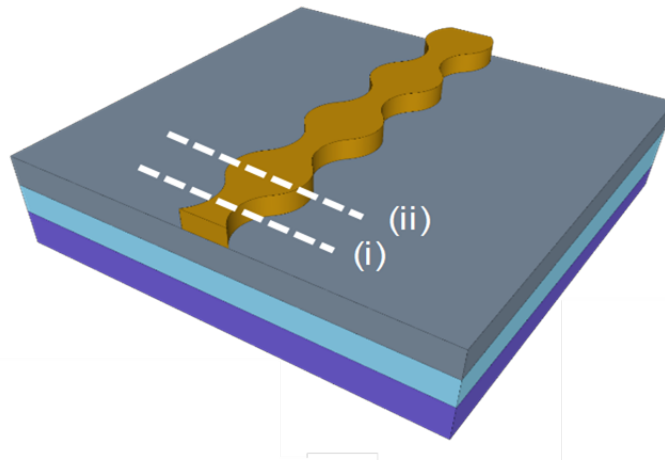
Figure 2.2: Example of a MSM waveguide [42].

OSA-trace results showing the SH signal generated from MSM-QPM are shown in Fig. 2.3. These measurements were performed with a pulsed-source input, and the data is originally published in

15

[42].
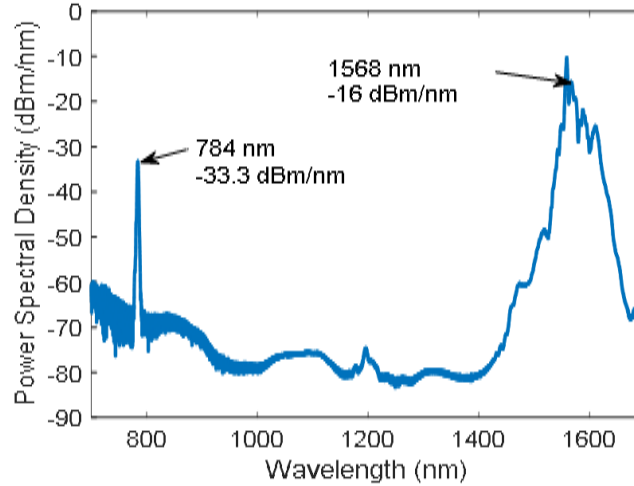
Figure 2.3: SHG results from a MSM waveguide [42].

2.2.2 Periodic Poling

Another method for implementing QPM is by adding a z-dependent variation from modulating the second-order nonlinear d tensor, noted by the term contained in the overbracket in $f(z)$ from (2.8). This modulation comes from a periodic reversal of the domain of the material, mathematically represented by a periodic reversal in the sign of coefficients in the d tensor. This is implemented by periodically poling a ferroelectric material. Poling involves applying an electric field across a material, large enough to be greater than the coercive field strength of the material and thus cause a domain reversal. Poling the material periodically results in the periodic domain reversal necessary for QPM. Figure 2.4 shows an example of the metal electrodes used for poling, and the resulting domain reversal.

The periodicity of the poling, Λ, is calculated from the wavevector mismatch Δk as shown in (2.9).

16
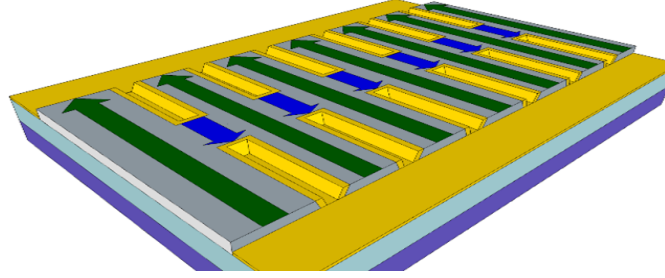
Figure 2.4: Example of periodically-poled material, showing electrodes and domain reversal [27].

The equations for calculating the wavevector mismatch for SHG, SFG, and DFG processes are given in (2.10).

$$\Lambda = \frac{2\pi}{\Delta k} \qquad (2.9)$$

$$\Delta k = \begin{cases} k_1 + k_2 - k_3 & \text{SFG} \\ k_3 - k_1 - k_2 & \text{DFG} \\ 2k_1 - k_2 & \text{SHG} \end{cases} \qquad (2.10)$$
$$\text{where } k_m = \frac{n_m 2\pi}{\lambda_m}$$

Periodic poling is applicable to ferroelectric materials such as lithium niobate, lithium tantalate, and others. As lithium niobate has one of the highest second-order nonlinearities, along with other advantages, this makes it a material of choice to use for second-order nonlinear processes. Lithium niobate, and its methods of implementation, are further discussed in the next section

2.3 Lithium Niobate

There are several reasons why lithium niobate (LiNbO$_3$, LN) is a well-established material choice for frequency conversion processes [43, 44]. LN has high $\chi^{(2)}$ nonlinearity (d_{33} = 30pm/V), allowing for efficient frequency conversion. LN also has a broad transparency range (~0.35 - 5.2 μm), allowing operation at multiple wavelengths for a wide range of applications. Finally, LN has a strong electrooptic effect, allowing for periodic poling for QPM for nonlinear frequency conversion. Periodically-poled LN (PPLN) has been shown to produce high-efficiency second-order nonlinear processes [45, 46, 47, 48, 49, 50]. However, bulk PPLN has some disadvantages. These are detailed below, followed by a method for solving these problems.

2.3.1 Conventional PPLN Diffused Waveguides

Conventional LN waveguides are formed through diffusion and proton-exchange techniques [51, 52]. These waveguides with titanium-diffused (ti-diffused) cores are difficult to integrate with silicon photonics, and due to the fabrication process, the waveguides themselves are large, resulting in large devices, large bending radii, large cores, and thus large mode sizes. The diffused waveguides also have a low index contrast between the core and the cladding, resulting in weakly-confined modes. These large, weakly-confined modes result in low conversion efficiencies for second-order nonlinear frequency conversion processes, as discussed in greater detail below. Figure 2.5 shows a diagram of a ti-diffused waveguide.

Since LN itself has extremely favorable material qualities, a method for fabricating small, high-contrast waveguides that could combine these material advantages with the benefits of smaller mode sizes would be profitable for numerous applications. The process for achieving such a scheme, thin-film LN, is discussed in the following section.
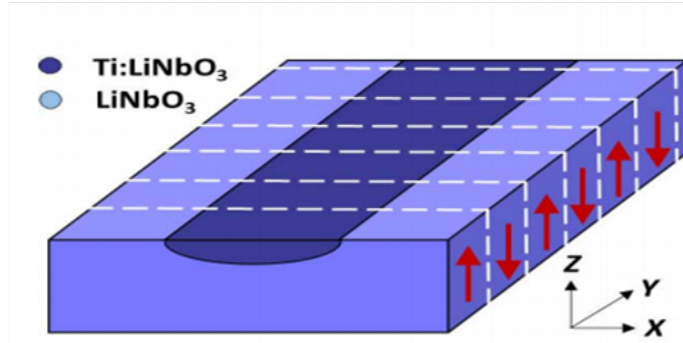
Figure 2.5: Example of a ti-diffused LN waveguide [53].

2.3.2   *Thin-Film Lithium Niobate on Silicon*

Thin-film LN, particularly on silicon substrates, has proven to be a promising platform to address the issues faced by conventional LN for many nonlinear integrated devices [53, 22, 54, 29, 55]. Thin-film LN wafers are formed through ion implantation, bonding, and thermal slicing processes [56]. This process starts with helium ion implantation on bulk single-crystal LN wafers, which are bonded to a thermally-oxidized silicon wafer. This bonded wafer pair is heated for thermal slicing of the bulk LN, leaving a thin LN layer on the oxidized silicon. The rest of the bulk LN can then be recycled and used for another thin-film LN fabrication process. The silicon wafer with the bonded LN layer is annealed to recover the LN nonlinear coefficients, and the surface is then planarized with chemical-mechanical polishing. The device layer is less than one micron thick, and is isolated from the substrate by a silicon dioxide bottom cladding layer . Figure 2.6 depicts this fabrication process for thin-film LN on silicon wafers.

Optical waveguides are formed on the thin-film wafers by either rib-loading or direct-etching. This thin-film platform results in smaller waveguides, and thus smaller device footprints and smaller

19

i) Ion implantation

ii) Oxidized Si substrate

Recycled

200 to 600 nm LN thin film

2 µm

○ LiNbO$_3$
○ SiO$_2$
● Si substrate

iii) Wafer bonding

iv) Thermal slicing
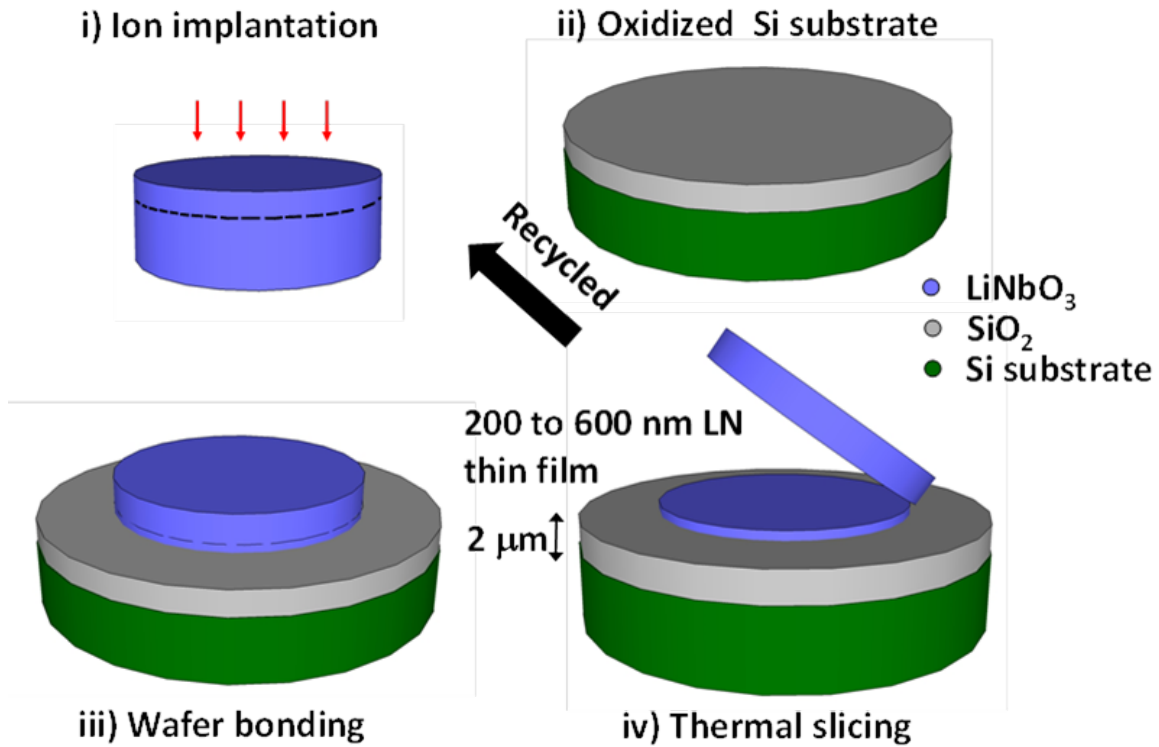
Figure 2.6: Process for fabricating thin-film LN on silicon [56].

mode sizes, than conventional LN waveguides, and the modes are much more tightly-confined in the core due to the higher index contrast between the core and the cladding. A comparison of mode sizes between a conventional diffused LN waveguide and a thin-film LN waveguide is given in Fig. 2.7.

Rib-loading is one implementation method used to form optical waveguides on the thin-film LN wafers, where a material that is index-matched to the LN (typically silicon nitride or chalcogenide) is deposited on the LN and etched to form the rib of the waveguide to confine the mode to the LN [42, 57, 27, 58]. Figure 2.8 depicts a rib-loaded PPLN waveguide. These materials have historically been easier to etch than LN. Low-loss direct-etching of LN to form a ridge waveguide is a more
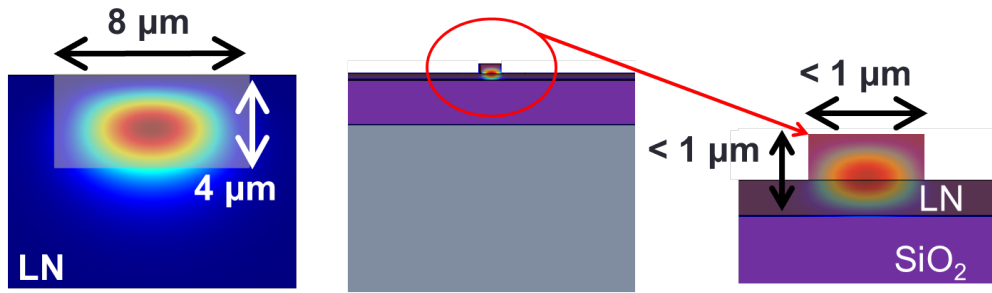
Figure 2.7: Mode-size comparison between conventional diffused LN (left) and thin-film LN (right) waveguides.

recent achievement [55, 28].
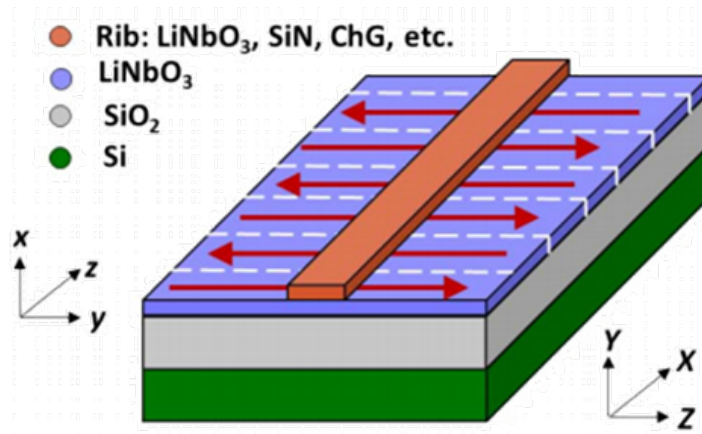
Figure 2.8: Example of rib-loaded PPLN waveguide [53].

2.3.3 Thin-Film PPLN on Silicon

When periodically-poled and used for nonlinear frequency conversion, the thin-film platform also allows for higher mode overlap, resulting in much more efficient $\chi^{(2)}$ frequency conversion processes. The first demonstration of SHG with thin-film PPLN is found in [27], with rib-loaded waveguides.

Characterized by conversion efficiency, this implementation achieved 730 $\%\mathrm{W}^{-1}\mathrm{cm}^{-2}$. Additionally, since the nonlinear conversion efficiency is inversely proportional to the nonlinear interaction area, an ultracompact waveguide that tightly confines the mode in the nonlinear material results in higher conversion efficiencies [27, 23, 22, 59, 28]. Figure 2.9 shows this increase in SH power for increased optical mode confinement. Thin-film implementations can also be poled more easily and more effectively and with lower electric fields than conventional LN wavgeuides.
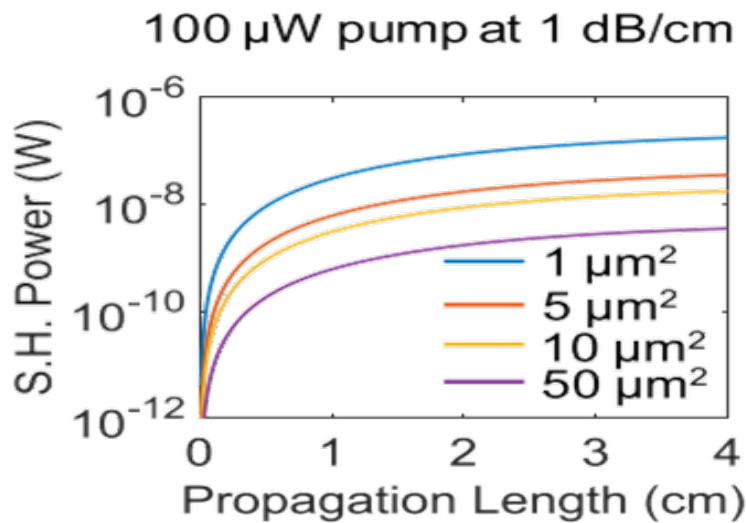
Figure 2.9: Mode-size comparison between conventional diffused LN (left) and thin-film LN (right) waveguides.

After achieving a low-loss LN dry-etch process, this is applied to PPLN waveguides. The conversion efficiencies are higher with this direct-etch approach, as the mode remains entirely confined in the highly-nonlinear LN [55, 28]. Most recently, SHG with record-high efficiency of $4,600\ \%\mathrm{W}^{-1}\mathrm{cm}^{-2}$ has been demonstrated in direct-etched thin-film PPLN-on-Si [55]. This research is presented in detail in Chapter 3.

CHAPTER 3: HIGH-EFFICIENCY SECOND HARMONIC GENERATION

These thin-film PPLN segments, as introduced in the previous chapter, can be implemented to achieve high-efficiency SHG nonlinear frequency conversion. In this work, record-breaking $4,600\ \%\text{W}^{-1}\text{cm}^{-2}$ conversion efficiency for SHG has been generated in direct-etch thin-film PPLN on silicon waveguides. A new poling scheme is introduced to ensure efficient and optimized poling is achieved. Finally, the device is measured with a pulsed source, suggesting higher-order harmonics are able to be generated in these PPLN segments. This work is originally published in [55].

3.1 Design and Fabrication

As discussed previously, small, high-contrast waveguides with tightly-confined modes are essential for achieving high conversion efficiencies through integrated approaches. Thus, the waveguide is designed with this in mind. 300 nm X-cut LN film on an oxidized silicon wafer is chosen for the devices, resulting in a small waveguide core and a strong index contrast between the core and both the SiO_2 lower cladding and the air upper cladding.

3.1.1 Simulation

COMSOL mode simulations are run to determine the waveguide dimensions, including etch-depth (to optimize between mode confinement and waveguide loss), waveguide core width, and electrode spacing across the waveguide (to optimize between metal-induced optical loss and required electric field strength for poling the LN). Figure 3.1 shows the device structure, where the LN film is 300

23
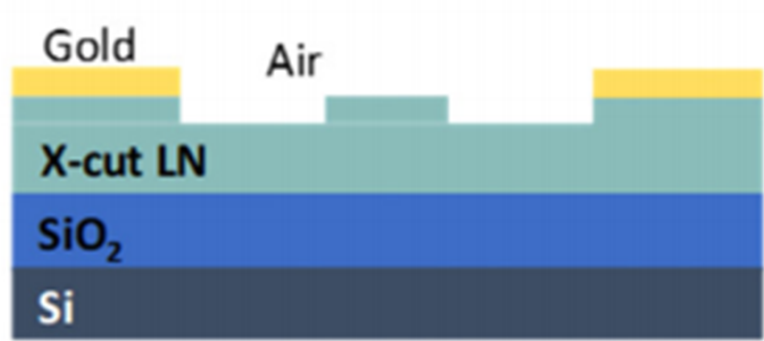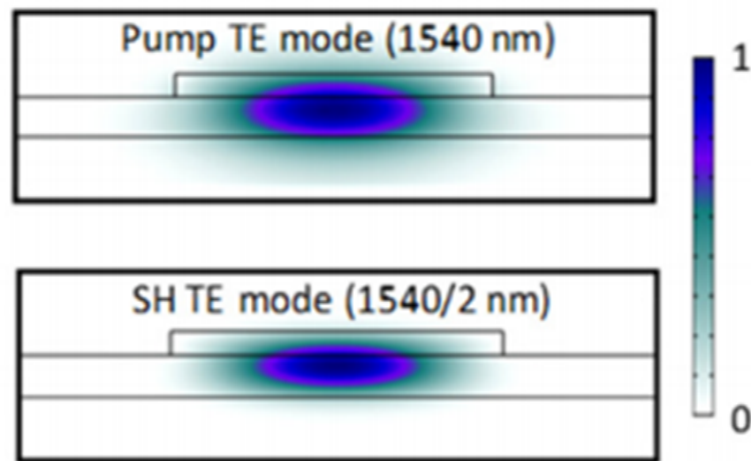
Figure 3.1: (a) Waveguide cross-section. (b) Simulated TE mode images for the pump and SH wavelengths [55].

nm, the etch-depth is 100 nm, and the waveguide width is 1.5μm, and COMSOL simulations of the fundamental and SH TE modes.

The poling period of the electrodes is calculated from the effective indices returned by the mode simulations for the fundamental pump and SH TE modes, from (2.10). TE modes are used because due to the X-cut LN crystal orientation, TE modes allow for the use of the highest LN nonlinear tensor coefficient, d_{33}, and reversal of the ferroelectric domains parallel to the crystal Z-axis of

the LN by periodic poling. The fundamental mode is used, as higher-order modes increase the nonlinear interaction area and thus decrease the achievable conversion efficiency. The poling period chosen is $\Lambda = 2.67 \mu$m for QPM between the fundamental pump and TE modes. A 3-D finite element method simulation of the electric field for poling the LN is performed, using an applied voltage of 400 V. $y - z$ and $x - y$ plane cross-sections extracted from this simulation are shown in Fig. 3.2, showing the distribution of the electric field.
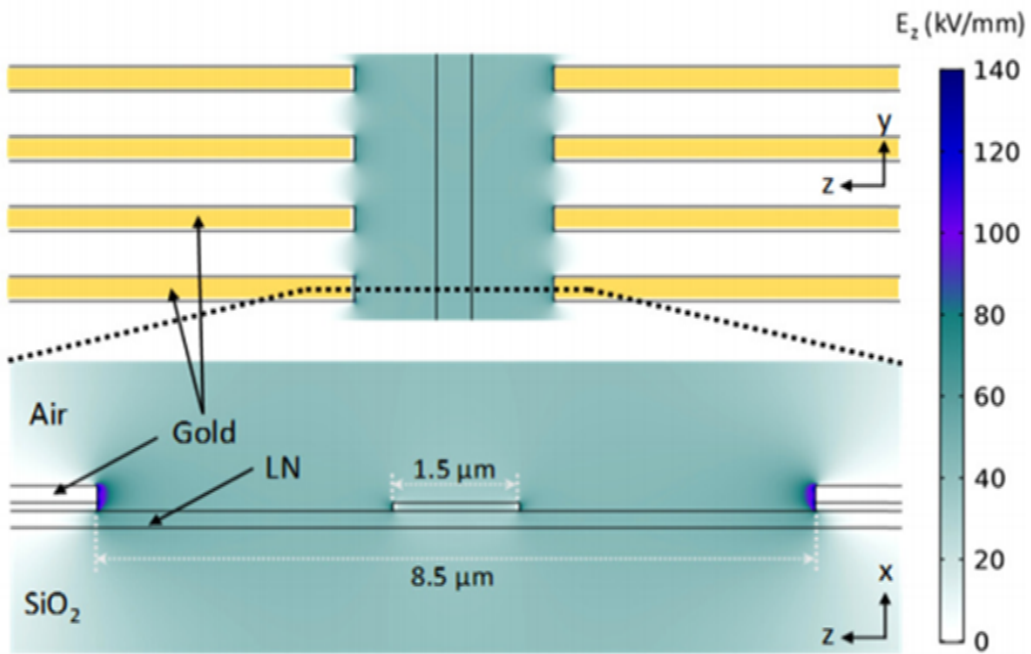
Figure 3.2: Cross-sections of the (top) $y - z$ and (bottom) $x - z$ planes from electric poling field simulations.

3.1.2 Fabrication

The devices are fabricated on 300 nm thin-film X-cut LN on a silicon substrate [56]. The electrodes for poling are formed first, through steps of patterning with electron-beam lithography, chrome and

25

gold deposition viea electron-beam lithography, and lift-off in N-Methyl-2-pyrrolidone heated to 120 °C. The waveguides are formed next, patterned again by electron-beam lithography, and dry-etched in an argon plasma. Subsequent cleaning steps in an oxygen plasma and a dilute hydrofluoric acid (HF) solution (1:100 49% HF:H_2O) are performed. The waveguide facets are formed by dicing and polishing. More detailed descriptions of the fabrication process and etching recipe are given in Appendices A and B, respectively. Figure 3.3 shows a scanning-electron microscope (SEM) image of the final fabricated device, showing the waveguide and metal electrodes.
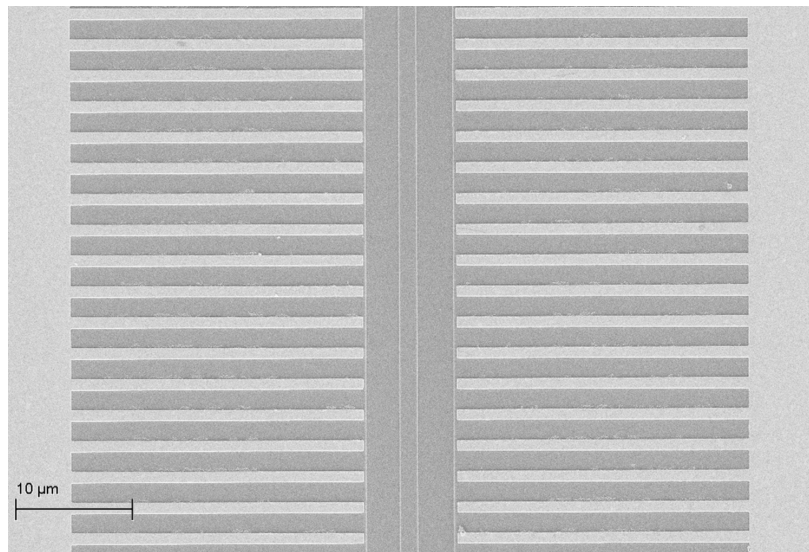
Figure 3.3: SEM image of the fabricated PPLN device.

3.2   Characterization and Measurements

These devices are poled using an actively-monitored iterative poling process. This method, along with the setup used for poling, is discussed below. After poling, the SHG is characterized through measurements with continuous-wave (CW) and pulsed sources.

26

3.2.1 Actively-Monitored Iterative Poling for Second Harmonic Generation

During the poling process, a tunable CW laser centered around 1550 nm is fiber-coupled into the waveguide, and the output power at the SH is monitored as the electrodes are poled. This real-time monitoring allows for the adjustment of poling parameters for repeated poling processes to reach optimal SHG results, as opposed to poling processes performed partway through the fabrication process, where the electrodes are later inaccessible and further adjustments to the poling is impossible.

The setup for poling consists of an arbitrary-waveform generator (AWG) for generating the pulses, which are monitored with an oscilloscope (OSC). The pulses from the AWG are amplified by 100x with a high-voltage amplifier (HVA). These high-voltage pulses are applied to the electrodes with tungsten contact probes. High-voltage pulses are required to generate electric fields strong enough for poling the LN. The field strength must be higher than the coercive field of LN, 21 kV/mm [60]. The setup for measuring the SH consists of the tunable CW laser passed through a polarization controller (PC) and lensed-fiber-coupled into the waveguide at the diced and polished facet. Any generated output light, along with the pump light, is coupled out of the waveguide with a second lensed fiber at the output. The pump light is measured using a calibrated InGaAs photodetector (PD), and the SH light is measured using a calibrated silicon PD. This setup is depicted in Fig. 3.4.

When poling the PPLN electrodes, the electric field strength (by way of applied voltage), pulse duration, and pulse repetition period can ve varied in order to optimize the poling. Preliminary results show voltage pulses of 400 V, 5 ms in duration, with a 5 s repetition period performed the best. A 600μm-long PPLN waveguide is poled with pulses with these parameters until the SHG power saturates, and the conversion efficiency, defined by (3.1), where P_ω is the power of the pump in the waveguide, $P_{2\omega}$ is the power of the SH in the waveguide, and L is the length of the waveguide in cm, is recorded. The polarity of the pulses is then reversed, and the devices are depoled until the

27
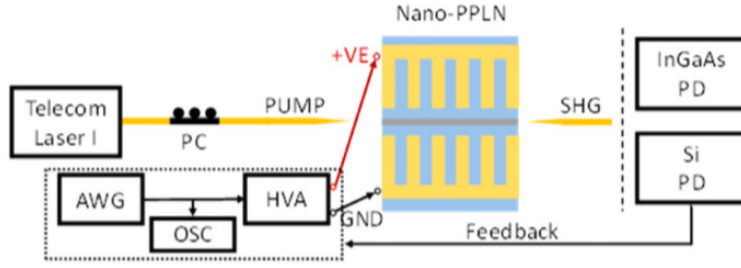
Figure 3.4: Setup used for the actively-monitored iterative poling process for generating the SH.

SHG power is below the noise level.

$$\eta = \frac{P_{2\omega}}{P_\omega^2 L^2} \tag{3.1}$$

Repeating this process shows an increased SHG power. This process is repeated for 9 poling and depoling cycles, before the peak SHG conversion efficiency begins to saturate, at $2,800~\%\mathrm{W}^{-1}\mathrm{cm}^{-2}$. The results for increased conversion efficiency with additional poling cycles in shown in Fig. 3.5, along with a plot of the peak conversion efficiency of the device versus pump wavelength.

This poling, depoling, and repoling process to generate a SH signal with increasing peak power suggests the repeated poling process improves poling uniformity and domain reversal in the LN.

This iterative, monitored poling process and the CW measurements are repeated for another waveguide, this time with a length of 300μm. For this waveguide, the poling process is repeated for 8 poling and depoling cycles, while also increasing the length of the poling pulse up to 30 ms. The maximum conversion efficiency is achieved after 4 poling cycles and then starts to decrease, and after 6 poling cycles the conversion efficiency saturates. The peak conversion efficiency reaches $4,600~\%\mathrm{W}^{-1}\mathrm{cm}^{-2}$. A plot of conversion efficiency versus number of poling cycles in shown in Fig.
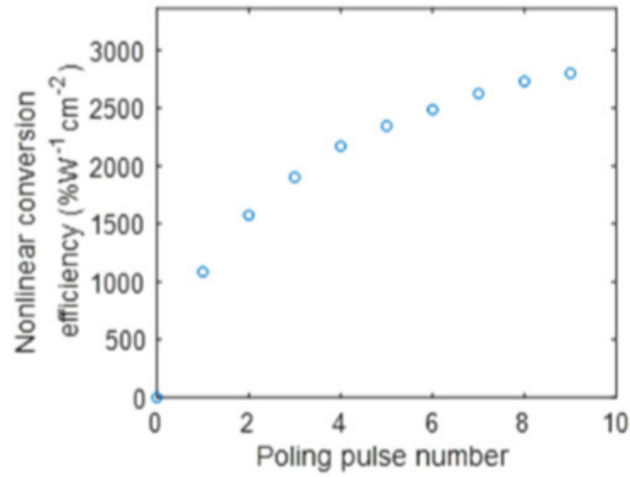
(a)
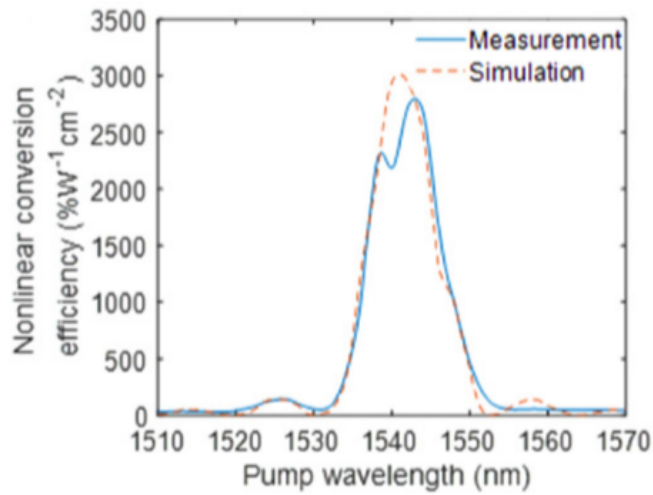
(b)

Figure 3.5: Results for CW measurements of the 600μm-long PPLN device with iterative poling cycles. (a) Increasing then saturating conversion efficiency for additional poling cycles. (b) Measured $2,800$ %W^{-1}cm^{-2} peak conversion efficiency [55].

3.6, along with a plot of the peak conversion efficiency of the device versus pump wavelength.

These results show that overpoling the device is possible, leading to a reduced final conversion efficiency. The improved peak conversion efficiency for the 300μm-long device may be due to better poling uniformity over a shorter distance.

3.2.2   Pulsed-Input Measurements

The devices are next measured with a pulsed pump source from a commercial fiber laser. The pulses have a repetition rate of 80 MHz, with 100 fs pulse width. Due to the broad bandwidth of the pulsed source, additional wavelengths are phase-matched, leading to not only a broad SHG output pulse, but also third-harmonic generation from SFG of the pump and SH, and fourth-harmonic generation from SHG of the SH. This result is shown in Fig. 3.7 for multiple input pump powers, and also a plot of the output for the maximum input pump power.

These results suggest that with additional design, devices can be fabricated to optimize these higher-order harmonics. This approach is detailed in Chapter 4.

3.3   Conclusions

This chapter discussed the design, fabrication, and characterization of high-efficiency thin-film PPLN on silicon devices. The devices were fabricated by directly-etching the LN film to form the waveguide core, and they were poled using a novel, actively-monitored iterative poling process to achieve maximum conversion efficiency. A peak, record-high CW SHG conversion efficiency of $4,600$ %W^{-1}cm^{-2} was measured in the device. Additionally, the devices were measured with a pulsed pump source, and small amounts of third- and fourth-order harmonics were generated,
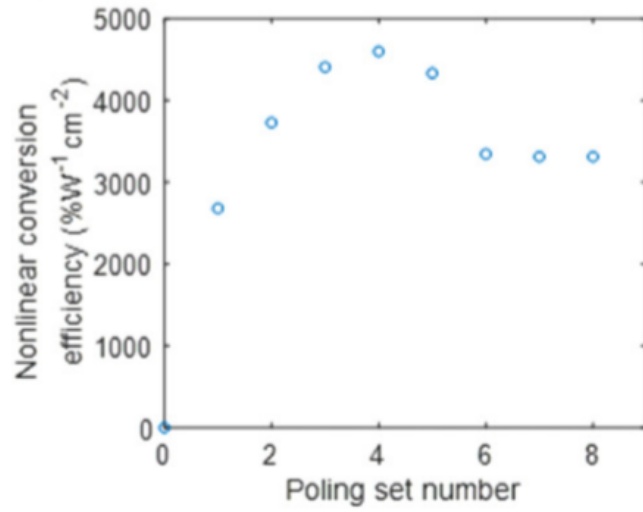
(a)
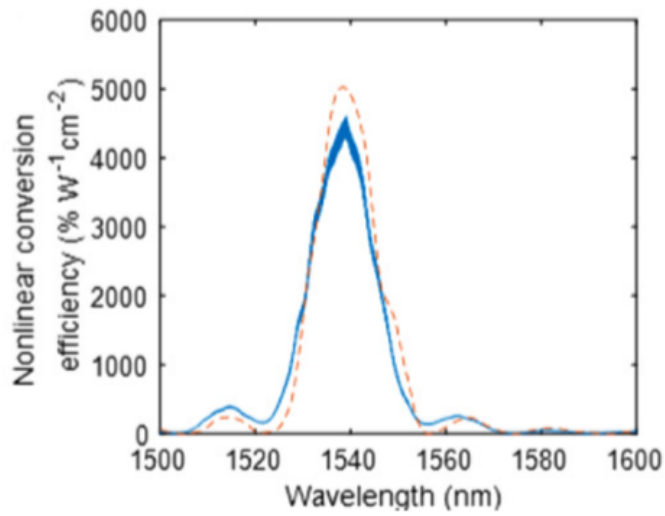
(b)

Figure 3.6: Results for CW measurements of the 300μm-long PPLN device with iterative poling cycles. (a) Increasing, decreasing, then saturating conversion efficiency for additional poling cycles. (b) Measured 4,600 %W^{-1}cm^{-2} peak conversion efficiency [55].
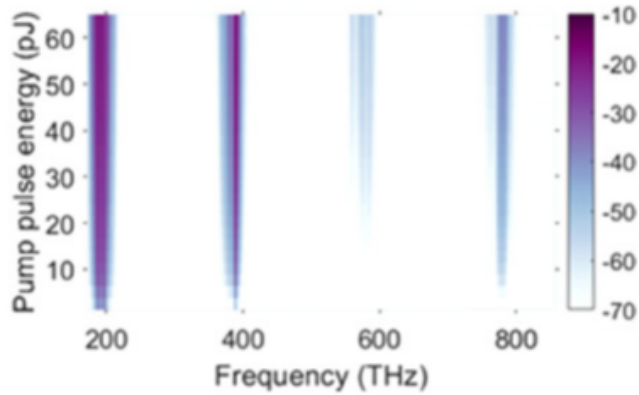
(a)
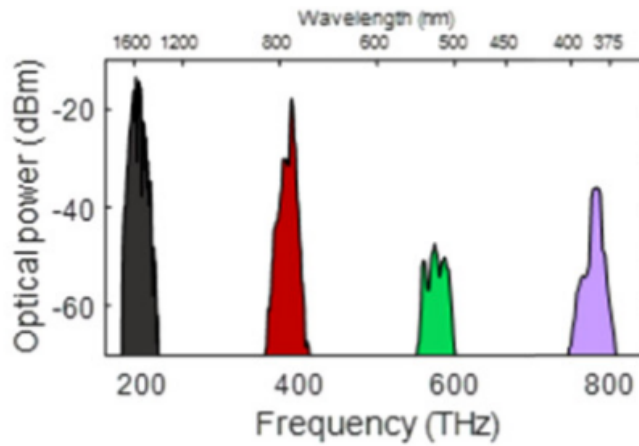
(b)

Figure 3.7: Results for pulsed-pump measurements for (a) multiple input pump powers and (b) the maximum input pump power [55].

suggesting that further optimization of cascaded PPLN segments for SFG and SHG could increase the conversion efficiencies of these higher-order harmonics.

CHAPTER 4: CASCADED HARMONIC GENERATION

These integrated PPLN segments for $\chi^{(2)}$ frequency conversion processes, discussed in Chapter 3 for SHG, can be cascaded to achieve higher harmonic generation, for example, third- and fourth-order harmonic generations. Conventional PPLN has been used to demonstrate higher-order harmonic generation [30]. Also, THG is demonstrated through a cascaded process on LN-on-insulator (LNOI) microdisks [61]. However, in this work, strong third- and fourth-harmonic generations are demonstrated for the first time in cascaded thin-film PPLN-on-Si ultracompact devices.

4.1   Device Concept

Cascading $\chi^{(2)}$ nonlinear frequency conversion processes in PPLN can be used to generate higher-order harmonics while still taking advantage of the strong second-order nonlinearity of LN. While the third-harmonic could be achieved through a third-order nonlinearity frequency tripling process, the second-order nonlinearity of LN is more efficient. Additionally, other harmonics can be reached by a similar cascaded implementation, by careful selection of the second-order nonlinear processes being cascaded.

4.1.1   Third Harmonic Generation

As depicted in Fig. 4.1, the third harmonic (TH) can be generated by first using a SHG segment to generate the SH of the input pump wavelength, and then using SFG in a second cascaded segment in order to generate the TH from the sum of the pump and the SH. As long as the transparency range of LN (~0.35 —5.2 μm) is not violated, other combinations of $\chi^{(2)}$ processes can also be cascaded to reach even higher harmonics. For example, adding a third segment, quasi-phase-matched for SFG,

33

to the device in Fig. 4.1 can reach the fifth-order harmonic. These cascaded structures can also be tuned to reach a broad span of wavelengths, depending on the fundamental, or pump, wavelength.

$$\star \quad \omega_1$$

$$\star \quad \omega_2 = \omega_1 + \omega_1 = 2\omega_1$$

$$\star \quad \omega_3 = \omega_1 + \omega_2$$
$$= \omega_1 + 2\omega_1 = 3\omega_1$$
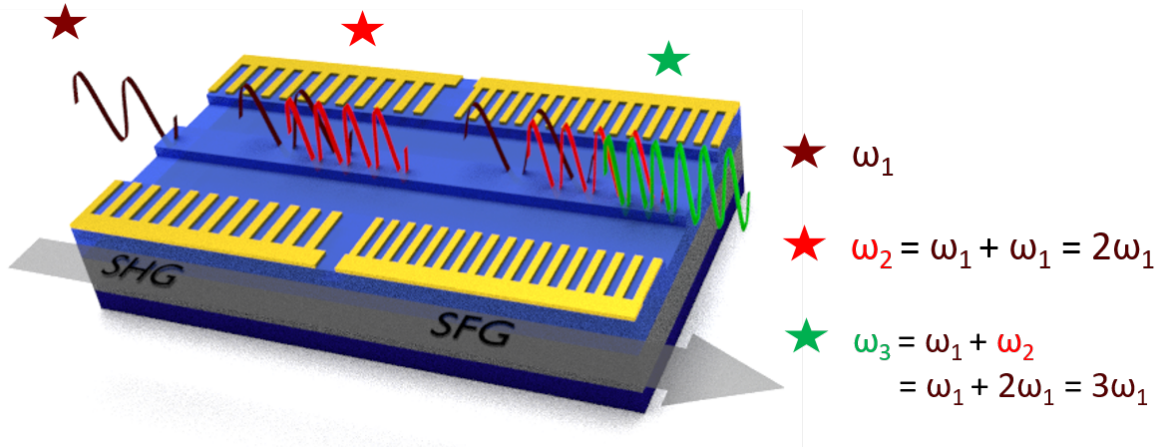
Figure 4.1: Schematic showing how two second-order nonlinear SHG and SFG processes can be cascaded to generate the third-order harmonic.

4.1.2 Fourth Harmonic Generation

Figure 4.2 shows how the fourth harmonic (FH) can be similarly generated by cascading two SHG segments, where the first segment doubles the pump frequency to generate the SH, and the second segment doubles the SH frequency to generate the FH. As before, as long as the transparency range of LN (~0.35 —5.2 μm) is not violated, other combinations of $\chi^{(2)}$ processes can also be cascaded to reach higher harmonics. By adding a third segment, quasi-phase-matched for SFG, to the device in Fig. 4.2, the sixth-order harmonic can be generated.

$$\star \quad \omega_1$$

$$\star \quad \omega_2 = \omega_1 + \omega_1 = 2\omega_1$$

$$\star \quad \omega_4 = \omega_2 + \omega_2$$
$$= 2\omega_1 + 2\omega_1 = 4\omega_1$$
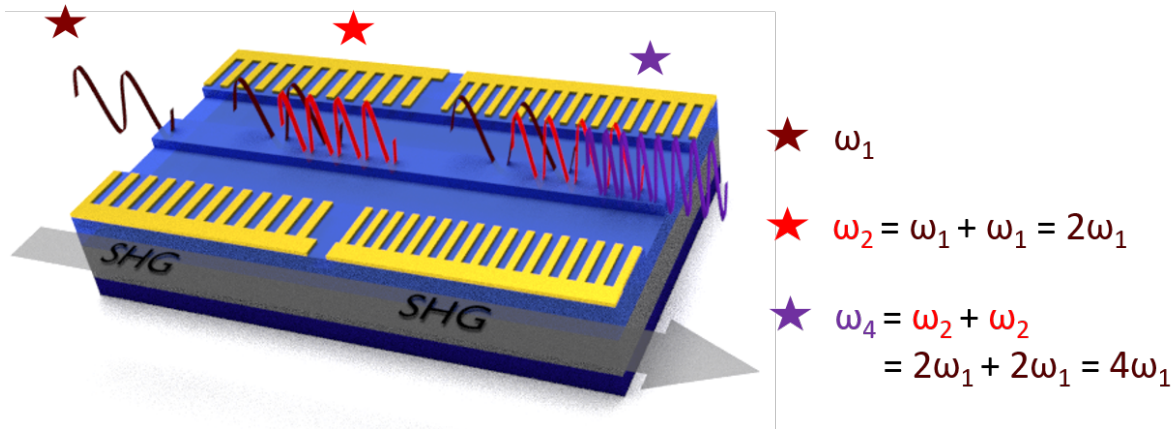
Figure 4.2: Schematic showing how two second-order nonlinear SHG processes can be cascaded to generate the fourth-order harmonic.

4.2 Design and Fabrication

This section details the simulation process for finding the optimal dimensions of the waveguide itself, including width and etch depth, the spacing between the electrodes across the waveguide, and the electrode poling periods for each of the four PPLN segments of the devices.

The fabrication steps, starting from a thin-film LN on oxidized silicon substrate wafer are explained, as well as a new method for poling the electrodes while observing the resulting output.

4.2.1 Simulation

COMSOL simulations are run to find the optimal device dimensions. The final device cross-section is depicted in Fig. 4.3a. Fig. 4.3b shows the simulations of each mode from the pump to the fourth harmonic in the waveguide, demonstrating that high mode overlap and tight confinement are possible in the ultracompact waveguide. The spacing between the poling electrodes is 8.0 μm,
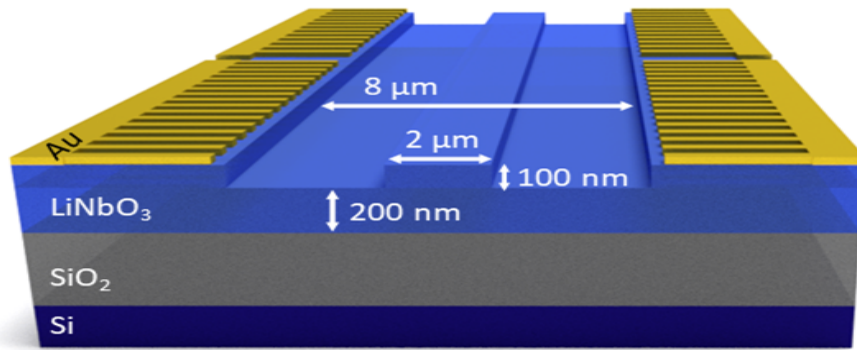
(a)
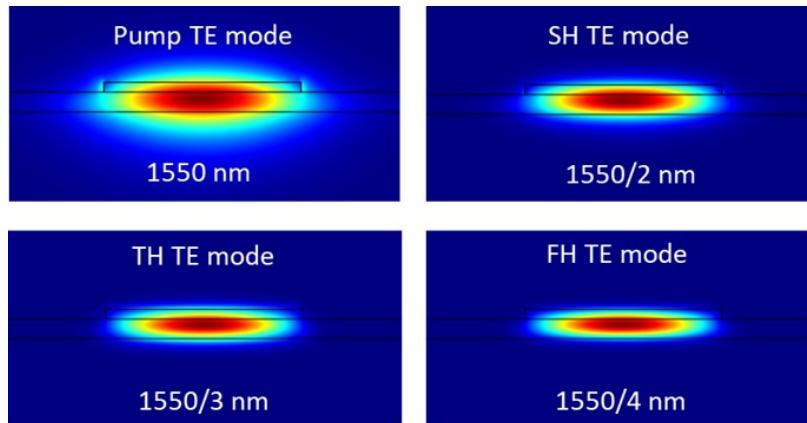
(b)

Figure 4.3: (a) Device cross-section with labeled dimensions. (b) Simulated TE mode images for the pump wavelength and the second-, third-, and fourth-order harmonics.

a distance wide enough to cause minimal interference with the modes, but narrow enough for the applied electric field to exceed the 21 kV/mm coercive field strength of LN necessary for poling the material [60].

The effective index of each of the transverse-electric (TE) modes allows for calculating the optimal poling period for each of the PPLN segments, according to (2.10). The nominal poling period lengths are 2.83, 2.20, and 1.33 μm to generate the second-, third-, and fourth-order harmonics,

36

respectively, of 1550 nm pump light. The duty cycle chosen for the electrode periods is 35%. A small gap (10 μm) is placed between the two PPLN segments to allow each segment to be poled separately, while avoiding inducing additional phase mismatch. Figure 4.4 depicts these electrode poling periods and positioning, as well as the segment lengths.

In reality, to allow for fabrication tolerances and errors in parameters such as etch depth, film thickness, and electrode quality, multiple waveguides are fabricated that vary in width, electrode spacing, and electrode period, such that optimal phase matching can be achieved in one of the devices. However, the values presented above are the central design values, and the parameters of all the devices are varied around these ideal values.
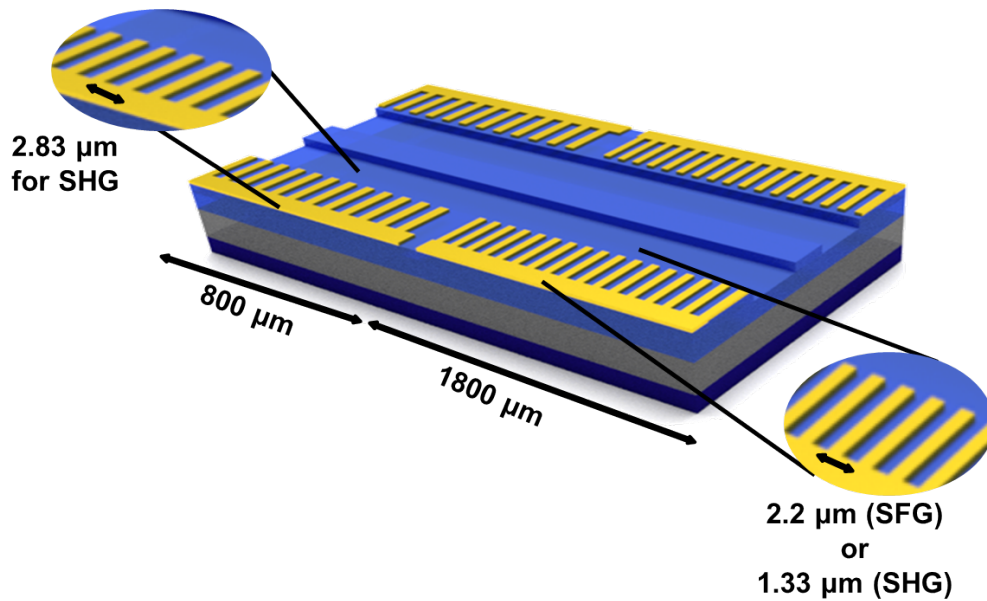
Figure 4.4: Electrode poling periods and device lengths.

4.2.2   Fabrication

The devices are fabricated on 300 nm thin-film *X*-cut lithium niobate (LiNbO$_3$,LN) on a silicon substrate [56]. The first processing step is formation of electrodes for poling. Due to the precision required in fabricating the small dimensions of these electrodes, patterning is performed using electron-beam lithography. After the lithography, the electrodes are formed by depositing thin layers of chrome and gold (10 nm and 100 nm thick, respectively) via electron-beam evaporation. A lift-off procedure is then performed in N-Methyl-2-pyrrolidone heated to 120 °C to form the poling electrodes.

A second electron-beam lithography process is next used to pattern the waveguides. ZEP 520A resist is used in both lithography steps, and the patterns are developed in ortho-xylene developer. The waveguides are formed through dry etching in an argon plasma, with subsequent cleaning steps in an oxygen plasma and a dilute hydrofluoric acid (HF) solution (1:100 49% HF:H$_2$O). The waveguide facets are formed by dicing and polishing. Figure 4.5 shows the main steps of this fabrication process, and more detailed descriptions of the fabrication process and etching recipe are given in Appendices A and B, respectively.

4.2.3   Actively-Monitored Poling

The devices are poled using a poling setup consisting of a function generator to generate the pulses, an oscilloscope to monitor the pulses, a high-voltage amplifier to amplify the voltage pulses by a factor of 100, and two tungsten contact probes to connect to the electrodes on either side of the waveguide. The pulses generated by the function generator are 15 ms square pulses with a 3.7 V amplitude and a repetition period of 5 seconds. Figure 4.6 shows this poling setup.

An actively-monitored iterative poling process is employed for poling the device segments, as
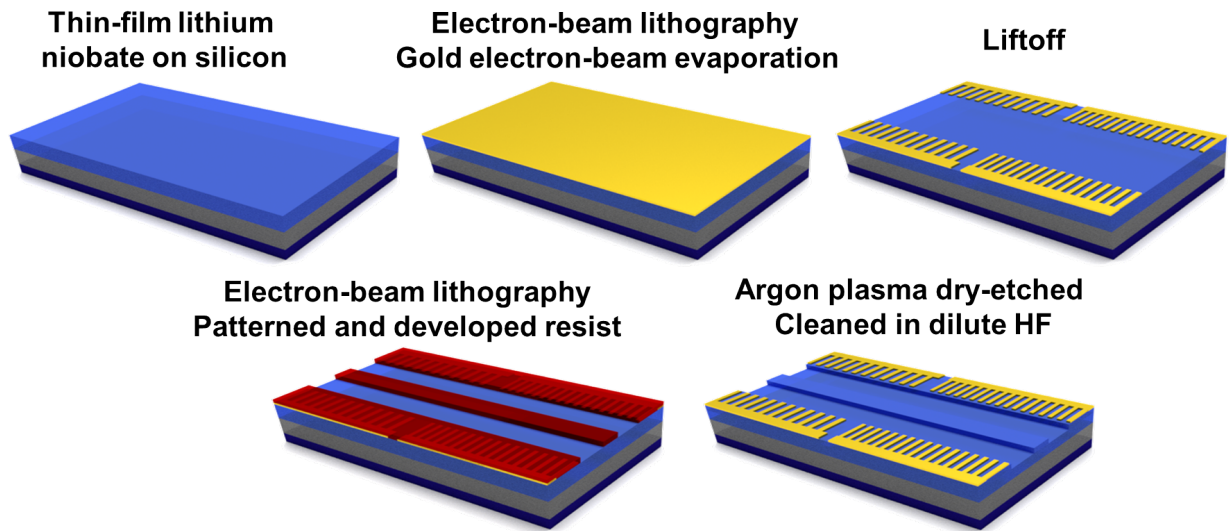
Figure 4.5: Fabrication process for PPLN waveguides.
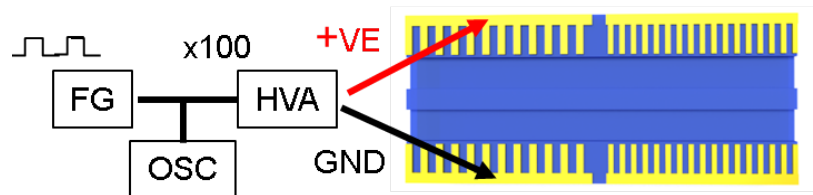
Figure 4.6: Setup for poling.

introduced in Chapter 3 [55]. Before poling, a pulsed laser is lens-coupled into the device, and out-coupled via a lensed fiber that leads to the OSA. At this stage, the OSA shows only the input pulse spectrum, confirming no harmonic generation is produced through unintentional phase-matching in the waveguide. Then, with the OSA continuously scanning, the first segment is poled. The output is monitored and as poling continues, the power of the SH increases. To avoid the possibility of over-poling the device and causing a decrease in conversion efficiency, the poling is stopped after the SH power begins to saturate. Depoling and repoling the segments can increase the conversion

efficiency [55]. The same actively-monitored process is repeated for all remaining PPLN segments. Figure 4.7 shows the OSA trace before poling, after poling only the first segment, and after poling both segments of a THG device. Before either segment is poled there is no harmonic generation. After the first segment is poled, strong SHG is seen, and weak THG and FHG are observed (this phenomenon is discussed later). After the second segment is poled, the TH peak is stronger. These images are from measuring a non-optimized device, and as such the results shown here are strictly for demonstrating the poling process.

4.3 Characterization and Measurement Results

The devices are measured with continuous-wave (CW) and pulsed-input sources to fully characterize their responses. Key results include conversion efficiencies of each of the segments, and seeing higher-order harmonics generated from either CW or pulsed-input light.

4.3.1 CW Characterization

The device is first characterized with a CW source, with the setup shown in Fig. 4.8. The power in the waveguide is measured at both the pump and SH wavelengths, taking coupling loss at the facets into account. The equation for calculating the conversion efficiency in %/W is given in (4.1), where P_ω is the power of the pump in the waveguide and $P_{2\omega}$ is the power of the SH in the waveguide. These powers are measured by use of a photodetector and power meter, and as stated above, the input and output fibers are characterized to calculate the loss they add to the system at both the pump and SH wavelengths, and the facet loss is also calculated, such that the powers used in calculating the conversion efficiency are the pump power that is coupled into the waveguide and the SH power generated by the waveguide, ignoring any external losses. The accordingly-measured
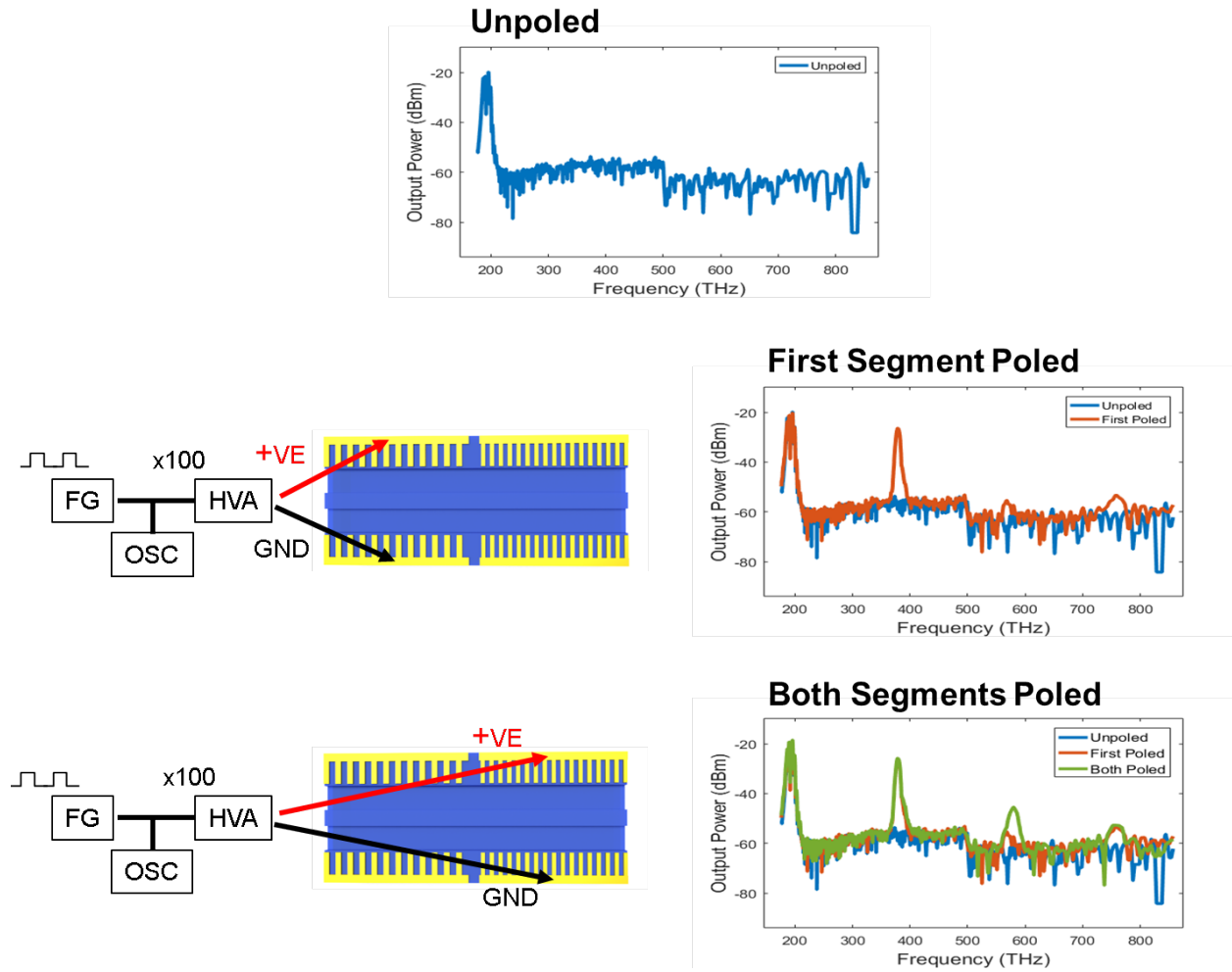
Figure 4.7: Poling process showing OSA trace for (top) both segments unpoled, (middle) first segment poled, and (bottom) both segments poled.

SHG CW conversion efficiencies for the first segment of the THG and FHG devices are 3.84 %/W and 2.56 %/W, respectively.

$$\eta = \frac{P_{2\omega}}{/} P_\omega^2 \tag{4.1}$$
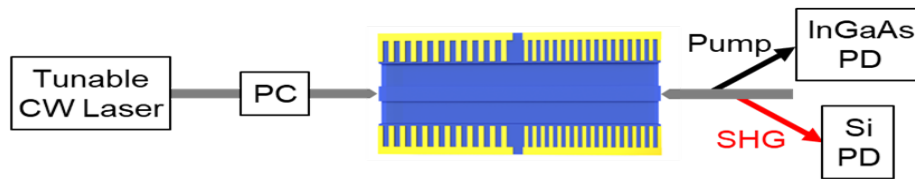
Figure 4.8: CW measurement setup.

CW measurements, even those at high powers through use of an erbium-doped fiber amplifier (EDFA) do not show higher-order harmonic generation. This is likely due to difficulty in achieving the precise phase-matching conditions as described below.

The nature of the cascaded devices means that the output wavelengths of the first segment must be the input wavelengths for the first segment. For the THG device, this means the wavelength of the SH generated in the first segment, and the pump wavelength that generates it, might not satisfy the phase-matching conditions required by the electrode period of the SFG segment. The pump could be tuned to satisfy the phase matching condition, however, tuning the pump means the phase matching conditions of the first segment will no longer be satisfied, and no SH will be generated. This could be addressed by measuring with two tunable lasers at the pump wavelength: one tuned to generate the SH in the first segment, and the other tuned for SFG in the second segment. This measurement was performed, but results are inconclusive. Due to the very precise wavelengths necessary to achieve phase-matching, it is difficult to ensure that the lasers each reach the ideal wavelengths at the same. Even while keeping one laser at the wavelength for maximum SHG, tuning the second input did not show any THG. Additionally, the silicon photodetector used to measure the power of the SH is the same detector used to measure the TH. Thus, it is possible the SH signal hid any detection of the TH. This could be addressed by filtering out the SH at the output so that any power detected could be confidently attributed to the TH. However, such a filter was not available at the time of these measurements.

A similar problem occurs for the FHG device, although with added complication. Since the second SHG segment only depends on the SH wavelength (the pump is not involved in the frequency conversion process in the second segment), adding a second tunable laser at the fundamental wavelength would not solve the problem. Instead, a tunable laser at the SH wavelength is needed, to find the precise wavelength around 775 nm that meets the phase-matching condition of the second segment. Such a source that could be repeatably and precisely tuned was not available at the time of these measurements.

4.3.2 Pulsed-Input Measurements

Therefore, a pulsed source is used to measure the cascaded-harmonic generation (CHG) of the devices at multiple input powers, with the setup shown in Fig. 4.9. The pulsed source generates pulses at 80 MHz repetition rate with a nominal pulse width of ~100 fs.
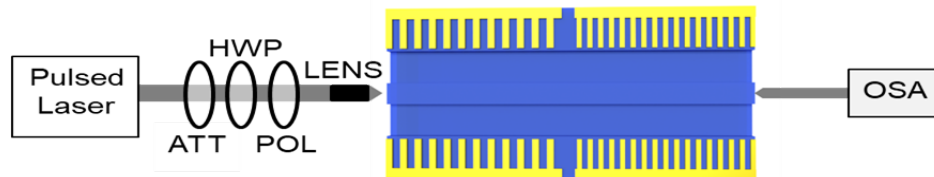
Figure 4.9: Pulsed-source measurement setup.

A pulsed-input source has two advantages over a CW source for this situations. First, it can reach very high peak powers, leading to higher powers in the generated harmonics. Second, its broad bandwidth means that the two different phase matching conditions of the two segments in each device can be satisfied simultaneously with a single input source.

Figure 4.10a images the OSA data for each input pulse energy, showing how the power in each harmonic varies with input pulse energy for the THG device, and Fig. 4.10b displays the OSA

traces for three of these input pulse energies.

From the spectra for the maximum input pulse in Fig. 4.10b, it can be seen that the power level of the generated TH is comparable to that of the SH, indicating an efficient conversion process. However, while the broad bandwidth of the pulse allowed for the cascaded generation of the harmonics, it complicates the process of measuring the conversion efficiencies. The conversion efficiency of the data from a pulsed-source cannot be extracted in the same straightforward way as for a CW input. This is due to complexities arising from the difference between the peak and average powers, the broad and spectrally-rich bandwidth, and the phase components of the pulses. A method for determining the conversion efficiency when measured with a pulsed source is discussed below in Chapter 5, and quantitative results are reported. As can be seen in Figure 4.10b, a small amount of FH is generated by the THG device. Experimentally, this is likely due to non-optimized SHG of the SH and non-optimizied SFG between the pump and the TH.

The FHG device is characterized similarly. Figure 4.11a images the OSA traces for each of the input pulse energies, showing how the power in each harmonic grows with increasing input pulse energy for the FHG device. Figure 4.11b displays the OSA traces for several of these input pulse energies.

From the spectra for the maximum input pulse in Fig. 4.11b, it can be seen that the power level of the generated FH is comparable to that of the SH, again indicating efficient conversion. Quantitative results are reported Section 5.3. Again, Figure 4.11b shows a small amount of TH is generated by the FHG device. Experimentally, this is likely due to non-optimized SFG between the pump and the SH.
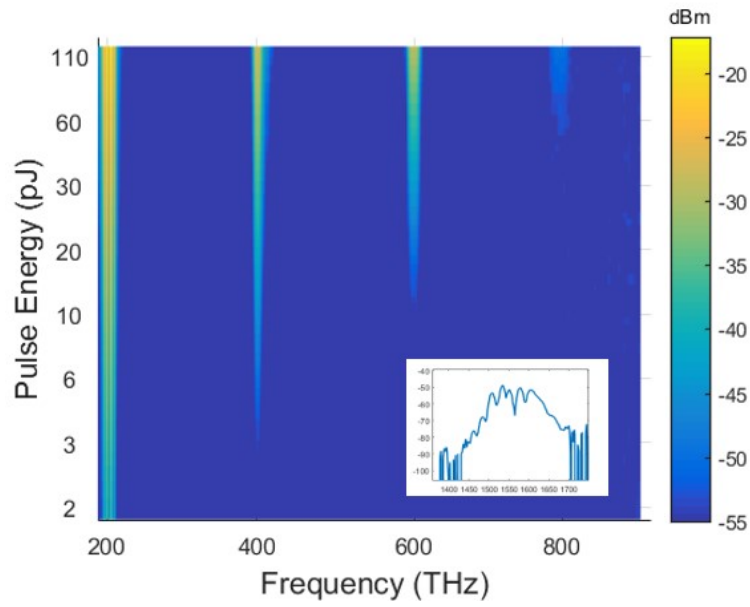
(a)
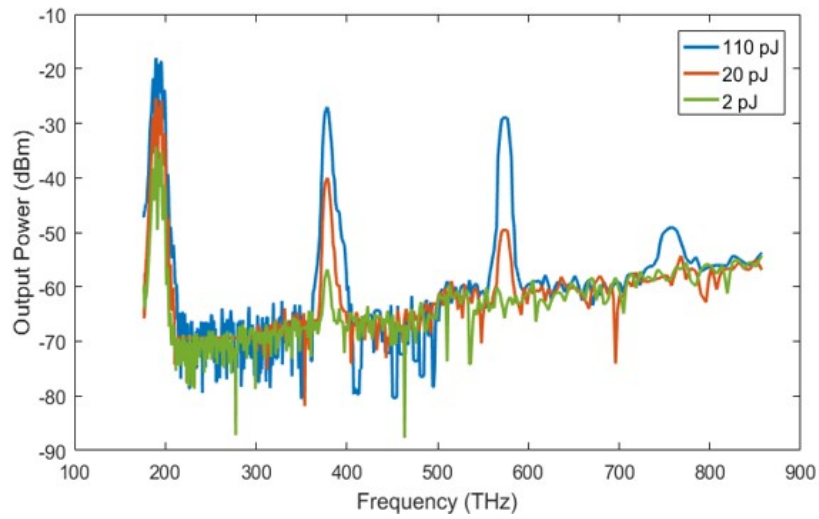
(b)

Figure 4.10: (a) CHG (optimized for THG, see Fig. 4.1) as a function of input pulse energy. (Inset: input pulse spectrum) (b) CHG measured in dBm for several input pulse energies.
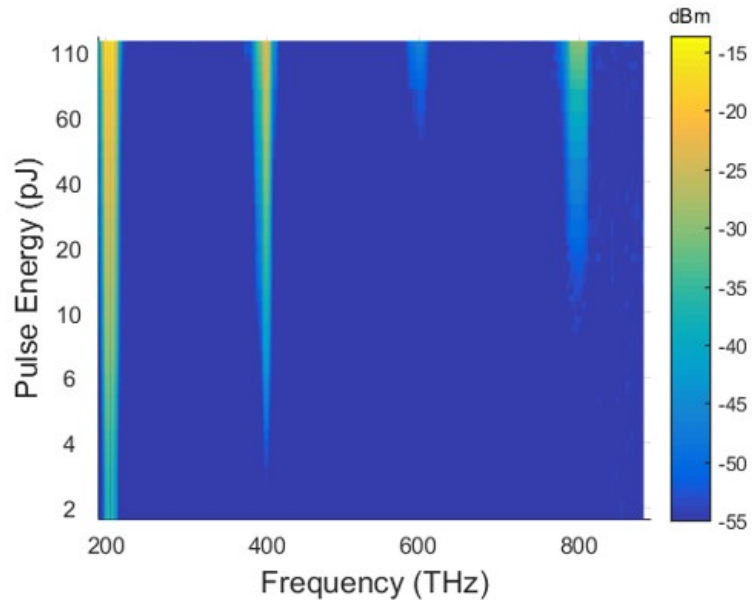
(a)
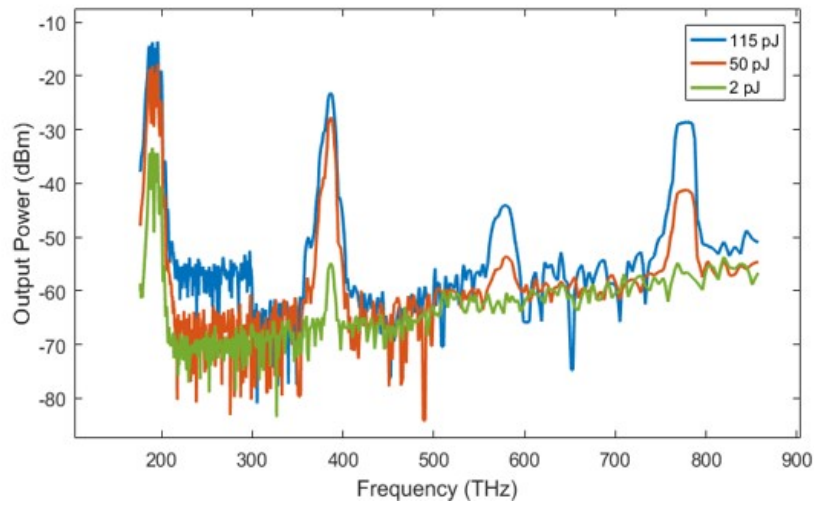
(b)

Figure 4.11: (a) CHG (optimized for FHG, see Fig. 4.2) as a function of input pulse energy. (b) CHG measured in dBm for multiple input pulse energies.

4.4 Conclusions

Cascaded $\chi^{(2)}$ nonlinear PPLN segments can be used to generate higher-order harmonics, and that is demonstrated in this work for the first time in thin-film lithium niobate on silicon waveguides. In this work, cascading SHG and SFG segments produces third-harmonic generation, and cascading two SHG segments produces fourth-harmonic generation. The design and simulation process are discussed, in addition to the fabrication steps. An optically-monitored poling system is presented, allowing for harmonic generation results to be seen during the poling process. This allows the poling process to be repeated until maximum efficiency is attained. CW measurements show strong SHG in the first segments of the devices. When the devices are measured with a pulsed input to characterize the cascaded processes, the resulting spectra show efficient frequency conversion to the third- and fourth-order harmonics. However, due to using a pulsed source for measurements, the conversion efficiencies cannot be calculated in the same way and devices measured with CW light. This is addressed in the following chapter.

CHAPTER 5: MODELING PULSED-INPUT HARMONIC GENERATION

As discussed above, determining the conversion efficiency is more complicated for measurements performed with a pulsed source as opposed to a CW input. Thus, a simulation is written to model the harmonic generation process with a pulsed input, and the conversion efficiency can be extracted from the best-fit results. The model itself is presented, with a discussion of the involved equations and their solution method. The process of applying it to the devices of Chapter 4 is detailed, and the simulation results are compared to the measured results. The conversion efficiencies of the cascaded segments are extracted.

5.1   Theory and Equations

The model solves the nonlinear Schrödinger equation for coupled modes with second-order non-linearity for SHG and SFG. Partial differential equations (5.1), (5.2), and (5.3) describe the pulse shapes of the waves involved in the nonlinear conversion processes, as they propagate through the waveguide. The set of equations is generalized to describe SHG, SFG, and cascaded SHG, with terms being turned on or off depending on the specific process being described. The subscript indices *1* and *2* refer to the pump and SH, respectively. A subscript *3* is used to denote the third wave in the cascaded process. This third wave can be either the TH or the FH, depending on the process (TH for SFG, FH for cascaded SHG). The linear terms such as loss and dispersion, denoted by the overbraces, make up the linear operator, and the nonlinear terms for both harmonic generation and kerr nonlinearity, denoted by the underbraces, make up the nonlinear operator. These operators are

discussed further in following sections.

$$\frac{\partial A_1}{\partial z} = (a-1)\Delta\beta_1 \frac{\partial A_1}{\partial \tau} - \frac{i}{2}\beta_{2,1}\frac{\partial^2 A_1}{\partial \tau^2} - \frac{\alpha_1}{2}A_1 +$$
$$i\kappa_{p,1}A_q \exp\left[i\Delta k_p z\right] + i\gamma_1\left(|A_1|^2 + 2|A_2|^2 + 2a|A_3|^2\right)A_1 \tag{5.1}$$

$$\frac{\partial A_2}{\partial z} = -a\Delta_{2,1}\beta_1 \frac{\partial A_2}{\partial \tau} - \frac{i}{2}\beta_{2,2}\frac{\partial^2 A_2}{\partial \tau^2} - \frac{\alpha_2}{2}A_2 +$$
$$i\kappa_{p,2}A_r \exp\left[i\Delta k_p z\right] + i\gamma_2\left(2|A_1|^2 + |A_2|^2 + 2a|A_3|^2\right)A_2 \tag{5.2}$$

$$a\frac{\partial A_3}{\partial z} = -a\Delta_{3,1}\beta_1 \frac{\partial A_3}{\partial \tau} - \frac{i}{2}a\beta_{2,3}\frac{\partial^2 A_3}{\partial \tau^2} - \frac{\alpha_3}{2}aA_3 +$$
$$ia\kappa_{p,3}A_s \exp\left[-i\Delta k_p z\right] + ia\gamma_3\left(2|A_1|^2 + |2A_2|^2 + |A_3|^2\right)A_3 \tag{5.3}$$

These equations governing higher-harmonic processes are expanded versions of the partial differential equations that describe the evolution of the fundamental and second-harmonic pulses in a waveguide [62, 41]. The subscript p indicates the selected conversion process, either SHG, THG, or FHG. a is a multiplier to effectively turn off portions of the equations as necessary depending on the process being modeled, and is equal to 0 for SHG, and 1 for THG and FHG processes. $A_q = A_2 A_1^*$, $A_3 A_2^*$, or 0, $A_r = A_1^2$, $A_3 A_1^*$, or $A_3 A_2^*$, and $A_s = 0$, $A_1 A_2$, or A_2^2, for SHG, THG, and FHG, respectively. Some of the variables in the equations combine other variables for more

condensed notation, as shown below in (5.4).

The coupling coefficients for each process, κ_p, are defined according to the equations below in (5.5). The theoretical limit for the conversion efficiency is given by η.

$$\gamma_j = \frac{n_2 \omega_{0,j}}{c A_{eff,j}}, j = 1, 2, 3$$

$$\Delta\beta_1 = \frac{1}{v_{g,1}} - \frac{1}{v_{g,2}} \tag{5.4}$$

$$\Delta_{k,1}\beta_1 = \frac{1}{v_{g,k}} - \frac{1}{v_{g,1}}, k = 2, 3$$

$$\kappa_{SHG,1} = \kappa_{SHG,2} = \kappa_{SHG,3} = \sqrt{\frac{8d_{33}^2}{\epsilon_0 c n_{0,2}^2 n_{0,1} \lambda_{2\omega}^2 S_{eff,1}}}$$

$$\eta_{SHG} = \kappa_{SHG}^2$$

$$\eta_{SFG} = \frac{2\omega_{0,1}\omega_{0,2}d_{33}^2}{\pi^2 \epsilon_0 c^3 n_{0,1} n_{0,2} n_{0,3} S_{eff,3}} \tag{5.5}$$

$$\kappa_{THG,j} = \frac{\sqrt{\eta_{SFG}}}{\sqrt{\omega_{0,1}\omega_{0,2}}} \omega_{0,j}, \text{for } j = 1, 2, 3$$

$$\kappa_{FHG,1} = \kappa_{FHG,2} = \kappa_{FHG,3} = \sqrt{\frac{8d_{33}^2}{\epsilon_0 c n_{0,3}^2 n_{0,2} \lambda_{4\omega}^2 S_{eff,2}}}$$

$$\eta_{FHG} = \kappa_{FHG}^2$$

In the equations in (5.5), the variables are defined as follows. c is the speed of light in vacuum, and ω_j is the center frequency of the given harmonic. The refractive index of LN for the wavelength of the given harmonic is $n_{0,j}$, and the third-order nonlinear refractive index is noted as n_2, the value of which is 10×10^{-16} cm^2/W, and $d_{33} = 33$ pm/V is the largest intrinsic nonlinear susceptibility

coefficient of LN. The loss incurred along the waveguide for each harmonic is α_j. $v_{g,j}$ is the group velocity and $\beta_{2,j}$ is the group velocity dispersion of each wave. Δk_p is the wavevector mismatch for each nonlinear process, z measures distance in the propagation direction, $A_{eff,j}$ is the overlap area between the mode and the LN, and $S_{eff,j}$ is the overlap surface integral between the interacting modes. The model does not assume perfect phase matching by setting $\Delta k = 0$; instead, it accounts for the domain reversal from periodic poling and the sign of d_{eff} is flipped between ± 1 to invert the domain orientation of the LN. The domain orientations are flipped according to the dimensions of the poling period of the fabricated electrodes. Δk_p is then finely tuned to precisely match the phase matching condition returned by the measured results.

Directly flipping the sign of d_{eff} to invert the domain orientation allows the results from nonuniformity or damaged electrodes to be modeled as well. For example, in the case of damaged electrodes, poling might not occur at every period along the wavelength. To simulate this, the model can be made to not invert specific domains. For the case of nonuniformity, a gradually-increasing film thickness would change the phase-matching condition, phase-matching instead at a different wavelength. If this phenomenon is strong enough, it could broaden the range of wavelengths over which phase-matching, and thus harmonic generation, occurs.

5.2   Solution Method

The partial differential equations are solved using the symmetrized split-step Fourier method [63, 64] at each small dz along the length of the waveguide. This algorithm is implemented in Matlab, and is tested and found to be numerically stable. The model does not consider higher-order modes, as mode-overlap simulations show very small overlap between the fundamental SH mode and the third-order TH and FH modes, and thus and harmonic generation resulting from higher-order modes is negligible.

5.2.1 Symmetrized Split-Step Fourier Method

With the split-step Fourier method, the linear operator (again, denoted by the overbraces in (5.1), (5.1), and (5.1)) are accounted for in the frequency domain, whereas the nonlinear operators (again, denoted by the underbraces in (5.1), (5.1), and (5.1)) are applied in the time domain. The SHG is accounted for by adding an additional linearized driving term to avoid dividing by small numbers. While some error is accumulated due to the oversimplification of assuming the linear and nonlinear operators can be split apart, the error is minimized by propagating over a small step size dz.

The symmetrized split-step Fourier method used here (as opposed to the standard, non-symmetrized method) further minimizes this error by applying the linear operators to the first half of the dz, then applying the nonlinear operators over the entire dz, and finally applying the linear operators to the second half of the dz, as opposed to the non-symmetrized method that does not apply the linear operators this way in two steps. Instead, the standard, non-symmetrized method applies the linear operator over the entire dz segment at once, followed by the nonlinear operators, also over the entire dz segment at once. This symmetrized split-step Fourier method is visualized in Fig. 5.1, where the method is applied along a waveguide of length L, divided into segments of length dz. The flowchart underneath the waveguide describes how the operators are applied. In practice, the dz segments are very small compared to waveguide length, but are shown large here simply for demonstration purposes.

5.3 Applying Model to Characterize Cascaded Devices

The input pulse used in the model is formed by taking the pulse spectrum in frequency domain from an OSA measurement of the pulse used in the experimental measurement, and converting the data into time domain. This ensures the pulse used for the simulation contains the same spectral
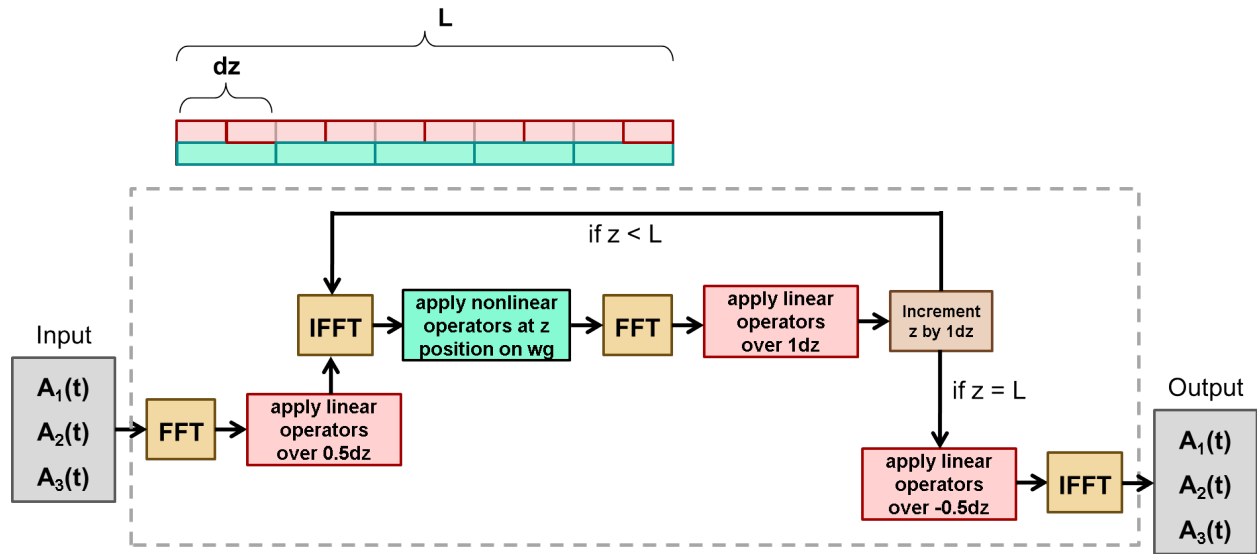
Figure 5.1: Visualization of the symmetrized split-step Fourier method for solving nonlinear Schrödinger equation for coupled modes with second-order nonlinearity for SHG and SFG.

components as the pulse used in the experimental measurements. Chirp is added to the pulse to produce a quadratic phase, and the chirp parameters are tuned such that the simulation output for a test case matches known results.

The CW conversion efficiencies measured experimentally for the first segments of both devices are set as constants in the model. The simulated SHG spectra of the first segment for both the THG and FHG devices are comparable to the experimental results. The conversion efficiencies for the second segments are returned by the model by varying the parameters to achieve a best fit between the simulated and measured results.

5.4   Model Results for Cascaded Devices

The model is used to simulate the harmonic generation occurring in the cascaded devices. The results of the first segments with known conversion efficiencies match well, giving credibility to the model and the results for the cascaded segments.

5.4.1   THG Results

Figure 5.2 compares the experimentally-measured spectra to the results returned by the simulation for the THG device, demonstrating agreement between the results. The plots correct for the loss experienced by each wavelength from the OSA. Extracting the conversion efficiency from the model gives $28.8 \pm 8.5\%$/W for the SFG conversion process for generating the TH. The uncertainty in the conversion efficiency comes from adding a $\pm 5\%$ change to simulation parameters and extracting the resulting range of conversion efficiencies. This is due to uncertainty in the precise phase-matching conditions in the sample, limitations of the simulation process, and subjectivity in determining the coupling coefficient that best fits the data. The output is evidently very sensitive to small changes in many of the input parameters.

5.4.2   FHG Results

Figure 5.3 compares the experimentally-measured spectra to the simulation results, again correcting for the OSA loss for each wavelength. Extracting the conversion efficiency from the simulation gives $10.0 \pm 1.2\%$/W for the SHG-based FH conversion process. As with the THG case, the uncertainty in the conversion efficiency comes from adding a $\pm 5\%$ change to simulation parameters and extracting the resulting range of conversion efficiencies.
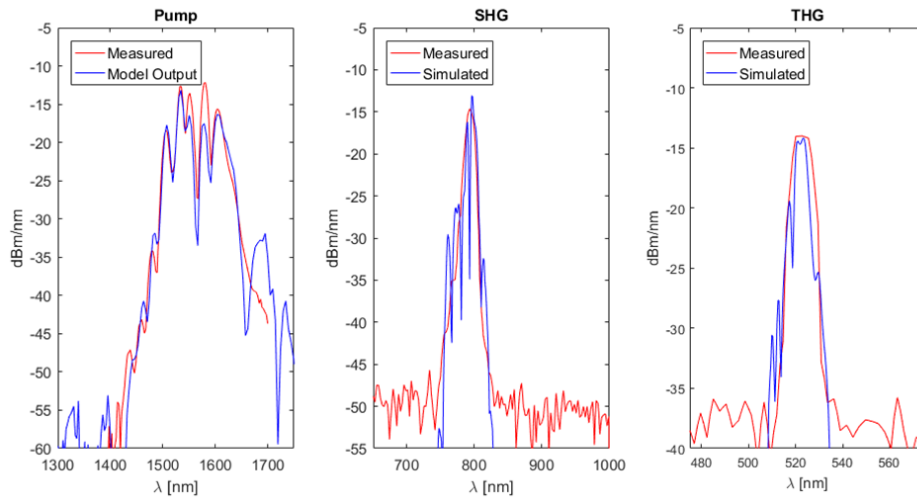
Figure 5.2: Comparison of the measured and simulated spectra for (from left to right) the pump, SH, and TH.
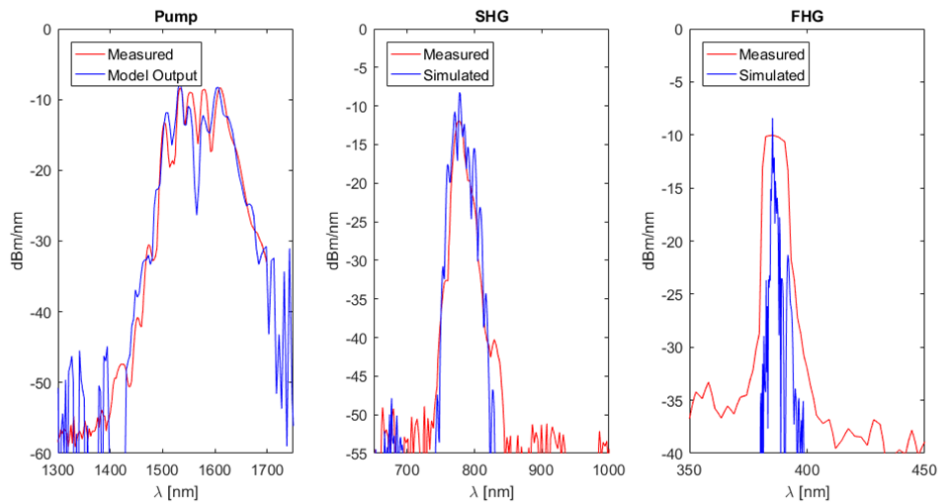
Figure 5.3: Comparison of the measured and simulated spectra for (from left to right) the pump, SH, and FH.

The linewidth of the measured TH and FH is broader than the initial model predicted (not shown here), and so measures were taken to improve the model. Particularly, possible nonuniformity in film thickness along the waveguide would gradually change the phase-matching condition, causing slight shifts in the generated wavelength, as discussed above. This phenomenon would broaden the TH and FH peaks. This fabrication nonuniformity is implemented in the model by adding a linear ramp to the phase-matching condition along the length of the device, around the center wavelength. This effectively broadens the TH and FH peaks and achieves a good fit to the experimental measurements, especially for the THG device as can be seen in Fig. 5.2. The FH peak from the model is narrower than the measured peak, even after adding the above-mentioned nonuniformity to the model. The reasons for this are not yet well understood.

5.5   Conclusions

In conclusion, a numerical model is presented for simulating the harmonic generation that occurs in the cascaded devices of Chapter 4 when measured with a pulsed-source input, in order to characterize and quantify the conversion efficiencies of the cascaded segments. The model solves the nonlinear Schrödinger equation for coupled modes with second-order nonlinearity for SHG and SFG by employing the symmetrized split-step fourier method. The equations and solution method are presented in detail, highlighting the ability to simulate the results of fabrication nonuniformity. The model is applied to the cascaded devices, and the measured and simulated results are compared. The conversion efficiencies of the cascaded segments are extracted from the model. The conversion efficiencies returned by the model are 28.8 ± 8.5%/W for the SFG conversion process for generating the TH, and 10.0 ± 1.2%/W for the SHG conversion process for generating the FH.

CHAPTER 6: SPATIALLY-MAPPED ANISOTROPIC PHOTONICS

In this chapter, the need for polarization-diverse photonics is presented. Examples of applications where polarization-selective devices are necessary are discussed, along with a summary of the types of devices required for these processes. Current device implementations to address these requirements are discussed, and their limitations and disadvantages are studied. Finally, a new platform to overcome these challenges is introduced. Additionally, the results of fabricated polarization-selective devices are presented, showing large improvements over current technology.

6.1 Polarization Diversity

Bipolarized light contains both transverse-electric (TE) and transverse-magnetic (TM) polarized light, where with TE the electric field is transverse to the direction of propagation, and with TM the magnetic field is transverse to the direction of propagation, as depicted in Fig. 6.1. Polarization-diverse transmitter and receivers are becoming even more desirable across a wide variety of applications, including high-bandwidth telecommunications [65], optical coherence tomography [66, 67, 68], remote spectroscopy [69], polarimetric light detection and ranging (LIDAR) [70], and spaceborne optical polarimetry [71], among others. Thus, having a platform that can effectively process light of both orthogonal polarization states is important.

Polarization division multiplexing is another example of an implementation requiring this polarization-diverse processing [72, 73]. Polarization division multiplexing is a method of multiplexing in which two information channels can be transmitted on the same carrier frequency, one for each orthogonal polarization state, unlike wavelength division multiplexing where two different carrier frequencies are necessary, thus doubling the amount of information that can be transmitted [74, 75, 76]. Again,
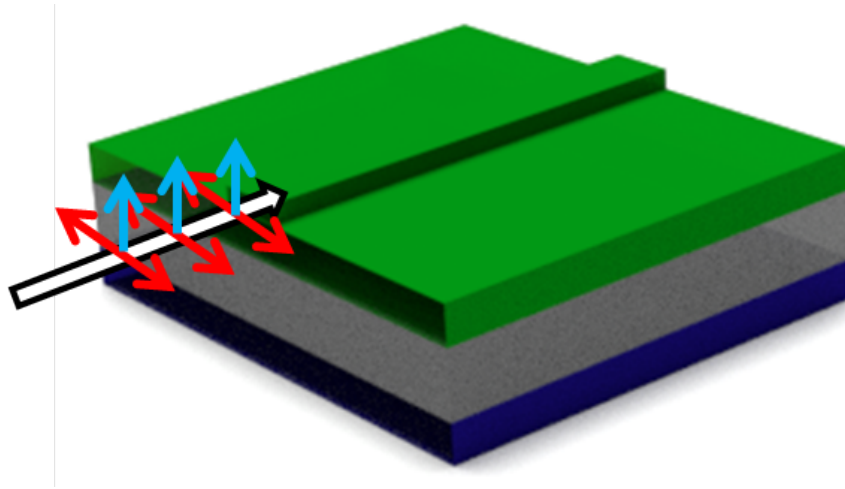
Figure 6.1: Bipolarized light entering a waveguide, with TE- (red arrows) and TM-polarized (blue arrows) light.

having a platform that can route and process light of orthogonal polarizations is essential to the operation of polarization division multiplexing.

The SOI photonics platform is sensitive to polarization due to the large birefringence present in the ultra-compact waveguides [72, 77]. Rather than trying to decrease this polarization sensitivity inherent to the platform, a polarization-diverse system can be employed where each polarization is routed and processed separately [78, 79]. This splitting process is done by using polarization beam splitters (PBS). This concept is illustrated in Fig. 6.2. Alternatively, one polarization state can first be rotated using a polarization rotator (PR) to its orthogonal state, and thus the same polarization states can be processed together. High-performing PBS and PR devices are important for the applications discussed above [72, 80, 81, 82].
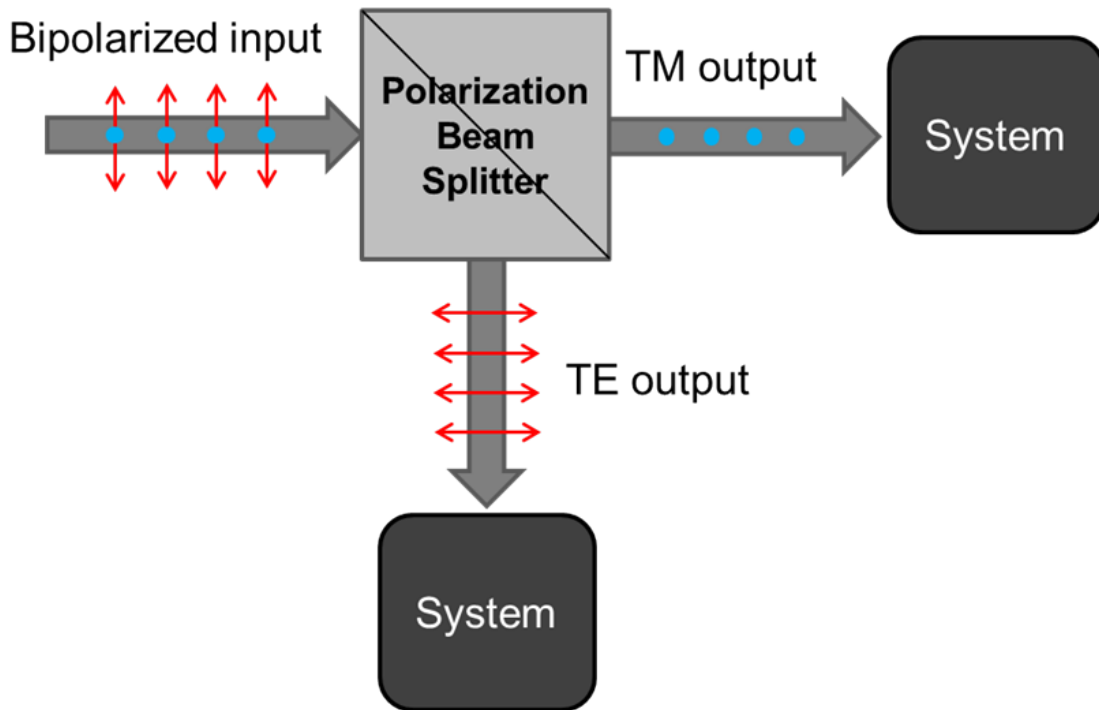
Figure 6.2: A bipolarized input can be split into two orthogonal polarizations and processed separately.

6.2 Polarization-Diverse Device Approaches

A review of methods and implementations to achieve the PBS and PR devices discussed above is presented in this section. Disadvantages of certain approaches are discussed, and finally an overview of the current-best integrated technology is presented.

6.2.1 Polrization Beam Splitters

There are three most common types of PBS devices based on integrated structures.

First, the birefringence of Mach-Zehnder interferometers can be used to split apart orthogonal

polarizations [83, 84, 85, 81, 74], However, the birefringence is small and does not allow for a robust splitting process.

Multimode interference structure approaches have also been implemented for polarization splitting, taking advantage of the difference of beat lengths of the orthogonal polarizations [86, 87, 88, 89, 90]. However, this approach requires extremely long devices, incurring excess loss.

Directional couplers are a third method for implementing PBS devices [91, 92, 93, 94]. The length of the coupling region is calculated to satisfy given conditions relating the coupling lengths of each polarization [72]. While simple to fabricate, this approach also requires long devices due to weak birefringence in the waveguide, and due to the specific conditions for coupling lengths required for splitting the polarizations, the approach is not broadband.

6.2.2   Polarization Rotators

Polarization rotators are more complicated for realization with integrated approaches, as waveguides are typically polarization-maintaining devices. In waveguides, it is not possible to rotate the optical axis to induce polarization rotation. Instead, asymmetry must be introduced in some way.

Previous implementations of this introduced asymmetry include double-core waveguides [79], bi-level tapers [95, 96], and waveguides with slanted cores [97, 98]. These approaches involve long and/or complicated fabrication processes.

Another approach to polarization rotation is to combine a PBS and PR into a single polarization splitter-rotator (PSR). With these devices, the mode of one polarization is converted to a higher-order mode of the orthogonal polarization. This approach, typically taking advantage of the directional coupler PBS implementation, has been demonstrated in [99, 100, 101, 102]

6.2.3 *Current Best Technology*

The results of several of the best-performing integrated broadband polarization-selective devices are summarized in Table 6.1.

Table 6.1: Current-best broadband integrated polarization-selective devices

Work	Device	Bandwidth (nm)	Max insertion loss (dB)	Min. ER (dB)
Xiong [103]	TE-pass polarizer	110	0.4	30
Shahin [104]	TM-pass polarizer	110	2.4	18
Tan [99]	PSR	100	~2	~18
Kim [91]	PBS	100	2.1	22.5
Su [105]	PBS	150	3.4	10

The PBS in the above table both rely on specifically-designed coupling regions to split the polarization states [91, 105]. While these approaches have semi-high extinction ratios, their dependence on mode-coupling results in a smaller operation bandwidth.

Each of these devices are engineered to make the best use of the dissimilar electric field distributions of the transverse electric (TE) and transverse magnetic (TM) modes. Sub-wavelength structures have been used to realize stronger differentiation between polarizations [103, 104]. The bandwidths of these approaches are limited by the wavelength dependence of the field distribution.

Devices with lower insertion losses across a broader bandwidth are necessary for high-performing polarization-diverse circuits. Current technology is unable to achieve these optimistic conditions.

6.3   Platform Concept

As seen in the previous section, it is difficult to make polarization-selective devices as the devices depend on the difference of the distribution of the electric field between the TM and TE modes,

and this distribution is wavelength-dependent. Additionally, for tightly-confined modes, such as at shorter wavelengths, the field distributions between the polarizations become more similar, further limiting the bandwidth of such devices.

For a different approach, rather than trying to take advantage of the modal birefringence of the material, the anisotropy of the material itself can be manipulated. If a waveguide is made with a uniaxial anisotropic core, where the extraordinary axis is perpendicular to the substrate, and the ordinary index is higher than the extraordinary index, there is an enhanced birefringence between the TE and TM modes, even at short wavelengths. This material becomes more useful if it can be spatially mapped across a sample. By mapping this material anisotropy on the chip, devices can be designed that make use of this enhanced birefringence. This process was used to demonstrate a PBS [106]. This mapped anisotropy concept has also been demonstrated with polymers [107, 108], organic crystals [109], and anisotropic overlayers [110, 111].

This anisotropic material can be used in a waveguide to create polarization-selective waveguides, where only one polarization is guided, and the orthogonal polarization is rejected from the core [112]. If a waveguide is formed by an anisotropic material and an isotropic material, where the value of the refractive index of the isotropic material is less than the TE effective index of the anisotropic material, and is greater than the TM effective index of the anisotropic material, two types of structures can be made.

If the anisotropic material is placed as the core of the waveguide and the isotropic material is placed as the side cladding, only TE light will be guided, and TM light will be rejected from the core. However, if the positions of the materials are swapped and the anisotropic material becomes the cladding and the isotropic material is in the core, then only TM light will be guided and TE light is rejected from the core. This waveguide geometry is depicted in Fig. 6.3. These refractive index requirements and waveguide configurations are given by. (6.1). This concept forms the basis of the
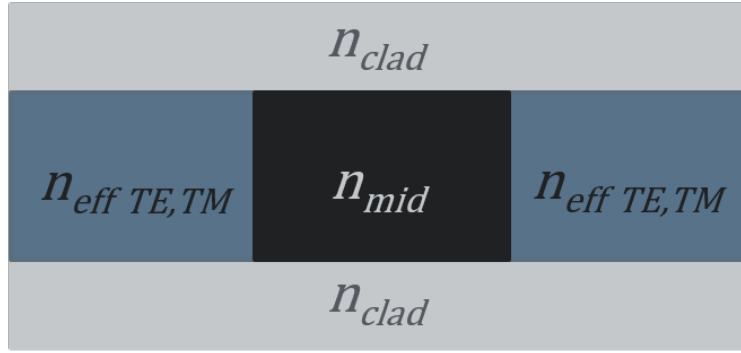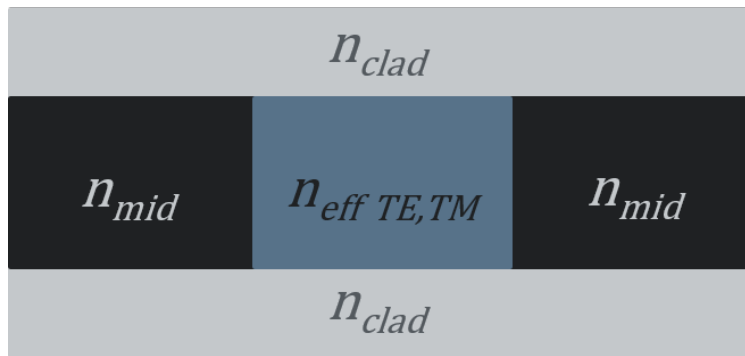
Figure 6.3: Waveguide materials configuration for (a) TM-only and (b) TE-only.

Spatially-Mapped Anisotropic Photonics platform.

$$n_{clad} < n_{eff,TM} < n_{mid} < n_{eff,TE} \qquad (6.1)$$

An anisotropic material that satisfies these requirements can be created by alternating thin layers of high and low refractive index materials to create a multilayer stack (MLS). From effective medium

theory [113], the birefringence in the material indices can be described by (6.2), where H and L denote the high- and low-index material, respectively, and f is the fill fraction of the high-index material. These equations apply since the thickness of the layers (on the order of 20 nm) is much less than the wavelength.

6.4 Platform Design

The materials used to create the MLS are silicon dioxide (SiO_2) (low-index material) and silicon nitride (Si_3N_4) (high-index material). The isotropic material is silicon oxynitride (SiON), the refractive index of which is tuned to be between the values of the TE and TM effective indices by adjusting the material composition during deposition. For this work, the MLS has a TE effective index of 1.715 and a TM effective index of 1.65, and the refractive index of the SiON is 1.68, when measured with 633 nm light. Fig. 6.4 shows an updated diagram of the TE- and TM-only waveguides, now showing the MLS as the anisotropic material.

$$n^2_{eff,TE} = f n^2_H + (1-f) n^2_L$$
$$\frac{1}{n^2_{eff}} = \frac{f}{n^2_H} + \frac{(1-f)}{n^2_L} \tag{6.2}$$

6.4.1 Simulation

Lumerical MODE Solutions™ simulations have been run to confirm these waveguides are single-polarization over a broad bandwidth. As expected, the waveguide structures only guide one polarization, and no modes are returned for the orthogonal polarizations. This confirms polarization selectivity, giving confidence to continue developing the platform. Figure 6.5 shows these TE and

TM-Selective Waveguide

(a)

TE-Selective Waveguide

(b)
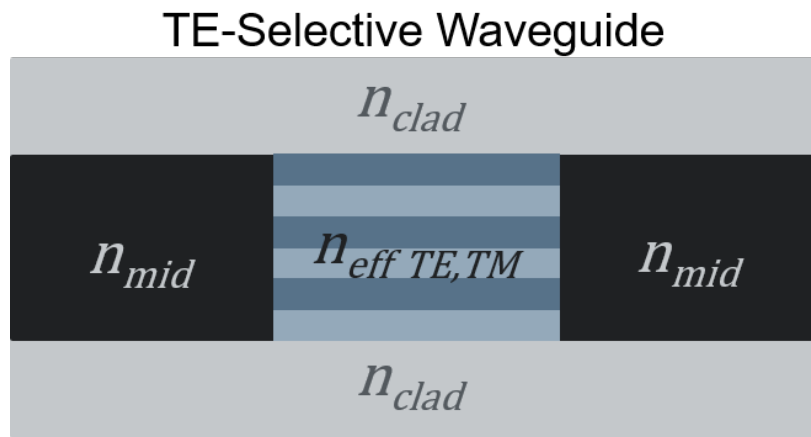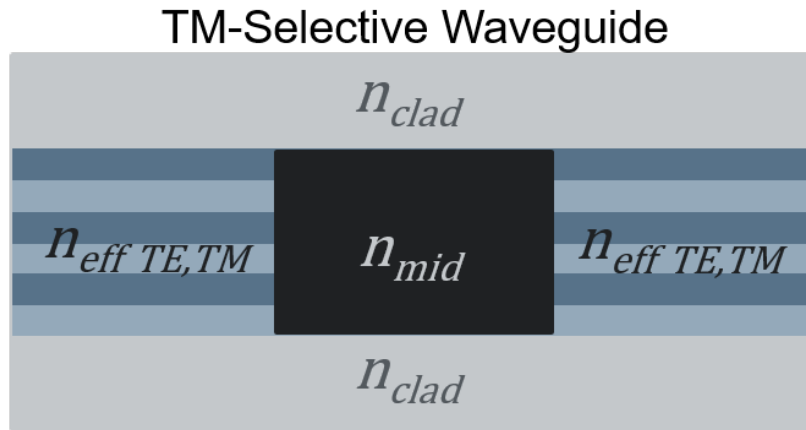
Figure 6.4: Waveguide materials configuration for (a) TM-selective device and (b) TE-selective device containing MLS as the anisotropic material.

TM mode profiles in the waveguide structures shown in Fig. 6.4.
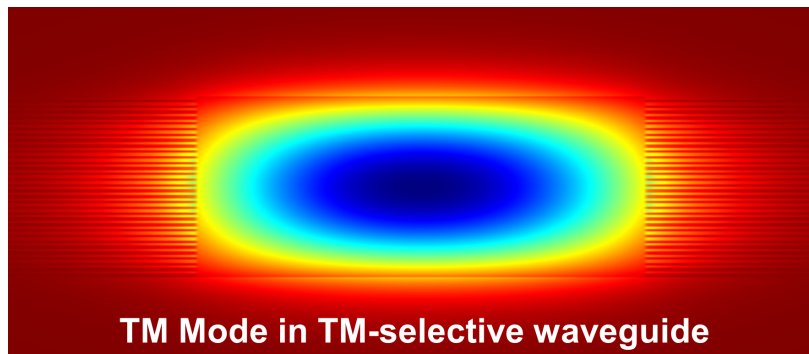
(a)
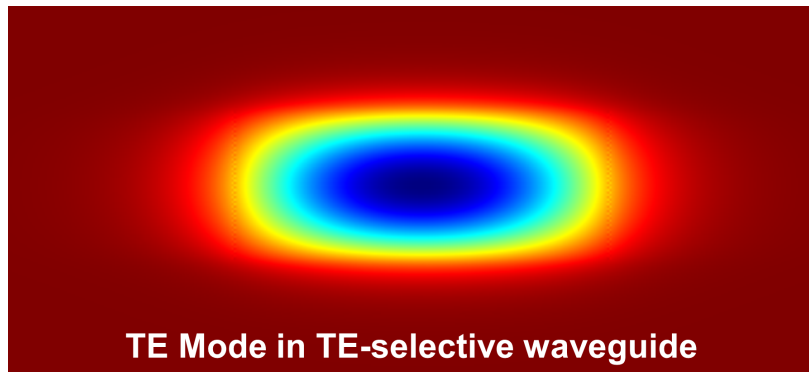
(b)

Figure 6.5: Mode profiles in the waveguide structures of Fig. 6.4.

6.4.2 Fundamental States

The TM- and TE-only waveguides make up the fundamental states of the spatially-mapped anisotropic photonics platform, along with a bipolarized waveguide formed by a SiON core and a SiO_2 side cladding, which guides both TE and TM light. These fundamental states are shown in Fig. 6.6.

Fundamental States
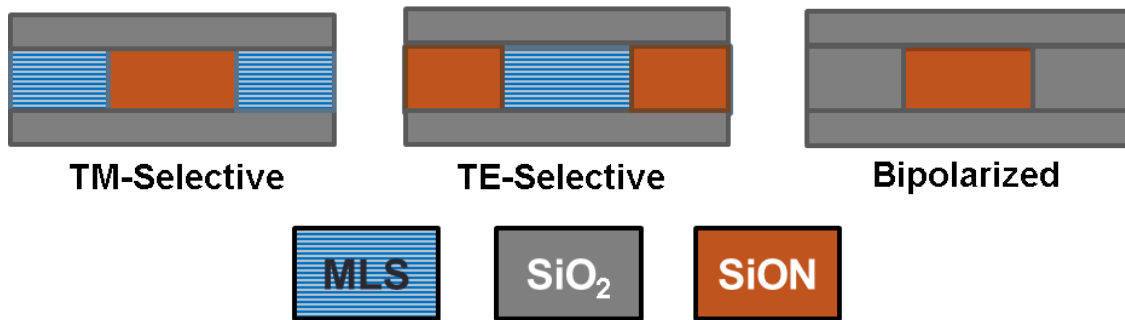
Figure 6.6: Fundamental states showing single-polarization and bipolarized waveguide material configurations.

6.4.3 Hybrid States

The fundamental states can be combined to create hybrid states that contain two waveguide cores (both MLS and SiON), with a SiO_2 cladding. When the two different cores are beside each other, TE-polarized light favors the MLS core, and TM light favors the SiON core. These hybrid states are shown in Fig. 6.7. Also shown is a mode simulation showing how the TE and TM modes are split in space for the Asymmetric Coupled Hybrid state, where the MLS and SiON cores are adjacent.

6.5 Platform Fabrication

The fundamental and hybrid states that make up this platform are fabricated as described below. The process starts with an oxidized silicon wafer. The wafer is cleaved down to sample size, and the MLS is deposited by plasma-enhanced chemical vapor deposition (PECVD), alternating between the SiO_2 and Si_3N_4 layers. The sample is coated with ZEP 520-A electron-beam resist, and
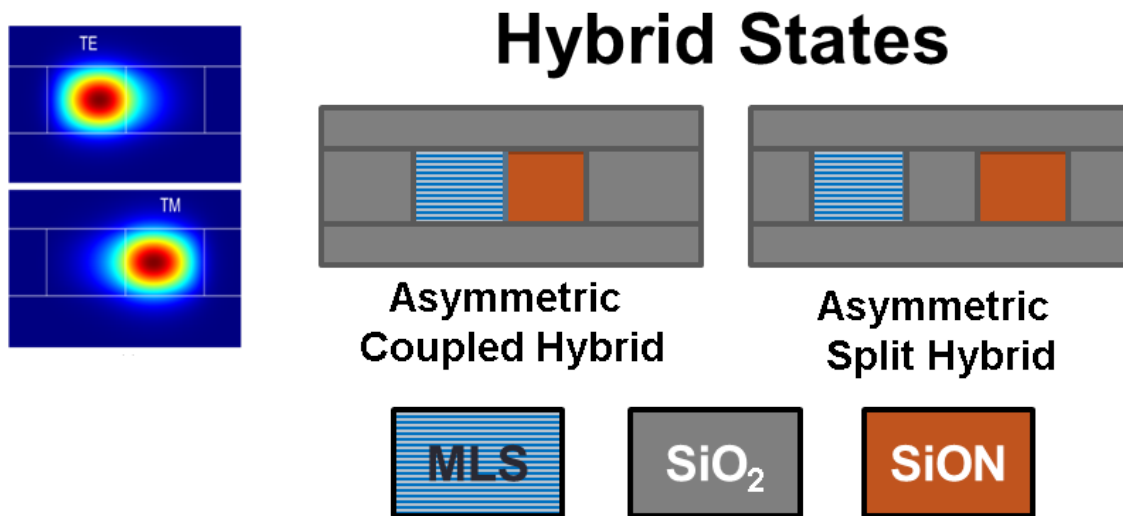
Figure 6.7: Hybrid states showing waveguide material configuration for transitions used in devices, along with a mode simulation for one of the hybrid states

patterned by electron-beam lithography using a Leica EBPG5000+ writer. The MLS is dry-etched to form trenches for the SiON regions. The trenches are refilled with SiON by PECVD. S1805 photoresist is spun onto the sample to planarize the surface, and a etch-back process flattens the top surface of the sample. The sample is coated with ZEP 520-A and patterned with electron-beam lithography a second time to define trenches for the SiO_2 regions, and these areas are dry-etched Lastly, SiO_2 is deposited by PECVD to refill the trenches and to form a top cladding. The full fabrication process is detailed in Appendix A, and the dry-etch and PECVD recipe parameters are listed in Appendix B. Figure 6.8 summarizes this fabrication process.

6.6   Device Design and Characterization

These fundamental and hybrid states can be combined in various ways to create multiple polarization-selective devices. The simulation, design, and measurement results for these devices are discussed
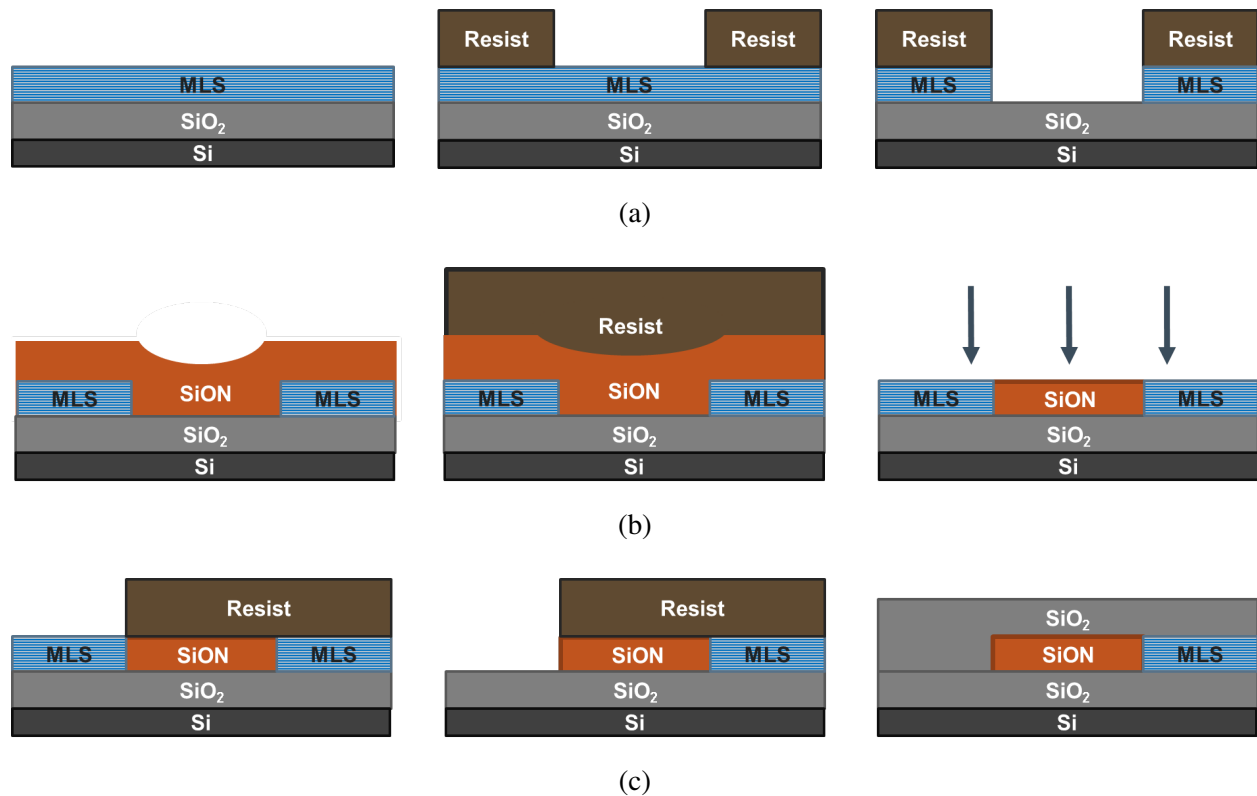
Figure 6.8: Summarization of the fabrication process for the spatially-mapped anisotropic photonics platform, showing (a) the deposition, patterning, and etching of the MLS material, (b) the refill, planarization, and etchback of the SiON material, and (c) the patterning, etching, and deposition for the SiO$_2$ cladding material.

in this section.

6.6.1 Polarization Beam Splitter

The first device realized is a polarization beam splitter (PBS). By starting with a bipolarized waveguide and transitioning first into the asymmetric coupled hybrid state and finally into the asymmetric split hybrid state, a device is created where TM-polarized light remains in the SiON core and TE-polarized light is pulled away from the SiON core and into the MLS core, as shown

in Fig. 6.9. Top-view Lumerical MODE Solutions™ eigenmode expansion (EME) simulation results for TE- and TM-polarized input light are also shown in Fig. 6.9. These simulations show an extinction ration (ER) between the polarizations greater than 12.7 dB and with an insertion loss less than 0.26 dB across a nearly 480 nm wavelength span, as detailed in Table 6.2.
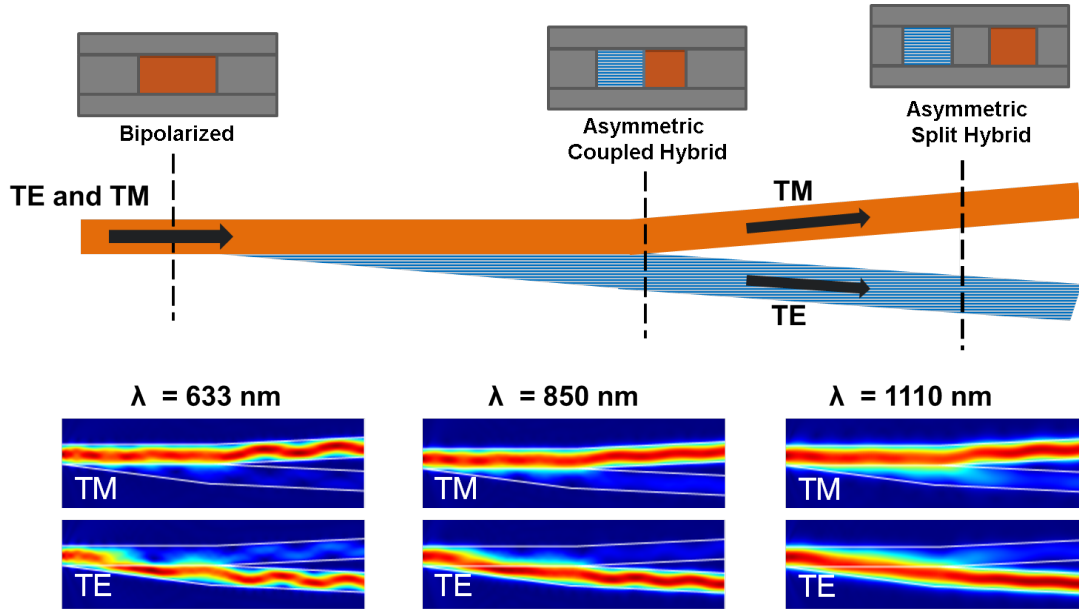
Figure 6.9: Device design and top view PBS simulations showing broadband operation.

Table 6.2: PBS ER and Loss Simulations

Wavelength (nm)	Insertion Loss (dB)		Extinction Ratio (dB)	
	TM	TE	TM	TE
633	0.03	0.26	21.47	12.7
850	0.13	0.04	17.0	19.3
1110	0.20	0.10	13.8	16.4

The device is designed to start with a single input, which is then split into a reference arm and a device arm through a 50:50 Y-junction splitter. The reference arm continues straight to the end of the die. The device arm contains the PBS, which splits into a TM arm and a TE arm. The TM

70

arm keeps the SiON core of the input waveguide. The TE arm is formed by introducing a wedge of MLS material that pulls the TE mode away from the SiON core. This region where the MLS and SiON are adjacent is long enough to sufficiently separate the polarizations, and then a wedge of SiO_2 is introduced to separate the cores. Finally, to minimize propogation losses of the TE mode in the MLS, the waveguide of the TE arm is switched back to a SiON core and SiO_2 cladding. At the end of the die there are three output ports, one for each of the TE, TM, and reference arms, and each arm is routed to its respective output port. Figure 6.10 shows this PBS device layout, along with extra detail of the polarization-splitting region.
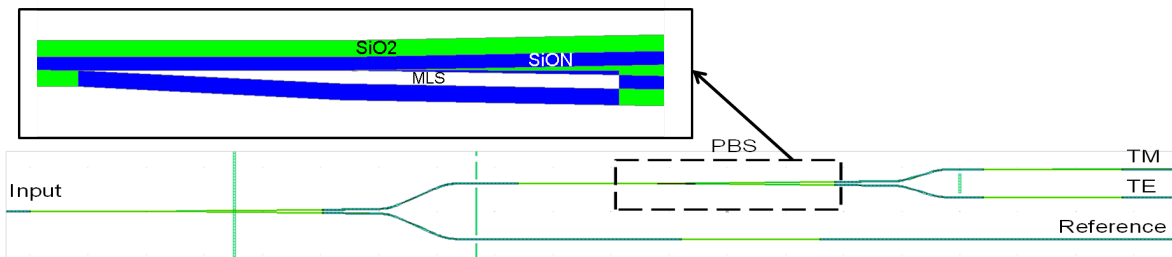
Figure 6.10: PBS device layout. Insert: detail of polarization-splitting region.

The PBS devices are measured with free-space laser sources of multiple wavelengths: $\lambda = 633$, 780, 855, 976, and 1117 nm. The light is passed through a Glan-Taylor polarizer, and then coupled into the waveguide using a 20X objective lens. The input side of the sample is partially diced and cleaved to create facets. The output contains a partially etched top facet to provide consistent out-coupling, important for relative intensity measurements. The light at the output facets is imaged using a top-view camera that imaged all three of the output ports per device simultaneously. A neutral density (ND) filter is used to reduce the amount of light, and camera settings are adjusted to further reduce the brightness and avoid saturating the camera pixels. Figure 6.11a shows this top-view look at the device region itself, along with images of device operation with TE- and TM-input light. Figure 6.11b shows a detailed view of the ports during measurement with both
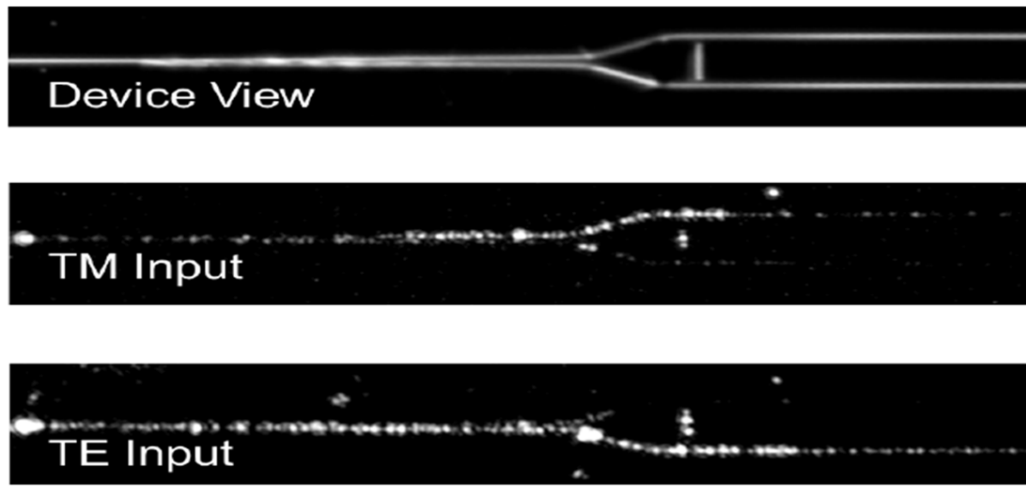
(a)

(b)

Figure 6.11: Images from measuring a PBS: (a) Top-view look at fabricated device, and images while measuring with TM- and TE-polarized input light. (b) Top-view look at (saturated) output ports while measuring with TM- and TE-polarized input light.

TM and TE light. The light shown in the ports is saturated solely for demonstration purposes.

The extinction ratio (ER) and device insertion loss are measured measured for each wavelength by comparing the relative intensity of light in the output ports. The ER is calculated by comparing the intensities in the TE and TM output ports, and the insertion loss is calculated by comparing the intensity of light in each device arm to the intensity of the light in the reference arm. Figure 6.12 shows the ER and loss results for each wavelength. Across a wavelength span of 337 nm (from $\lambda = 780$ to 1117 nm) which represents a fractional bandwidth of 0.52 octaves, a minimum ER of 16
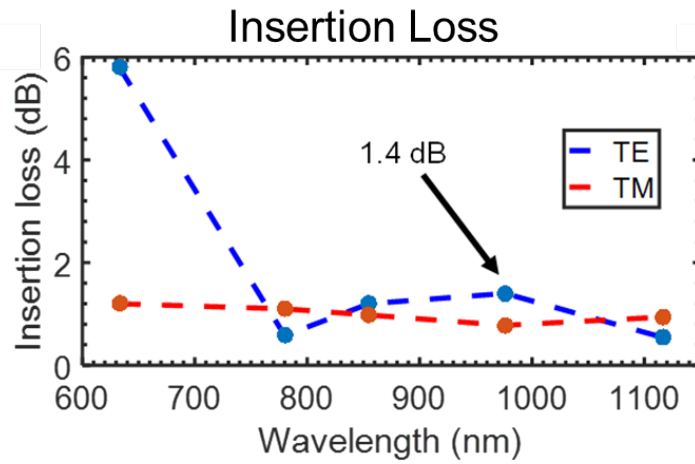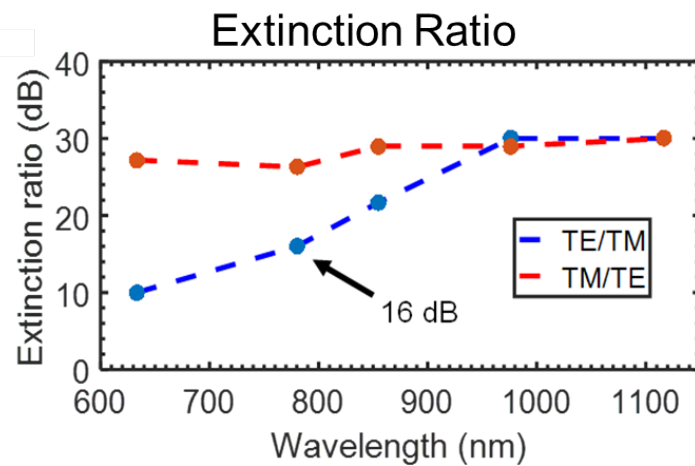
Figure 6.12: PBS experimental results, (a) insertion loss and (b) extinction ratio)

dB and maximum device loss of 1.4 dB is achieved. The ER improves at longer wavelengths. This represents the broadest bandwidth for an integrated PBS, and has a 6 dB minimum ER improvement over the current best technology [56].
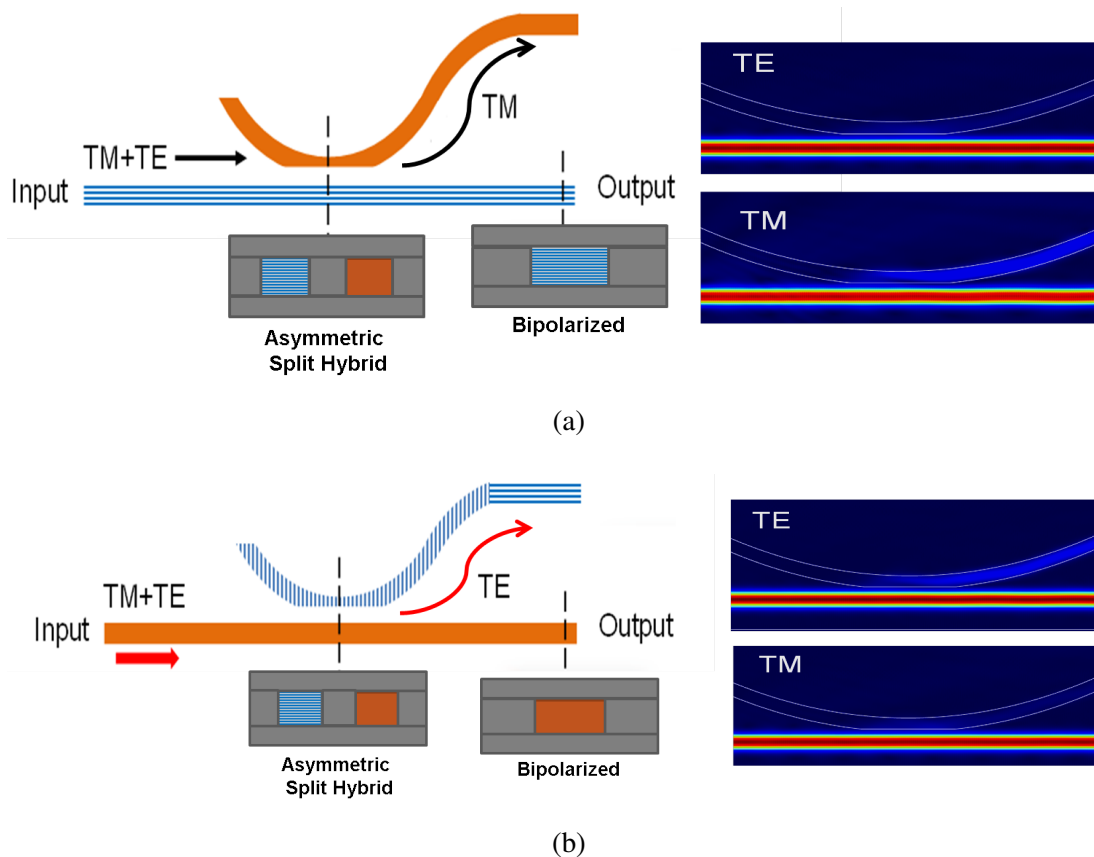
Figure 6.13: PSBT design and top view simulation for (a) TM-selective and (b) TE-selective devices, with top-view simulations of the coupling regions.

6.6.2   *Polarization-Selective Beam Taps*

The fundamental and hybrid states from Figs. 6.6 and 6.7 can also be combined to create other devices. One such device is the polarization-selective beam taps (PSBT) [114]. A diagram of the PSBT is shown in Fig. 6.13. As shown, only one polarization of light is coupled into the tapped-off arm, and the orthogonal polarization continues straight. This device could be useful if a small amount of a single polarization needed to be routed elsewhere on a chip.

Figure 6.13 also shows Lumerical MODE Solutions™ EME simulation results for the coupling
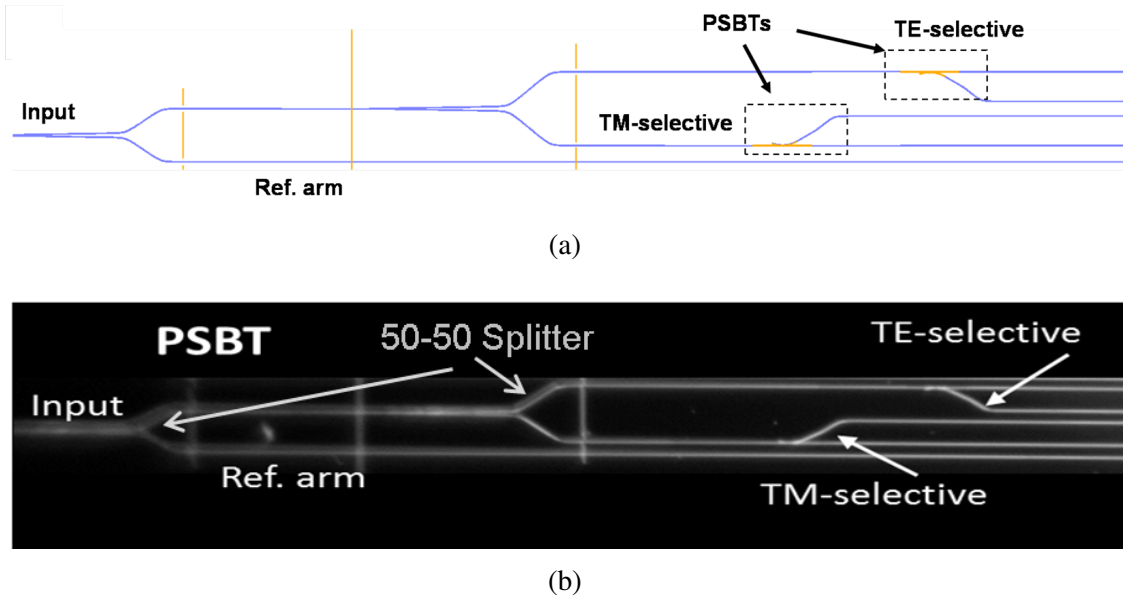
Figure 6.14: (a) Diagram of PSBT design (b) Top-view image of fabricated device

region of the PSBT device. For TM-selective devices, TM-polarized light is coupled into the SiON core, and TE-polarized light remains in the straight waveguide. For TE-selective devices, TE-polarized light is coupled into the MLS core and TM-polarized light is unaffected.

Figure 6.14 shows a diagram of the final PSBT design, and an image of the fabricated device. Similar to the PBS design, the PSBT splits between a reference arm and a device arm. The device arm contains a second 50:50 splitter and splits into TE and TM arms. Each arm then has two output ports, one from the bus waveguide and one from the tapped-off waveguide.

The PSBT devices are measured in a similar way as the PBS, using wavelengths $\lambda = 780$ and 855 nm. The results for the PSBTs are interpreted in terms of the polarization-dependent coupling ratio (PDCR). Table 6.3 summarizes the coupling coefficient and PDCR results for both wavelengths.

The PDCR is the ratio of the coupling coefficient of power coupled into the tap-off port for

Table 6.3: Experimental PSBT performance

Wavelength (nm)	Device type	PDCR, dB (±1)
780	TE-selective	6.5
	TM-selective	14
855	TE-selective	5.5
	TM-selective	9.4

one polarization state divided by the coupling coefficient into the tap-off port for the orthogonal polarization. Although the TM-selective devices have better performance, these results confirm polarization selectivity for both TE- and TM-selective devices.

6.6.3   Polarization-Selective Microring Resonators

A third type of device that can be made on this platform is the polarization-selective mircroring resonator (PSMR) [114]. The PSMR design is similar to the PSBT, except the loop is closed to form a ring rather than continuing as a waveguide. As before, only one polarization is coupled into the microring, and the ring is essentially invisible to the orthogonal polarization. The PSMR could be useful if orthogonal polarizations of light needed to be filtered separately. Instead of first passing through a PBS and then entering a standard microring resonator, a PSMR could be used, thus decreasing the footprint size of the device, and removing any extra loss introduced by the PBS. A diagram of the PSMR is shown in Fig. 6.15. As shown, only one polarization of light is coupled into the microring, and the orthogonal polarization continues straight.

The Lumerical MODE Solutions™ EME simulation results of the coupling regions of the PSBTs in Fig. 6.15 are the same as those for the PSMR devices. As with the PSBTs, for TM-selective devices, TM-polarized light is coupled into the SiON core, and TE-polarized light remains in the straight waveguide. For TE-selective devices, TE-polarized light is coupled into the MLS core and
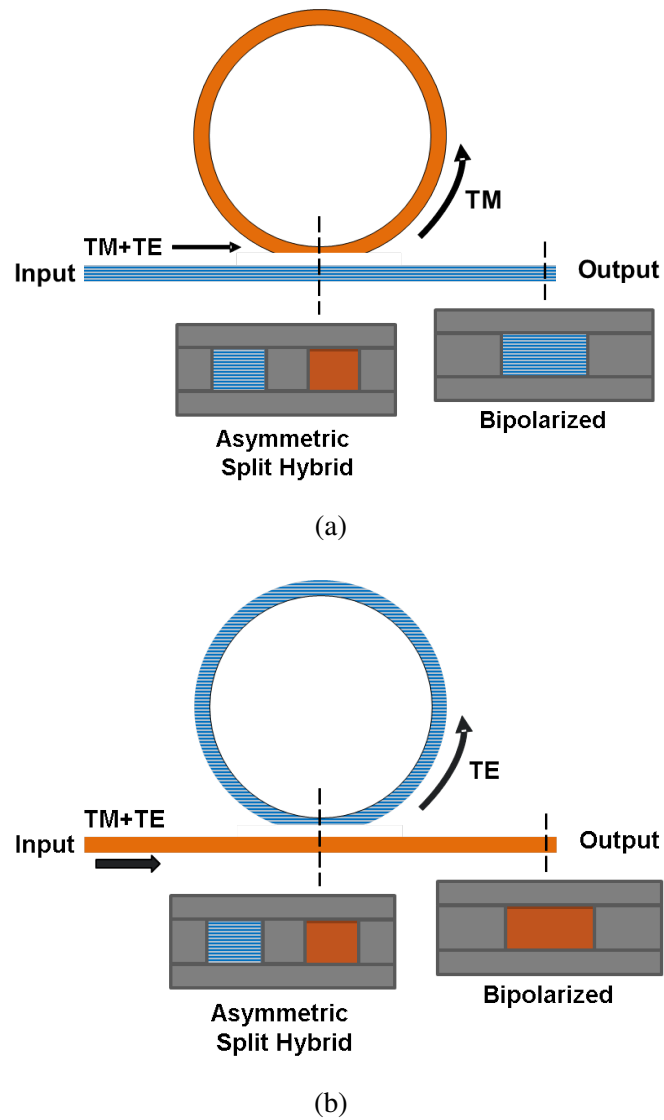
Figure 6.15: PSMR design and top view simulation for (a) TM-selective and (b) TE-selective devices.

TM-polarized light is unaffected.

Figure 6.16 shows a diagram of the final PSMR design, and an image of the fabricated device. Similar to the PSBT design, the PSMR splits between a reference arm and a device arm. The device arm contains a second 50:50 splitter and splits into TE and TM arms.
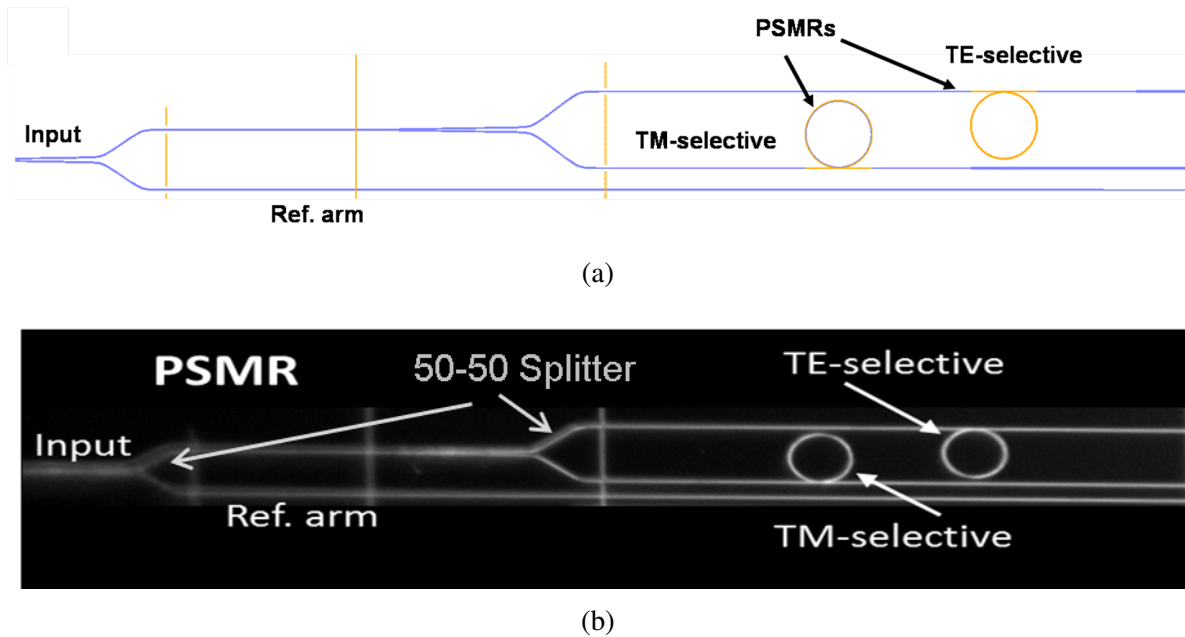
Figure 6.16: (a) Diagram of PSMR design (b) Top-view image of fabricated device

The PSMR devices are measured with a vertical-cavity surface-emitting laser (VCSEL) centered at $\lambda = 855$ nm. As with the other devices, the input light is polarized with a Glan-Taylor polarizer and lens coupled into the input facet of the die. The VCSEL is thermally tuned from room temperature to 50 °C, which corresponds to approximately a sweep in wavelength of 1 nm. The intensity in the output ports is recorded throughout the sweep, and plotted versus wavelength in a transmission plot. These transmission plots are shown in Fig. 6.17. The results are interpreted in terms of quality factor and ER. The transmission plot for the TM-selective device shows resonances for TM-polarized light, with an extinction ratio (ER) of 11 dB. There are no visible resonances for TE-polarized light, resulting in a large PDCR for the TM-selective device. The peak loaded quality factor for the TM-selective device is approximately 47,000. The transmission plot for the TE-selective device shows resonances for both TE- and TM-polarized input light, but the resonances for the TE-polarized light are much more pronounced. The difference between the ERs of the

resonances (Δ ER = 8.9 dB) is large enough to confirm a distinct selectivity towards TE-light. These results are consistent with the reduced PDCR measured for the TE-selective PSBT device.

6.7   Conclusions

In conclusion, the novel spatially-mapped anisotropic photonics platform was developed as a solution to the lack of methods to achieve broadband polarization diversity in silicon photonics. An explanation of the need and applications for broadband polarization diversity is given, along with a review of the current-best technology in use for meeting this need. Challenges and disadvantages with current approaches are discussed, prompting the development of a new platform. The spatially-mapped anisotropic photonics platform avoids some of these challenges faced by these other implementations. The platform makes use of a MLS of layers of non-birefringent materials to form a birefringent material. When paired with an isotropic material with a carefully-tuned refractive index, polarization-selective waveguides can be created.

By mapping this anisotropic material across a chip to form specific hybrid states, polarization-selective devices can also be formed, including PBS, PSBT, and PSMR. The fabrication, design, simulation, and characterization processes of these three devices are presented. The high-performing PBS exhibits high ER and low insertion loss across a record-breaking 337 nm bandwidth. The PSBTs show strong polarization selectivity as given by the high PDCR. The PSMRs also show strong polarization selectivity, as shown by the high extinction ratio between the resonances of the polarizations.
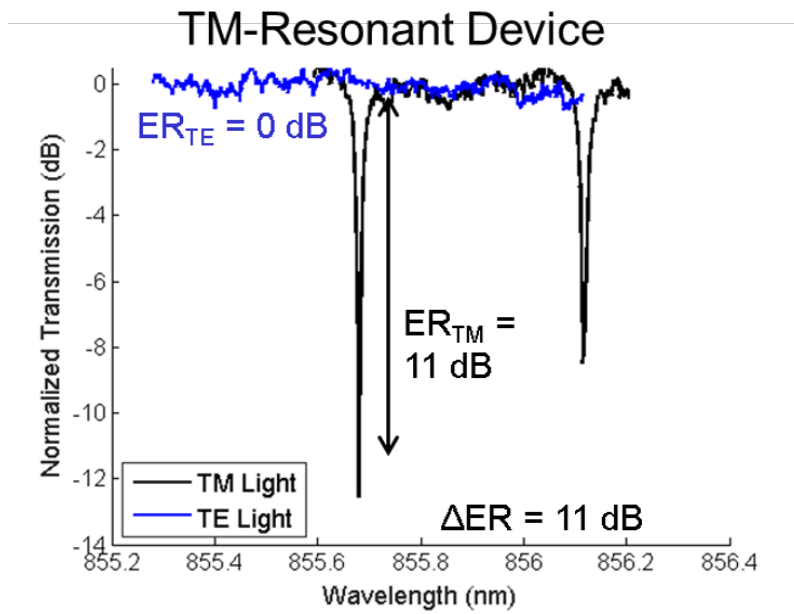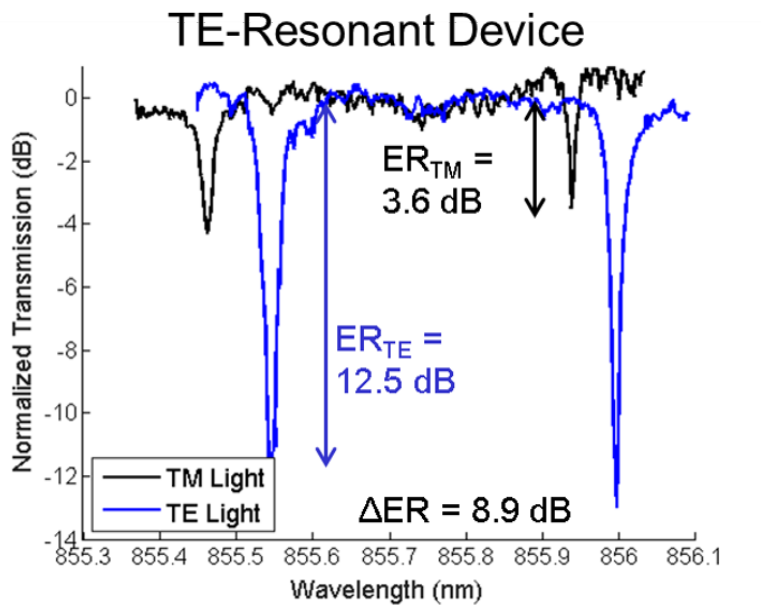
Figure 6.17: Transmission plots for (a) TM-selective, and (b) TE-selective PSMR.

CHAPTER 7: CONCLUSION AND FUTURE DIRECTIONS

This dissertation has discussed work proposed to address two limitations of the SOI platform: thin-film PPLN waveguides for harmonic generation to compensate for silicon's zero second-order nonlinearity, and the spatially-mapped anisotropic photonics platform to compensate for the lack of methods to achieve broadband polarization diversity with silicon waveguides. The results achieved on each of these platforms is summarized below.

7.1   Thin-Film PPLN for Nonlinear Frequency Conversion

Due to silicon's centrosymmetric crystal structure, it has no $\chi^{(2)}$ nonlinearity. Thus, other solutions are required for second-order nonlinear frequency conversion processes such as SHG and SFG. This work looked at the heterogeneous integration of thin-film lithium niobate with silicon. Lithium niobate has strong second-order nonlinearity leading to efficient frequency conversion processes. When implemented as the thin-film PPLN on silicon platform, this efficiency is enhanced by the sub-micron, high-contrast waveguides with tightly-confined optical modes possible with the platform.

7.1.1   High-Efficiency Second Harmonic Generation

Thin-film PPLN on silicon waveguides for SHG have shown a record-breaking conversion efficiency of 4,600 $\%W^{-1}cm^{-2}$. These waveguides are formed by directly etching the LN, and are poled using an actively-monitored iterative poling process to maximize the effectiveness of the poling procedure, to thus maximize the generation of the SH. Additional measurements with a pulsed source have shown small amounts of THG and FHG, suggesting the possibility of fabricating

devices to maximize these high-order frequency conversion processes.

7.1.2   Cascaded Harmonic Generation

Building on these high-efficiency SHG PPLN waveugides, cascaded thin-film PPLN on Si devices have been presented and demonstrate efficient SHG and SFG processes, generating the second-, third-, and fourth-order harmonics of 1550 nm. Cascaded SHG and SFG processes generate the TH, and two cascaded SHG processes generate the FH. Pulsed-source measurements indicate strong conversion efficiencies, though the spectrally-rich bandwidth of the pulsed source makes quantifying the conversion efficiency values difficult.

7.1.3   Modeling Pulsed-Input Harmonic Generation

Due to difficulties in quantifying the conversion efficiencies of PPLN segments when measured with a pulsed source, a numerical model has been developed that simulates the harmonic-generation that occurs when pumped with a pulsed source. The model solves the nonlinear Schrödinger equation for coupled modes with second-order nonlinearity for SHG and SFG, and allows the conversion efficiencies of the PPLN segments to be extracted. The simulated conversion efficiencies are 28.8 ± 8.5%/W for the SFG conversion process for generating the TH, and 10.0 ± 1.2%/W for the SHG conversion process for generating the FH.

7.2   Polarization Diversity

SOI waveguides are sensitive to polarization due to the large modal birefringence in the ultra-compact waveguides. As an alternative to attempts to decrease this sensitivity, the polarizations

can instead be split apart and processed separately, using PBS or PSRs. Although several implementations have been demonstrated by taking advantage of the modal birefringence of the material, the methods are not particularly broadband. Thus, a new platform is developed to overcome this challenge by instead manipulating the anisotropy of the material itself.

7.2.1 *Spatially-Mapped Anisotropic Photonics Platform*

The Spatially-Mapped Anisotropic platform has been presented as a new platform for achieving robust, broadband polarization diversity. The platform consists of layering thin alternating layers of non-birefringent materials to form a birefringent MLS, and mapping this anisotropy across a chip. An additional isotropic material with a carefully-tuned refractive index completes the polarization-selectivity. The fabrication methods of this platform have been discussed, as well as devices realized with this platform.

Polarization beam splitters have been demonstrated and shown to have low loss and high extinction ratios over a record-breaking bandwidth. Polarization-selective devices, including polarization beam taps and microring resonators, have also been demonstrated and show strong polarization selectivity.

7.3   Future Directions

Much research in the areas of nonlinear frequency conversion and polarization diversity has been perform and discussed in this dissertation. However, there is room for even further research in these areas. This section discusses these avenues for further research. Some amount of initial theory, design, and simulation work has been done in each of these areas, and this work is also presented.

7.3.1 Nonlinear Frequency Conversion

In this work, SHG and SFG through thin-film PPLN-on-Si have been used to demonstrate the generation of higher-order frequencies. However, these PPLN segments could also be used for DFG for the generation of longer wavelengths.

Looking at further nonlinear applications, third-order nonlinear processes can also be integrated. The integration of $\chi^{(2)}$-$\chi^{(3)}$ nonlinearities is another research area of interest for thin-film LN.

These two areas of research are further discussed in the following sections.

Difference Frequency Generation with Thin-film PPLN

Mid-infrared (mid-IR) (2-5 μm) light sources are useful for a variety of applications including chemical sensing, surgery, medical diagnostics, and infrared countermeasures. Recently, mid-IR laser technologies, including bulk solid-state [115], fibers [116], waveguides [117, 118], and quantum cascade lasers (QCLs) [119] have significantly improved. Fiber and waveguide devices have the benefit of containing less free-space optical components, which alleviates misalignment and improves reliability.

Mid-IR nonlinear frequency conversion, another viable route to mid-IR light generation, could be realized using QPM methods, such as PPLN. Previously, DFG was proposed for zinc selenide (ZnSe) MSM waveguides, however, implementing DFG with PPLN-on-Si allows the phase-matching condition to be met through the likely more efficient and easier to implement periodic poling method as opposed to MSM-QPM. Currently QCL lasers generate these desired mid-IR wavelengths, but an implementation with PPLN on Si has the potential to be easier to implement.

In order to generate light in the mid-IR (3.5μm), two input pump signals with wavelengths of 1.6

and 1.1 μm can be used. This is shown in Fig. 7.1, where the output follows from Fig. 2.1.
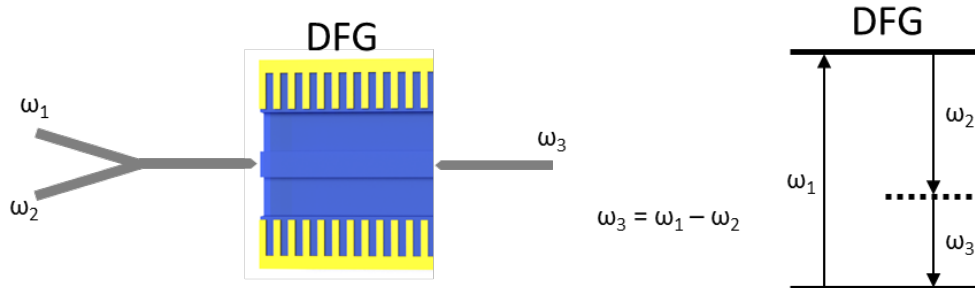
Figure 7.1: PPLN waveguide schematic for DFG.

With such a large difference in mode size between these wavelengths, designing a waveguide that will support all three modes while remaining low-loss for each will be challenging. Waveguides will not be single-mode across the wavelength range, so the presence of higher-order modes will add complexity to the phase-matching of the nonlinear conversion process.

The fabrication process will be similar to that described for the SHG and SFG PPLN-on-Si implementations in Chapters 3 and 4, including patterning with electron-beam lithography, depositing gold electrodes, and etching lithium niobate. The periodicity of the electrodes for QPM will be calculated using (2.10).

Challenges will arise in requiring a deeper LN etch to confine the lower- frequency modes. A deeper LN etch will produce additional etch-material redeposition in the etched-trench areas, which can affect the waveguide sidewall angle and roughness, as well as overall waveguide loss. An improved etching and cleaning process will need to be developed to produce such a device.

Third-order nonlinear processes can also benefit from being implemented with integrated approaches. Although silicon has a large $\chi^{(3)}$, two-photon absorption and free-carrier absorption occur at high intensity, and these high intensities are necessary for $\chi^{(3)}$ nonlinear processes [6, 17, 120]. Thus, heterogeneous integration with other, better-suited materials is again the solution. Chalcogenide glass has a large nonlinear refractive index, no free-carrier absorption, and a negligible two-photon absorption. These advantages, along with its ability to be easily deposited via thermal evaporation onto silicon wafers, makes chalcogenide a good material choice for integrated $\chi^{(3)}$ processes.

The integration of $\chi^{(2)}$ and $\chi^{(3)}$ nonlinearities on the same chip is advantageous for applications including frequency-stabilized optical comb generation based on supercontinuum generation (SCG) [121, 122, 123]. SCG is essentially the conversion of input pump light to light with a broad spectral bandwidth, and is realized by pumping a nonlinear device with pulsed-input light. Further heterogeneous integration of chalcogenide with the LN on silicon platform has been proposed and demonstrated for this $\chi^{(2)}$-$\chi^{(3)}$ integration [121]. This integration includes the thin-film LN platform introduced previously in this dissertation, with layers of Si_3N_4 and chalcogenide deposited on top to form rib-loaded waveguides and vertical mode tapers to adiabatically transition the mode from the chalcogenide and into the Si_3N_4 and LN. A schematic of this implementation, along with Lumerical MODE Solutions™ simulations of the adiabatic optical mode transition at various cross-sections of the vertical tapers, is shown in Fig. 7.2.

Measurements of these waveguides have shown reasonable loss values and have demonstrated wavelength conversion through four-wave mixing, showing promise for further research on this platform [121].
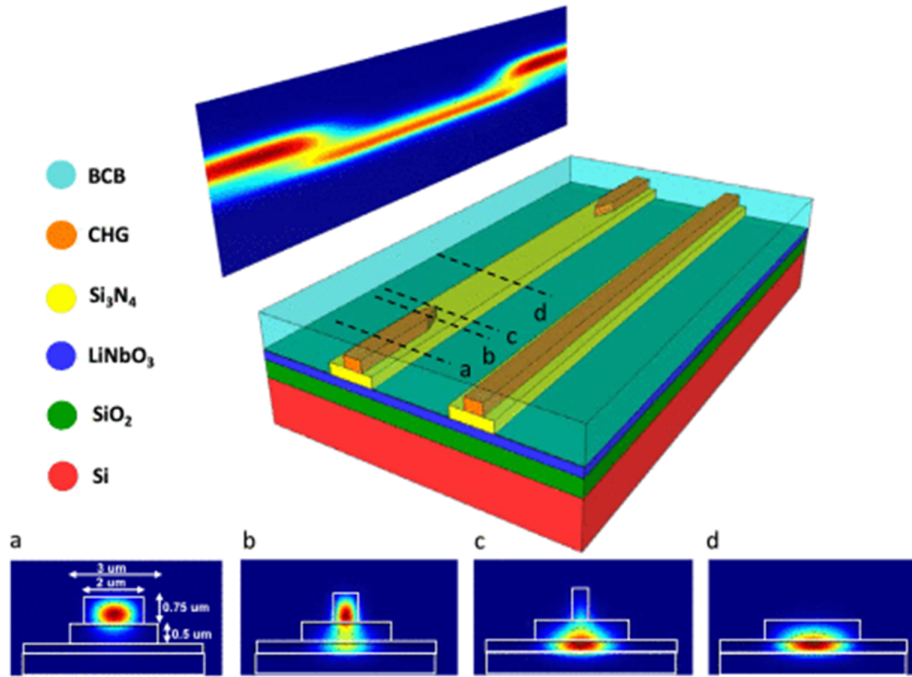
Figure 7.2: Schematic of LN and chalcogenide $\chi^{(2)}$-$\chi^{(3)}$ integration waveguides, with optical mode profile simulations at cross-sections of the vertical taper [121].

This further research includes development of a $\chi^{(2)}$-$\chi^{(3)}$ integration chip on which SHG and SCG are both demonstrated. This is towards the final goal of demonstrating frequency-stabilized optical comb generation based on octave-spanning SCG, with the SHG providing stabilization by f-to-$2f$ carrier-envelope offset (CEO) locking [121, 122, 123]. The SHG occurs in Si_3N_4 rib-loaded PPLN structures, and the SCG occurs in the chalcogenide waveguides. Lumerical MODE Solutions™ on structures similar to those pictured in 7.2 have been performed towards this end, and are detailed in [124, 125].

With the recent success of etching LN demonstrated with the devices in Chapters 3 and 4, this integration implementation has been redesigned to remove the Si_3N_4 and instead form an etched-LN ridge waveguide under the chalcogenide. This has the advantages of increasing the second-order

nonlinear mode overlap by having the mode confined completely in LN for the SHG PPLN segments, and simplifying the fabrication process by removing the Si_3N_4 deposition step. This waveguide structure has been optimized and simulated to show octave-spanning SCG. The electrode period for the SHG segments has also been calculated through additional mode simulations, and these waveguides and devices have been fabricated.

The PPLN and chalcogenide waveguides are placed separately to verify success of the SHG and SCG independently for this initial implementation, before eventually being combined into one device. CW measurements of the PPLN waveguides have shown SHG. Pulsed-input measurements of the SCG waveguides are ongoing. Measuring strong octave-spanning SCG in these devices will show additional promise towards reaching the goal of $\chi^{(2)}$-$\chi^{(3)}$ integration for frequency-stabilized optical comb generation.

7.3.2 *Polarization Diversity*

The spatially-mapped anisotropic photonics platform has demonstrated broadband, high-ER, low loss polarization beam splitters, and highly-selective polarization selective beam taps and microring resonators at near-infrared wavelengths. However, in order to demonstrate full polarization diversity, it must be capable of polarization rotation. Additionally, although high performance is observed for the current wavelength range, it is also important to have devices that can function at wavelengths in the telecommunication band ($\lambda = 1550$ nm) and where the silicon photonic platforms operate. Work is being done to address both of these current limitations.

Polarization Rotation

In order to achieve full polarization diversity on this integrated photonics platform, polarization rotation must be possible. As discussed previously, in order to rotate a polarization state, asymmetry is essential [72]. The current platform contains asymmetry in the refractive index, but physical, structural asymmetry is also necessary. Multiple polarization rotator (PR) designs have been explored [95, 126, 101, 127, 79] to find a device that best translates to this platform, and whose functionality is enhanced by the inherent refractive index asymmetry of the platform. Fig. 7.3 shows a diagram of the PR design [95] that currently shows the most promise for successfully being integrated with the current platform (the device shown was designed for Si waveguides, and so dimensions for actual fabricated waveguide will be much larger).
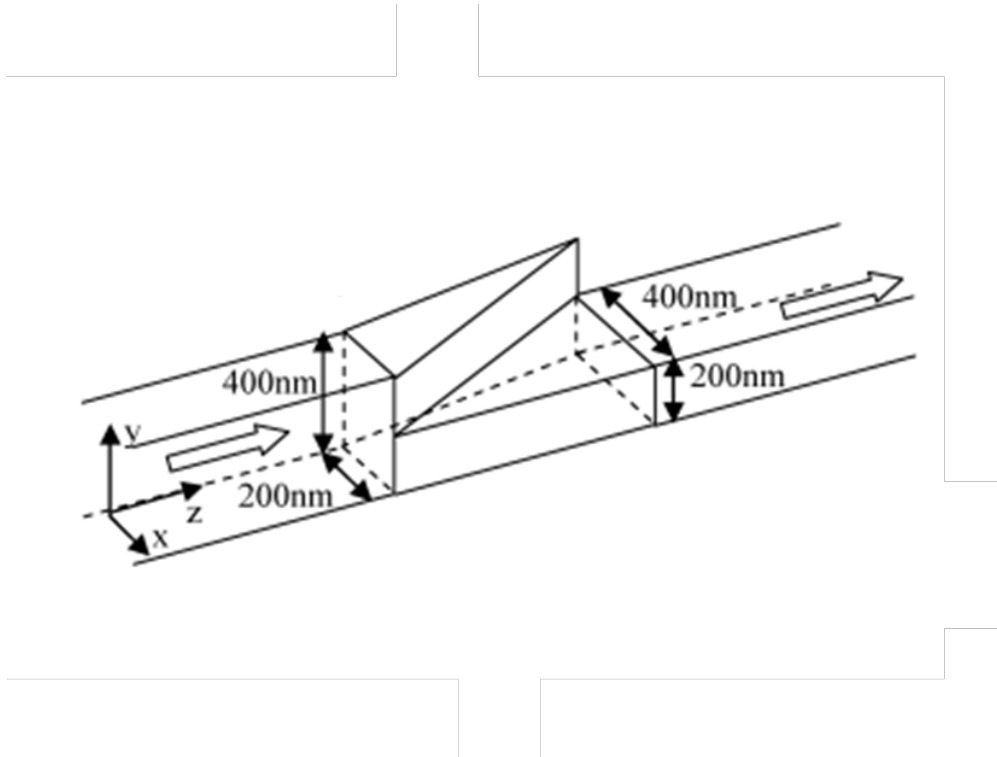
Figure 7.3: Polarization rotator design [95]

Lumerical MODE Solutions™ simulations have been performed to measure the amount of expected rotation of TE-polarized light to TM-polarized for a given device length. Figure 7.4 shows this transmission plot. However, due to the low refractive index contrast in the materials available on the platform, the device is required to be several hundred microns long in order to achieve full rotation to the orthogonal polarization.
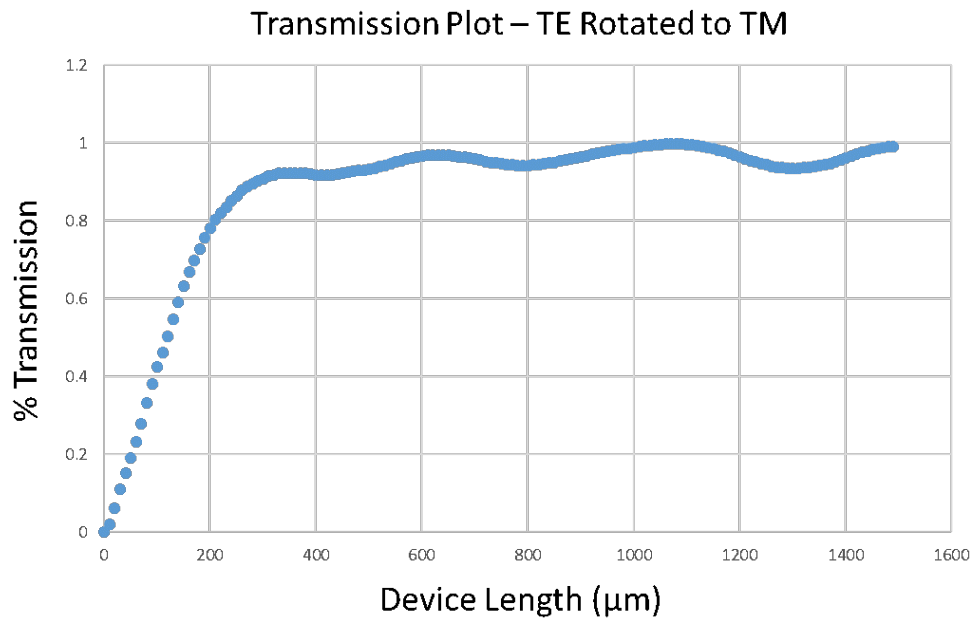
Figure 7.4: Transmission plot for rotating TE-polarized light to TM-polarized light

The PR will be fabricated through SiON PECVD depositions, aligned electron-beam lithography writes, and dry-etching. The vertical asymmetry of this PR design requires two dry-etch processes (and thus two aligned eletrcon-beam lithography patterning steps). Any slight misalignment between these two lithography steps could introduce loss or error to the device.

If initial results are not promising, the design choice will be reconsidered, potentially moving to a PSR that does not require vertical asymmetry, similar to that discussed in [102]. Future work will

include designing a better and more efficient PR that is enhanced by the anisotropy of the platform and is simpler to integrate with the other devices, while simultaneously choosing to fabricate the chosen design in order to test its functionality and optimize its output.

Operation at Telecommunication Band Wavelengths

While the spatially-mapped anisotropic photonics platform has shown high extinction ratios and low insertion losses for PBS and other devices over a broad bandwidth, operation at wavelengths in the telecommunication band is important. As discussed at the beginning of Chapter 6, the implementations that require broadband polarization diversity include, among others, polarization division multiplexing for communications applications. Additionally, this platform was presented as a solution for the lack of broadband polarization diversity methods for silicon photonics. As this platform currently operates below the transparency range of silicon, the platform as-is cannot be integrated with existing silicon photonic technologies that operate at these longer wavelengths.

Expanding this platform for operation at longer wavelengths and easier integrability with silicon photonics platforms requires a modification to the materials used to increase the effective indices. While the overall design concept will remain unchanged, the materials used for the MLS will likely be formed by alternating layers of Si_3N_4 and amorphous-Si, and the isotropic material will be silicon-rich Si_3N_4, increasing the effective indices and removing the platform dependence on SiO_2. Updating the materials will cause slight design modifications as the parameters for waveguide core size, taper lengths, coupling gaps, and interaction lengths will all change, but the overall design concept will remain as presented above.

The fabrication process will remain largely unchanged, apart from updating the etching and deposition recipes. The most time-intensive recipe change will be the planarization and etch-back process, as the etch rate of the isotropic refill material, in this case silicon-rich Si_3N_4, must match

the etch rate of the planarization photoresist material. Additionally, the PECVD depositions will require careful tuning of the deposition parameters to tune the refrative indices of the materials in order to achieve a birefringent MLS material, and an isotropic material whose refractive index is sandwiched between the TE- and TM-effective indices of the MLS.

Characterization of these devices will use input and output fiber coupling, with the output powers measured by photodetectors and power meters, instead of the top view camera used to characterize the previous implementation. The top view camera is not sensitive at these longer wavelengths, thus, the visual intensity measurement method cannot be scaled up for this implementation. Additionally, having exact values for the input and output powers, rather than relying on relative intensity measurements, will be beneficial in analyzing the results.

7.4   Conclusion

The areas of research discussed in this dissertation are presented as solutions to the current limitations of silicon photonics. These heterogeneous integration implementations combine the advantages and widespread usage of silicon photonics with the benefits of the materials best suited to overcome the challenges discussed, namely thin-film PPLN on silicon for second-order noninear frequency conversion and spatially-mapped anisotropic photonics for broadband polarization diversity. These devices realized on these platforms include high-efficiency SHG PPLN waveguides, cascaded PPLN waveguides - complete with numerical model for quantifying conversion efficiencies for devices measured with a pulsed source - for higher-harmonic generation to the third- and fourth-order harmonics, and broadband PBS and polarization-selective devices. These research topics further progress the field of silicon photonics, and as such also enhance the technology that makes up the field of integrated photonics.

APPENDIX A: FABRICATION PROCESSES

This section details the fabrication methods of the samples discussed in the main body of work. The fabrication steps are given to allow for easier future replication.

A.1 Periodically-Poled Lithium Niobate on Silicon

This section details the steps used to fabricate the lithium niobate harmonic generation devices.

1. Coat an *X*-cut 300 nm lithium niobate (LN) on silicon wafer with a thick layer of Shipley S1813 photoresist to protect surface while cleaving.

2. Cleave wafer to desired die size.

3. Thoroughly rinse the die with acetone, IPA, water and again IPA, and dry with nitrogen.

4. Coat sample with ZEP e-beam lithography resist in two steps, each spun at 1500 rpm.

5. Pattern electrodes and alignment markers with e-beam lithography.

6. Develop die in ortho-xylene - time determined by feature size and dose - and rinse with IPA.

7. Deposit layer of 10 nm chrome and 100 nm gold using e-beam evaporation, and perform liftoff in N-Methyl-2-pyrrolidone heated to 120 °C.

8. Perform alignment e-beam lithography to pattern the waveguides, with same resist preparation and development as before.

9. Dry-etch 100 nm of LN in argon plasma with RIE using recipe B.1.1.

10. Clean with soft oxygen plasma and dilute hydrofluoric acid (HF) solution (1:100 49% HF:H_2O)

11. Coat the sample with a thick layer of Shipley S1813 photoresist to protect the surface.

12. Dice both ends to form facets, and polish to a smooth finish.

A.2 Spatially-Mapped Anisotropic Photonic Polarization-Diversity

This section details the steps used to fabricate the PBS, PSBT, and PSMR devices.

1. Coat an oxidized silicon wafer with a thick layer of photoresist to protect the surface.

2. Cleave wafer into desired die size.

3. Thoroughly rinse the die with acetone, IPA, water and again IPA, and dry with nitrogen.

4. Coat die with photoresist, and pattern alignment markers with photolithography. Develop with Toluene.

5. Deposit 10 nm chrome and 70 nm gold with e-beam evaporation to form alignment markers.

6. Deposit SiO_2/Si_3N_4 mulilayer stack with PECVD, using recipe B.2.1.

7. Pattern trenches to be filled with SiON with e-beam lithography, coating the sample with ZEP, and devolping in ortho-xylene.

8. Use RIE to etch completely through the multilayer stack, using B.1.2.

9. Clean resist using soft oxygen clean and acetone.

10. Refill the trenches with SiON using PECVD with recipe B.2.2.

11. Planarize the sample by spin-coating die with Shipley S1805 photoresist at 1000 rpm.

12. Use RIE to perform etch-back to the top of the multilayer stack using B.1.3.

13. Prepare sample for alignment e-beam lithography, and pattern areas for SiO_2 cladding.

14. Use RIE to again completely etch through the multilayer stack, using recipe B.1.2

15. Clean die and deposit 1 μm SiO$_2$ cladding with PECVD, using recipe B.2.3.

16. Partially dice and cleave both ends of die to form waveguide facets.

APPENDIX B: FABRICATION RECIPES

B.1 Apex SLR Etcher Recipes

This section details the process parameters for etch recipes with the Apex SLR Etcher.

B.1.1 Lithium Niobate Etch

This is a recipe for etching lithium niobate with the Apex SLR Etcher.

- Bias power: 50 W

- ICP power: 300 W

- Process pressure: 10 mT

- Argon flow: 20 sccm

- Etch rate: 30 nm/min

B.1.2 Multilayer Stack Etch

This is a recipe for etching the Si_3N_4/SiO_2 multilayer stack with the Apex SLR Etcher.

- Bias power: 15 W

- ICP power: 750 W

- Process pressure: 6 mT

- CHF_3 flow: 40 sccm

- SF_6 flow: 10 sccm

B.1.3   SiON Etch-Back

This is a recipe for etching SiON and S1805 resist at the same rate with the Apex SLR Etcher. This planarizes the surface after SiON refill.

- Bias power: 20 W

- ICP power: 750 W

- Process pressure: 5 mT

- CHF_3 flow: 25 sccm

- Etch rate: 230 nm/min

B.2   Vision 310 PECVD Recipes

This section details the process parameters for deposition recipes with the Vision 310 PECVD.

B.2.1   Multilayer Stack Deposition

This is a recipe for depositing the Si_3N_4/SiO_2 multilayer stack with the Vision 310 PECVD. The fill factors can be modified to adjust the refractive index. As given, this recipe produces a refractive index of 1.72 for TE at $\lambda = 633$ nm. Each layer pair is about 47 nm.

1. Si_3N_4 layer

   - Temperature: 300 °C

   - Silane (SiH_4) flow: 2000 sccm

- Ammonia (NH_3) flow: 40 sccm

- RF power: 30 W

- Pressure: 750 mT

- Run time: 2 minutes 14 seconds

2. SiO_2 layer

- Temperature: 300 °C

- Silane (SiH_4) flow: 400 sccm

- Nitrous oxide (N_2O) flow: 1420 sccm

- RF power: 20 W

- Pressure: 800 mT

- Run time: 50 seconds

B.2.2   SiON Refill

This is a recipe for depositing SiON with the Vision 310 PECVD. As given, this recipe produces a film with a refractive index of 1.68 for $\lambda = 633$ nm.

- Temperature: 300 °C

- Silane (SiH_4) flow: 1450 sccm

- Nitrous oxide (N_2O) flow: 115 sccm

- Ammonia (NH_3) flow: 100 sccm

- RF power: 30 W

- Pressure: 950 mT

- Deposition rate: 30 nm/min

B.2.3 SiO_2 Deposition

This is a recipe for depositing SiO_2 with the Vision 310 PECVD.

- Temperature: 300 °C

- Silane (SiH_4) flow: 400 sccm

- Nitrous oxide (N_2O) flow: 1420 sccm

- RF power: 20 W

- Pressure: 800 mT

- Deposition rate: 25 nm/min

LIST OF REFERENCES

[1] Richard A Soref. Silicon-based optoelectronics. *Proceedings of the IEEE*, 81(12):1687–1706, 1993.

[2] Stewart E Miller. Integrated optics: An introduction. *The Bell System Technical Journal*, 48(7):2059–2069, 1969.

[3] Ivan P Kaminow. Optical integrated circuits: A personal perspective. *Journal of Lightwave Technology*, 26(9):994–1004, 2008.

[4] Tom Baehr-Jones, Thierry Pinguet, Patrick Lo Guo-Qiang, Steven Danziger, Dennis Prather, and Michael Hochberg. Myths and rumours of silicon photonics. *Nature Photonics*, 6(4):206–208, 2012.

[5] B Jalali, S Yegnanarayanan, T Yoon, T Yoshimoto, I Rendina, and F Coppinger. Advances in silicon-on-insulator optoelectronics. *IEEE Journal of selected topics in Quantum Electronics*, 4(6):938–947, 1998.

[6] Bahram Jalali and Sasan Fathpour. Silicon photonics. *Journal of lightwave technology*, 24(12):4600–4615, 2006.

[7] RICHARDA Soref and BRIANR Bennett. Electrooptical effects in silicon. *IEEE journal of quantum electronics*, 23(1):123–129, 1987.

[8] JP Lorenzo and RA Soref. 1.3 μm electro-optic silicon switch. *Applied physics letters*, 51(1):6–8, 1987.

[9] Lionel Friedman, Richard A Soref, and Joseph P Lorenzo. Silicon double-injection electro-optic modulator with junction gate control. *Journal of applied physics*, 63(6):1831–1839, 1988.

[10] Graham T Reed, G Mashanovich, F Yand Gardes, and DJ Thomson. Silicon optical modulators. *Nature photonics*, 4(8):518, 2010.

[11] Ricardo Claps, Dimitri Dimitropoulos, Yan Han, and Bahram Jalali. Observation of raman emission in silicon waveguides at 1.54 μm. *Optics Express*, 10(22):1305–1313, 2002.

[12] Ozdal Boyraz and Bahram Jalali. Demonstration of a silicon raman laser. *Optics express*, 12(21):5269–5273, 2004.

[13] Haisheng Rong, Richard Jones, Ansheng Liu, Oded Cohen, Dani Hak, Alexander Fang, and Mario Paniccia. A continuous-wave raman silicon laser. *Nature*, 433(7027):725–728, 2005.

[14] R Claps, V Raghunathan, D Dimitropoulos, and B Jalali. Anti-stokes raman conversion in silicon waveguides. *Optics Express*, 11(22):2862–2872, 2003.

[15] V Raghunathan, R Claps, D Dimitropoulos, and B Jalali. Wavelength conversion in silicon using raman induced four-wave mixing. *Applied physics letters*, 85(1):34–36, 2004.

[16] Mark A Foster, Amy C Turner, Jay E Sharping, Bradley S Schmidt, Michal Lipson, and Alexander L Gaeta. Broad-band optical parametric gain on a silicon photonic chip. *Nature*, 441(7096):960–963, 2006.

[17] Sasan Fathpour. Emerging heterogeneous integrated photonic platforms on silicon. *Nanophotonics*, 4(1):143–164, 2015.

[18] Tao Chu, Nobuhide Fujioka, and Masashige Ishizaka. Compact, lower-power-consumption wavelength tunable laser fabricated with silicon photonic wire waveguide micro-ring resonators. *Optics express*, 17(16):14063–14068, 2009.

[19] Kazuya Ohira, Kentaro Kobayashi, Norio Iizuka, Haruhiko Yoshida, Mizunori Ezaki, Hiroshi Uemura, Akihiro Kojima, Kenro Nakamura, Hideto Furuyama, and Hideki Shibata. On-chip

optical interconnection by using integrated iii-v laser diode and photodetector with silicon waveguide. *Optics express*, 18(15):15440–15447, 2010.

[20] Shinsuke Tanaka, Seok-Hwan Jeong, Shigeaki Sekiguchi, Teruo Kurahashi, Yu Tanaka, and Ken Morito. High-output-power, single-wavelength silicon hybrid laser using precise flip-chip bonding technology. *Optics express*, 20(27):28057–28069, 2012.

[21] HZ Chen, J Paslaski, A Yariv, and H Morkoc. High-frequency modulation of algaas/gaas lasers grown on si substrate by molecular beam epitaxy. *Applied physics letters*, 52(8):605–606, 1988.

[22] Ashutosh Rao and Sasan Fathpour. Second-harmonic generation in integrated photonics on silicon. *physica status solidi (a)*, 215(4):1700684, 2018.

[23] Ashutosh Rao and Sasan Fathpour. Heterogeneous thin-film lithium niobate integrated photonics for electrooptics and nonlinear optics. *IEEE Journal of Selected Topics in Quantum Electronics*, 24(6):1–12, 2018.

[24] WHP Pernice, C Xiong, C Schuck, and HX Tang. Second harmonic generation in phase matched aluminum nitride waveguides and micro-ring resonators. *Applied Physics Letters*, 100(22):223501, 2012.

[25] Xiang Guo, Chang-Ling Zou, and Hong X Tang. Second-harmonic generation in aluminum nitride microrings with 2500%/w conversion efficiency. *Optica*, 3(10):1126–1131, 2016.

[26] RW Boyd and BR Masters. Nonlinear optics 3rd edn (new york: Academic). 2008.

[27] Ashutosh Rao, Marcin Malinowski, Amirmahdi Honardoost, Javed Rouf Talukder, Payam Rabiei, Peter Delfyett, and Sasan Fathpour. Second-harmonic generation in periodically-poled thin film lithium niobate wafer-bonded on silicon. *Optics express*, 24(26):29941–29947, 2016.

[28] Cheng Wang, Carsten Langrock, Alireza Marandi, Marc Jankowski, Mian Zhang, Boris Desiatov, Martin M Fejer, and Marko Lončar. Ultrahigh-efficiency wavelength conversion in nanophotonic periodically poled lithium niobate waveguides. *Optica*, 5(11):1438–1441, 2018.

[29] Richard Wolf, Ingo Breunig, Hans Zappe, and Karsten Buse. Cascaded second-order optical nonlinearities in on-chip micro rings. *Optics express*, 25(24):29927–29933, 2017.

[30] Daniel D Hickstein, David R Carlson, Abijith Kowligy, Matt Kirchner, Scott R Domingue, Nima Nader, Henry Timmers, Alex Lind, Gabriel G Ycas, Margaret M Murnane, et al. High-harmonic generation in periodically poled waveguides. *Optica*, 4(12):1538–1544, 2017.

[31] Alexander W Bruch, Xianwen Liu, Xiang Guo, Joshua B Surya, Zheng Gong, Liang Zhang, Junxi Wang, Jianchang Yan, and Hong X Tang. 17 000%/w second-harmonic conversion efficiency in single-crystalline aluminum nitride microresonators. *Applied Physics Letters*, 113(13):131102, 2018.

[32] David P Lake, Matthew Mitchell, Harishankar Jayakumar, Laís Fujii dos Santos, Davor Curic, and Paul E Barclay. Efficient telecom to visible wavelength conversion in doubly resonant gallium phosphide microdisks. *Applied Physics Letters*, 108(3):031109, 2016.

[33] Jacob S Levy, Mark A Foster, Alexander L Gaeta, and Michal Lipson. Harmonic generation in silicon nitride ring resonators. *Optics express*, 19(12):11415–11421, 2011.

[34] Adrien Billat, Davide Grassani, Martin HP Pfeiffer, Svyatoslav Kharitonov, Tobias J Kippenberg, and Camille-Sophie Brès. Large second harmonic generation enhancement in si 3 n 4 waveguides by all-optically induced quasi-phase-matching. *Nature communications*, 8(1):1–7, 2017.

[35] Joshua B Surya, Xiang Guo, Chang-Ling Zou, and Hong X Tang. Efficient third-harmonic generation in composite aluminum nitride/silicon nitride microrings. *Optica*, 5(2):103–108, 2018.

[36] Tobias J Kippenberg, Ronald Holzwarth, and Scott A Diddams. Microresonator-based optical frequency combs. *science*, 332(6029):555–559, 2011.

[37] Yoshitomo Okawachi, Kasturi Saha, Jacob S Levy, Y Henry Wen, Michal Lipson, and Alexander L Gaeta. Octave-spanning frequency comb generation in a silicon nitride chip. *Optics letters*, 36(17):3398–3400, 2011.

[38] Hojoong Jung, Chi Xiong, King Y Fong, Xufeng Zhang, and Hong X Tang. Optical frequency comb generation from aluminum nitride microring resonator. *Optics letters*, 38(15):2810–2813, 2013.

[39] Anshuman Singh, Qing Li, Shunfa Liu, Ying Yu, Xiyuan Lu, Christian Schneider, Sven Höfling, John Lawall, Varun Verma, Richard Mirin, et al. Quantum frequency conversion of a quantum dot single-photon source on a nanophotonic chip. *Optica*, 6(5):563–569, 2019.

[40] Sebastian Zaske, Andreas Lenhard, Christian A Keßler, Jan Kettler, Christian Hepp, Carsten Arend, Roland Albrecht, Wolfgang-Michael Schulz, Michael Jetter, Peter Michler, et al. Visible-to-telecom quantum frequency conversion of light from a single quantum emitter. *Physical review letters*, 109(14):147404, 2012.

[41] Takashi Isoshima and Kunio Tada. Local normal-mode analysis of second harmonic generation in a periodic waveguide. *IEEE journal of quantum electronics*, 33(2):164–175, 1997.

[42] Ashutosh Rao, Jeff Chiles, Saeed Khan, Seyfollah Toroghi, Marcin Malinowski, Guillermo Fernando Camacho-González, and Sasan Fathpour. Second-harmonic generation

in single-mode integrated waveguides based on mode-shape modulation. *Applied Physics Letters*, 110(11):111109, 2017.

[43] GD Miller, RG Batchko, WM Tulloch, DR Weise, MM Fejer, and RL Byer. 42%-efficient single-pass cw second-harmonic generation in periodically poled lithium niobate. *Optics letters*, 22(24):1834–1836, 1997.

[44] Krishnan R Parameswaran, Jonathan R Kurz, Rostislav V Roussev, and Martin M Fejer. Observation of 99% pump depletion in single-pass second-harmonic generation in a periodically poled lithium niobate waveguide. *Optics letters*, 27(1):43–45, 2002.

[45] V Pruneri, J Webjörn, P St J Russell, and DC Hanna. 532 nm pumped optical parametric oscillator in bulk periodically poled lithium niobate. *Applied physics letters*, 67(15):2126–2128, 1995.

[46] Lawrence E Myers and Walter R Bosenberg. Periodically poled lithium niobate and quasi-phase-matched optical parametric oscillators. *IEEE Journal of Quantum Electronics*, 33(10):1663–1672, 1997.

[47] Jonas Webjorn, Frederic Laurell, and Gunnar Arvidsson. Fabrication of periodically domain-inverted channel waveguides in lithium niobate for second harmonic generation. *Journal of lightwave technology*, 7(10):1597–1600, 1989.

[48] EJ Lim, Martin M Fejer, RL Byer, and WJ Kozlovsky. Blue light generation by frequency doubling in periodically poled lithium niobate channel waveguide. *Electronics letters*, 25(11):731–732, 1989.

[49] Lingyun Ye, Ju Wang, Hao Hu, Jinlong Yu, and Kaichen Song. All-optical broadcast and multicast technologies based on ppln waveguide. *Chinese Optics Letters*, 11(11):110604, 2013.

[50] Susumu Kuma, Yuki Miyamoto, Kousuke Tsutsumi, Noboru Sasao, and Satoshi Uetake. 4.8 μm difference-frequency generation using a waveguide-ppln crystal and its application to mid-infrared lamb-dip spectroscopy. *Optics Letters*, 38(15):2825–2828, 2013.

[51] RV Schmidt and IP Kaminow. Metal-diffused optical waveguides in linbo3. *Applied Physics Letters*, 25(8):458–460, 1974.

[52] Janet L Jackel, CE Rice, and JJ Veselka. Proton exchange for high-index waveguides in linbo3. *Applied Physics Letters*, 41(7):607–608, 1982.

[53] Sasan Fathpour. Heterogeneous nonlinear integrated photonics. *IEEE Journal of Quantum Electronics*, 54(6):1–16, 2018.

[54] Jintian Lin, Yingxin Xu, Zhiwei Fang, Min Wang, Jiangxin Song, Nengwen Wang, Lingling Qiao, Wei Fang, and Ya Cheng. Fabrication of high-q lithium niobate microresonators using femtosecond laser micromachining. *Scientific reports*, 5:8072, 2015.

[55] Ashutosh Rao, Kamal Abdelsalam, Tracy Sjaardema, Amirmahdi Honardoost, Guillermo F Camacho-Gonzalez, and Sasan Fathpour. Actively-monitored periodic-poling in thin-film lithium niobate photonic waveguides with ultrahigh nonlinear conversion efficiency of 4600% w- 1 cm- 2. *Optics express*, 27(18):25920–25930, 2019.

[56] Payam Rabiei, Jichi Ma, Saeed Khan, Jeff Chiles, and Sasan Fathpour. Heterogeneous lithium niobate photonics on silicon substrates. *Optics express*, 21(21):25573–25581, 2013.

[57] Payam Rabiei, Jichi Ma, Saeed Khan, Jeff Chiles, and Sasan Fathpour. Submicron optical waveguides and microring resonators fabricated by selective oxidation of tantalum. *Optics express*, 21(6):6967–6972, 2013.

[58] Jeff Chiles, Marcin Malinowski, Ashutosh Rao, Spencer Novak, Kathleen Richardson, and

Sasan Fathpour. Low-loss, submicron chalcogenide integrated photonics with chlorine plasma etching. *Applied Physics Letters*, 106(11):111110, 2015.

[59] Lin Chang, Yifei Li, Nicolas Volet, Leiran Wang, Jon Peters, and John E Bowers. Thin film wavelength converters for photonic integrated circuits. *Optica*, 3(5):531–535, 2016.

[60] M De Angelis, S De Nicola, A Finizio, G Pierattini, P Ferraro, Simonetta Grilli, and M Paturzo. Evaluation of the internal field in lithium niobate ferroelectric domains by an interferometric method. *Applied physics letters*, 85(14):2785–2787, 2004.

[61] Shijie Liu, Yuanlin Zheng, and Xianfeng Chen. Cascading second-order nonlinear processes in a lithium niobate-on-insulator microdisk. *Opt. Lett.*, 42(18):3626–3629, Sep 2017.

[62] Zheng Zheng, Andrew M Weiner, Krishnan R Parameswaran, Ming-Hsien Chou, and Martin M Fejer. Femtosecond second-harmonic generation in periodically poled lithium niobate waveguides with simultaneous strong pump depletion and group-velocity walk-off. *JOSA B*, 19(4):839–848, 2002.

[63] Andrew Weiner. *Ultrafast optics*, volume 72. John Wiley & Sons, 2011.

[64] Oleg V Sinkin, Ronald Holzlohner, John Zweck, and Curtis R Menyuk. Optimization of the split-step fourier method in modeling optical-fiber communications systems. *Journal of lightwave technology*, 21(1):61–68, 2003.

[65] Radhakrishnan Nagarajan, Jeffrey Rahn, Masaki Kato, Jacco Pleumeekers, Damien Lambert, Vikrant Lal, Huan-Shang Tsai, Alan Nilsson, Andrew Dentai, Matthias Kuntz, et al. 10 channel, 45.6 gb/s per channel, polarization-multiplexed dqpsk, inp receiver photonic integrated circuit. *Journal of lightwave technology*, 29(4):386–395, 2010.

[66] David Huang, Eric A Swanson, Charles P Lin, Joel S Schuman, William G Stinson, Warren

Chang, Michael R Hee, Thomas Flotte, Kenton Gregory, Carmen A Puliafito, et al. Optical coherence tomography. *science*, 254(5035):1178–1181, 1991.

[67] Zhao Wang, Hsiang-Chieh Lee, Diedrik Vermeulen, Long Chen, Torben Nielsen, Seo Yeon Park, Allan Ghaemi, Eric Swanson, Chris Doerr, and James Fujimoto. Silicon photonic integrated circuit swept-source optical coherence tomography receiver with dual polarization, dual balanced, in-phase and quadrature detection. *Biomedical optics express*, 6(7):2562–2574, 2015.

[68] Zhao Wang, Benjamin Potsaid, Long Chen, Chris Doerr, Hsiang-Chieh Lee, Torben Nielson, Vijaysekhar Jayaraman, Alex E Cable, Eric Swanson, and James G Fujimoto. Cubic meter volume optical coherence tomography. *Optica*, 3(12):1496–1503, 2016.

[69] J Scott Tyo, Dennis L Goldstein, David B Chenault, and Joseph A Shaw. Review of passive imaging polarimetry for remote sensing applications. *Applied optics*, 45(22):5453–5469, 2006.

[70] Songxin Tan and Ram M Narayanan. Design and performance of a multiwavelength airborne polarimetric lidar for vegetation remote sensing. *Applied Optics*, 43(11):2360–2368, 2004.

[71] Philippe Goloub, Maurice Herman, Hélène Chepfer, Jérôme Riédi, Gérard Brogniez, Pierre Couvert, and Geneviève Sèze. Cloud thermodynamical phase classification from the polder spaceborne instrument. *Journal of Geophysical Research: Atmospheres*, 105(D11):14747–14759, 2000.

[72] Daoxin Dai, Jared Bauters, and John E Bowers. Passive technologies for future large-scale photonic integrated circuits on silicon: polarization handling, light non-reciprocity and loss reduction. *Light: Science & Applications*, 1(3):e1–e1, 2012.

[73] Timo Pfau, Ralf Peveling, Jérôme Hauden, Nicolas Grossard, Henri Porte, Yaakov Achiam,

Sebastian Hoffmann, Selwan K Ibrahim, Olaf Adamczyk, Suhas Bhandare, et al. Coherent digital polarization diversity receiver for real-time polarization-multiplexed qpsk transmission at 2.8 gb/s. *IEEE Photonics Technology Letters*, 19(24):1988–1990, 2007.

[74] Diego Pérez-Galacho, Ruiyong Zhang, Alejandro Ortega-Moñux, Robert Halir, Carlos Alonso-Ramos, Patrick Runge, Klemens Janiak, Gan Zhou, Heinz-Gunter Bach, Andreas G Steffan, et al. Integrated polarization beam splitter for 100/400 ge polarization multiplexed coherent optical communications. *Journal of lightwave technology*, 32(3):361–368, 2014.

[75] Mengyuan Ye, Yu Yu, Jinghui Zou, Weili Yang, and Xinliang Zhang. On-chip multiplexing conversion between wavelength division multiplexing–polarization division multiplexing and wavelength division multiplexing–mode division multiplexing. *Optics letters*, 39(4):758–761, 2014.

[76] Eiichi Yamada, Shigeru Kanazawa, Akira Ohki, Kei Watanabe, Yusuke Nasu, Nobuhiro Kikuchi, Yasuo Shibata, Ryuzo Iga, and Hiroyuki Ishii. 112-gb/s inp dp-qpsk modulator integrated with a silica-plc polarization multiplexing circuit. In *National Fiber Optic Engineers Conference*, pages PDP5A–9. Optical Society of America, 2012.

[77] Daoxin Dai, Liu Liu, Lech Wosinski, and SAHS He. Design and fabrication of ultra-small overlapped awg demultiplexer based on/spl alpha/-si nanowire waveguides. *Electronics Letters*, 42(7):400–402, 2006.

[78] Tymon Barwicz, Michael R Watts, Miloš A Popović, Peter T Rakich, Luciano Socci, Franz X Kärtner, Erich P Ippen, and Henry I Smith. Polarization-transparent microphotonic devices in the strong confinement limit. *Nature Photonics*, 1(1):57–60, 2007.

[79] Hiroshi Fukuda, Koji Yamada, Tai Tsuchizawa, Toshifumi Watanabe, Hiroyuki Shinojima, and Sei-ichi Itabashi. Silicon photonic circuit with polarization diversity. *Optics express*, 16(7):4872–4880, 2008.

[80] Wim Bogaerts, Dirk Taillaert, Pieter Dumon, Dries Van Thourhout, Roel Baets, and Elroy Pluk. A polarization-diversity wavelength duplexer circuit in silicon-on-insulator photonic wires. *Optics express*, 15(4):1567–1578, 2007.

[81] D Pérez-Galacho, R Halir, A Ortega-Moñux, C Alonso-Ramos, R Zhang, P Runge, K Janiak, H-G Bach, AG Steffan, and Í Molina-Fernández. Integrated polarization beam splitter with relaxed fabrication tolerances. *Optics Express*, 21(12):14146–14151, 2013.

[82] Hiroshi Fukuda, Koji Yamada, Tai Tsuchizawa, Toshifumi Watanabe, Hiroyuki Shinojima, and Sei-ichi Itabashi. Ultrasmall polarization splitter based on silicon wire waveguides. *Optics Express*, 14(25):12401–12408, 2006.

[83] TK Liang and HK Tsang. Integrated polarization beam splitter in high index contrast silicon-on-insulator waveguides. *IEEE photonics technology letters*, 17(2):393–395, 2005.

[84] LM Augustin, R Hanfoug, JJGM Van der Tol, WJM De Laat, and MK Smit. A compact integrated polarization splitter/converter in ingaasp–inp. *IEEE Photonics Technology Letters*, 19(17):1286–1288, 2007.

[85] Yang Yue, Lin Zhang, Jeng-Yuan Yang, Raymond G Beausoleil, and Alan E Willner. Silicon-on-insulator polarization splitter using two horizontally slotted waveguides. *Optics letters*, 35(9):1364–1366, 2010.

[86] Jung Moo Hong, Hyun Ho Ryu, Soon Ryong Park, Jae Wan Jeong, Seung Gol Lee, El-Hang Lee, Se-Geun Park, Deokha Woo, Sunho Kim, and O Beom-Hoan. Design and fabrication of a significantly shortened multimode interference coupler for polarization splitter application. *IEEE Photonics Technology Letters*, 15(1):72–74, 2003.

[87] Yuqing Jiao, Daoxin Dai, Yaocheng Shi, and Sailing He. Shortened polarization beam

splitters with two cascaded multimode interference sections. *IEEE Photonics Technology Letters*, 21(20):1538–1540, 2009.

[88] Z Tu, YW Huang, HX Yi, XJ Wang, YP Li, L Li, and WW Hu. A compact soi polarization beam splitter based on multimode interference coupler. In *Asia Communications and Photonics Conference and Exhibition*, page 830707. Optical Society of America, 2011.

[89] Yawen Huang, Zhao Tu, Huaxiang Yi, Yanping Li, Xingjun Wang, and Weiwei Hu. High extinction ratio polarization beam splitter with multimode interference coupler on soi. *Optics Communications*, 307:46–49, 2013.

[90] Xiaowei Guan, Hao Wu, Yaocheng Shi, and Daoxin Dai. Extremely small polarization beam splitter based on a multimode interference coupler with a silicon hybrid plasmonic waveguide. *Optics Letters*, 39(2):259–262, 2014.

[91] Dong Wook Kim, Moon Hyeok Lee, Yudeuk Kim, and Kyong Hon Kim. Planar-type polarization beam splitter based on a bridged silicon waveguide coupler. *Optics express*, 23(2):998–1004, 2015.

[92] Isa Kiyat, Atilla Aydinli, and Nadir Dagli. A compact silicon-on-insulator polarization splitter. *IEEE photonics technology letters*, 17(1):100–102, 2004.

[93] Jinbiao Xiao, Xu Liu, and Xiaohan Sun. Design of a compact polarization splitter in horizontal multiple-slotted waveguide structures. *Japanese Journal of Applied Physics*, 47(5R):3748, 2008.

[94] Tomohide Yamazaki, Hideaki Aono, Junji Yamauchi, and Hisamatsu Nakano. Coupled waveguide polarization splitter with slightly different core widths. *Journal of lightwave technology*, 26(21):3528–3533, 2008.

[95] Jing Zhang, Mingbin Yu, Guo-Qiang Lo, and Dim-Lee Kwong. Silicon-waveguide-based mode evolution polarization rotator. *IEEE Journal of selected topics in quantum electronics*, 16(1):53–60, 2009.

[96] Ning-Ning Feng, Rong Sun, Jurgen Michel, and Lionel C Kimerling. Low-loss compact-size slotted waveguide polarization rotator and transformer. *Optics letters*, 32(15):2131–2133, 2007.

[97] BMA Rahman, SSA Obayya, N Somasiri, M Rajarajan, KTV Grattan, and HA El-Mikathi. Design and characterization of compact single-section passive polarization rotator. *Journal of lightwave technology*, 19(4):512, 2001.

[98] Henghua Deng, David O Yevick, Chris Brooks, and Paul E Jessop. Design rules for slanted-angle polarization rotators. *Journal of lightwave technology*, 23(1):432, 2005.

[99] Kang Tan, Ying Huang, Guo-Qiang Lo, Changyuan Yu, and Chengkuo Lee. Experimental realization of an o-band compact polarization splitter and rotator. *Optics express*, 25(4):3234–3241, 2017.

[100] Hang Guan, Ari Novack, Matthew Streshinsky, Ruizhi Shi, Qing Fang, Andy Eu-Jin Lim, Guo-Qiang Lo, Tom Baehr-Jones, and Michael Hochberg. Cmos-compatible highly efficient polarization splitter and rotator based on a double-etched directional coupler. *Optics express*, 22(3):2489–2496, 2014.

[101] Yunhong Ding, Liu Liu, Christophe Peucheret, and Haiyan Ou. Fabrication tolerant polarization splitter and rotator based on a tapered directional coupler. *Optics express*, 20(18):20021–20027, 2012.

[102] Daoxin Dai and John E Bowers. Novel concept for ultracompact polarization splitter-rotator based on silicon nanowires. *Optics express*, 19(11):10940–10949, 2011.

[103] Yule Xiong, Dan-Xia Xu, Jens H Schmid, Pavel Cheben, and N Ye Winnie. High extinction ratio and broadband silicon te-pass polarizer using subwavelength grating index engineering. *IEEE Photonics Journal*, 7(5):1–7, 2015.

[104] Mahmoud M Shahin, Hayk Gevorgyan, Marcus S Dahlem, and Anatol Khilo. Tm polarizer using segmented silicon waveguide. In *Integrated Photonics Research, Silicon and Nanophotonics*, pages IM2A–4. Optical Society of America, 2015.

[105] Zhan Su, Erman Timurdogan, Ehsan Shah Hosseini, Jie Sun, Gerald Leake, Douglas D Coolbaugh, and Michael R Watts. Four-port integrated polarizing beam splitter. *Optics letters*, 39(4):965–968, 2014.

[106] Y Suzuki, Hidetoshi Iwamura, Takeo Miyazawa, and Osamu Mikami. A novel waveguided polarization mode splitter using refractive index changes induced by superlattice disordering. *IEEE journal of quantum electronics*, 30(8):1794–1800, 1994.

[107] Osamu Watanabe, Masaaki Tsuchimori, Akane Okada, and Hiroshi Ito. Mode selective polymer channel waveguide defined by the photoinduced change in birefringence. *Applied physics letters*, 71(6):750–752, 1997.

[108] Min-Cheol Oh, Myung-Hyun Lee, and Hyung-Jong Lee. Polymeric waveguide polarization splitter with a buried birefringent polymer. *IEEE Photonics Technology Letters*, 11(9):1144–1146, 1999.

[109] Stephen R Forrest, Franky F So, and De Y Zang. Polarization-selective integrated optoelectronic devices incorporating crystalline organic thin films, December 15 1992. US Patent 5,172,385.

[110] Brent Everett Little. Integrated optics polarization beam splitter using form birefringence, April 25 2006. US Patent 7,035,491.

[111] X Sun, MZ Alam, J Stewart Aitchison, and M Mojahedi. Polarization rotator based on augmented low-index-guiding waveguide on silicon nitride/silicon-on-insulator platform. *Optics letters*, 41(14):3229–3232, 2016.

[112] Jeff Chiles, Tracy Sjaardema, Ashutosh Rao, and Sasan Fathpour. Damascene-patterned optical anisotropy in integrated photonics. *Optics Express*, 25(26):33664–33675, 2017.

[113] David E Aspnes. Optical properties of thin films. *Thin solid films*, 89(3):249–262, 1982.

[114] Tracy Sjaardema, Jeff Chiles, Ashutosh Rao, and Sasan Fathpour. Integrated polarization-selective microring resonators and beam taps via topographically anisotropic photonics. In *2017 IEEE Photonics Conference (IPC)*, pages 219–220. IEEE, 2017.

[115] Igor Moskalev, Sergey Mirov, Mike Mirov, Sergey Vasilyev, Viktor Smolski, Andrey Zakrevskiy, and Valentin Gapontsev. 140 w cr: Znse laser system. *Optics express*, 24(18):21090–21104, 2016.

[116] Timothy S McComb, R Andrew Sims, Christina CC Willis, Pankaj Kadwani, Vikas Sudesh, Lawrence Shah, and Martin Richardson. High-power widely tunable thulium fiber lasers. *Applied optics*, 49(32):6236–6242, 2010.

[117] Adam Lancaster, Gary Cook, Sean A McDaniel, Jonathan W Evans, Patrick A Berry, Jonathan Shephard, and Ajoy K Kar. Fe: Znse channel waveguide laser operating at 4122 nm. In *2015 Conference on Lasers and Electro-Optics (CLEO)*, pages 1–2. IEEE, 2015.

[118] John R Macdonald, Stephen J Beecher, Adam Lancaster, Patrick A Berry, Kenneth L Schepler, and Ajoy K Kar. Ultrabroad mid-infrared tunable cr: Znse channel waveguide laser. *IEEE Journal of Selected Topics in Quantum Electronics*, 21(1):375–379, 2014.

[119] Y Bai, N Bandyopadhyay, Slivken Tsao, S Slivken, and Manijeh Razeghi. Room tem-

perature quantum cascade lasers with 27% wall plug efficiency. *Applied Physics Letters*, 98(18):181102, 2011.

[120] Jeff Chiles and Sasan Fathpour. Silicon photonics beyond silicon-on-insulator. *Journal of Optics*, 19(5):053001, 2017.

[121] A. Honardoost, G. F. C. Gonzalez, S. Khan, M. Malinowski, A. Rao, J. Tremblay, A. Yadav, K. Richardson, M. C. Wu, and S. Fathpour. Cascaded integration of optical waveguides with third-order nonlinearity with lithium niobate waveguides on silicon substrates. *IEEE Photonics Journal*, 10(3):1–9, 2018.

[122] AS Mayer, A Klenner, AR Johnson, K Luke, MRE Lamont, Y Okawachi, M Lipson, AL Gaeta, and U Keller. Frequency comb offset detection using supercontinuum generation in silicon nitride waveguides. *Optics express*, 23(12):15440–15451, 2015.

[123] Alexander Klenner, Aline S Mayer, Adrea R Johnson, Kevin Luke, Michael RE Lamont, Yoshitomo Okawachi, Michal Lipson, Alexander L Gaeta, and Ursula Keller. Gigahertz frequency comb offset stabilization based on supercontinuum generation in silicon nitride waveguides. *Optics express*, 24(10):11043–11053, 2016.

[124] Guillermo Fernando Camacho Gonzalez, Marcin Malinowski, Amirmahdi Honardoost, and Sasan Fathpour. Design of a hybrid chalcogenide-glass on lithium-niobate waveguide structure for high-performance cascaded third-and second-order optical nonlinearities. *Applied optics*, 58(13):D1–D6, 2019.

[125] Guillermo Fernando Camacho-Gonzalez, Marcin Malinowski, Amirmahdi Honardoost, and Sasan Fathpour. Above-octave supercontinuum generation in a hybrid nonlinear waveguide for on-chip cascaded third- and second-order nonlinear-optic applications. In *Conference on Lasers and Electro-Optics*, page JTu2A.88. Optical Society of America, 2019.

[126] Xia Chen and Hon K Tsang. Polarization-independent grating couplers for silicon-on-insulator nanophotonic waveguides. *Optics letters*, 36(6):796–798, 2011.

[127] Michael R Watts, Minghao Qi, Tymon Barwicz, Luciano Socci, Peter T Rakich, Erich P Ippen, Henry I Smith, and AH Hermann. Towards integrated polarization diversity: design, fabrication, and characterization of integrated polarization splitters and rotators. In *OFC/NFOEC Technical Digest. Optical Fiber Communication Conference, 2005.*, volume 6, pages 3–pp. IEEE, 2005.